On variable-density subgrid effects in turbulent flows

A DISSERTATION
SUBMITTED TO THE FACULTY OF THE GRADUATE SCHOOL
OF THE UNIVERSITY OF MINNESOTA
BY

Sidharth GS

IN PARTIAL FULFILLMENT OF THE REQUIREMENTS
FOR THE DEGREE OF
DOCTOR OF PHILOSOPHY

Graham V. Candler

Nov, 2018

Acknowledgements

I thank my advisor, teachers, staff, cohorts, department, University, friends and family for their resources, help and support. Financial support from DOE/NNSA and AFOSR towards the research assistantship is acknowledged.

To good maths, good music, Ganga and the Mississippi.

Abstract

Eulerian mass density variations in a flow relate to compressibility and material inhomogeneities in the fluid. These variations can be caused due to high flow speeds, heat transfer, thermo-chemical reactions and/or phase change. From a local perspective, density gradient in space affects the velocity gradient dynamics due to variable inertia, in the presence of pressure-gradient driven acceleration, and therefore indirectly, the dissipation rate of kinetic energy and enstrophy. In turbulent flows, density variations and their effects on the velocity field influences the interscale interactions. Of particular interest is the turbulent dynamics in the presence of large vorticity generation by baroclinic torque. Although these effects are usually transient (in space or time) as turbulent mixing homogenizes the density field, the deviation from constant-density dynamical evolution can be statistically significant, particularly in instability-dominated flows with high sensitivity to initial/boundary conditions. In unsteady reacting flows, sustained chemi-acoustic interactions result in turbulent vorticity dynamics that is markedly different from the well-studied incompressible constant-density turbulence.

Large-eddy simulations of high Reynolds number variable-density flows require adequate representation of unresolved small-scale variable-density effects. The present work is an effort to understand subgrid-scale (SGS) variable-density effects to improve the fidelity and accuracy of our simulations in these regimes. The thesis focuses on Reynolds-filtered governing equations to compute the large-scale vorticity dynamics more precisely. A novel equation set for coarse-grained mass, momentum and energy is derived that employs only second order moment based closures, and allows explicit representation of subgrid-scale compressibility and inertial effects. The new form of the filtered equations has terms that represent the SGS mass flux, pressure-gradient acceleration, and velocity-dilatation correlation. We attempt to quantify the dynamical significance of these terms with direct numerical and large eddy simulations.

Contents

List of Tables

List of Figures

Chapter 1

Introduction

1.1 Background

Variable-density flows are ubiquitous in technology and nature. For example, significant variations in fluid density are encountered in high-speed flight, combustion, multi-phase flows and inertial confinement fusion. In nature, atmospheric and oceanic convection as well as astrophysical phenomena involve variable-density fluid dynamics.

Density variations in fluids can have different physical origins such as compressibility, thermal, compositional and phase inhomogeneity, chemical reactions and external energy sources and sinks. Primarily, there are two ways in which variations in the local density field interact with the local velocity field [66]: inertial effects, in which spatial variations in density correspond to spatial variations in the local pressure-gradient driven acceleration field, and dilatational effects, in which the Lagrangian variation in density corresponds to compression or expansion of the local Eulerian fluid element. These local interactions can significantly alter global flow dynamics. An important example of inertial effects is the case of variable density jets, where the jet to free-stream density ratio affects the global stability characteristics [107, 81], in free and transverse jets [43]. Another example of an inertial effect is the case of interfacial instabilities associated with accelerated variable-density interfaces, such as Rayleigh-Taylor [56] and Richtmyer-Meshkov instabilities [11]. The primary mechanism underlying these instabilities is baroclinic torque. The torque is produced by misalignment of independent thermodynamic quantities like pressure and density or equivalently, temperature and

entropy, and is represented in the general form of the vorticity equation.

$$\frac{\partial \vec{\omega}}{\partial t} + \nabla \times (\vec{\omega} \times \vec{v}) = \frac{1}{\rho^2} \nabla \rho \times \nabla p + \nabla \times \left(\frac{\nabla \cdot \sigma}{\rho} \right) + \nabla \times \vec{F}^b \tag{1.1}$$

where the σ_{ij} is the viscous stress tensor and $\vec{F}^b$ is non-conservative body force. In the framework of the Kovasznay decomposition of turbulent fluctuations [61], the interaction of acoustic and entropy modes produces vorticity modes via the baroclinic source term. This torque is also the primary vorticity source in shock-bubble [88] and shock-flame interactions [115]. Baroclinic instability and associated turbulence is also observed in the form of mid-latitude storms in the atmosphere [85] and mesoscale eddies in the ocean [44]. In the atmosphere, earth's rotation and differential heating produce vorticity, while in the oceans, horizontal density gradients are responsible. Secondary instabilities due to baroclinic torque are observed in two-dimensional Kelvin-Helmoltz billows of variable-density shear layers, as shown in the work of Fontane and Joly [35], Reinaud et al. [89]. Variable-density inertial effects are not only restricted to instabilities in quiescent flow states, but are also present in fully turbulent flows. For example, the density ratio of the streams in a mixing layer affects the entrainment ratio and composition of molecularly-mixed fluid in mixing layers [78, 37]. This is in addition to the reduction in growth rate and structural changes associated with increasing compressibility [12, 83, 121, 36, 34] and/or combustion-induced heat release. The composition of molecularly-mixed fluid has direct implications in the case of reactive mixing. In the reacting case, dilatational and baroclinic effects associated with heat release also contribute to the vorticity dynamics. Similarly, high-speed turbulent boundary layers exhibit significant variable-density effects due to near-wall thermal gradients [106]. This is reflected in the inertial transformations used to collapse the velocity profiles, such as the mean-density-based Van Driest transformation for adiabatic boundary layers [118] and mean-density-gradient-based transformations for non-adiabatic walls [84, 116].

1.2 Resolved-scale velocities in large eddy simulations

Simulations of technologically-relevant variable-density turbulent flows require truncation of the spatio-temporal scales of the computed physical fields due to computational

expense. Exclusion of information that represents a part of the physical system introduces the closure problem via the non-linearity of the governing equations. For accurate simulations, the closure problem has to be addressed, whether the simulations compute the time-averaged fields as in Reynolds averaged Navier-Stokes (RANS) or the spatially filtered fields, as in large eddy simulations (LES). This work focuses on the closure problem that results from non-representation of small-scale density fluctuations in large eddy simulations. The set of terms that require closure depends on the choice of the computed velocity field. For example, in the context of RANS, the choice of computed velocity variable can be either the time-averaged velocity or the density-weighted time-averaged velocity. The density-weighted averaging concept, also known as Favre averaging [32] is predominantly used. This method does not require closure of the mass conservation equation and retains the mathematical structure of the unclosed terms in a form that is structurally similar to their constant-density counterparts. Likewise, in LES, the resolved-scale velocity may be represented by the filtered velocity or Favre-filtered velocity. With the exception of the work of Yoshizawa [127], Boersma and Lele [7] and Sun and Lu [113], the Favre-filtered velocity is almost exclusively employed. The two velocity fields represent two different physical variables and their evolution is governed by different dynamics. An analogy may be drawn between the two resolved-scale velocities and the concept of mass velocity and momentum velocity introduced as bi-velocity hydrodynamics in [10].

[33] cites the importance of mass-averaged velocity for statistical analysis by stating that "the mean stream-surfaces lose their physical meaning as the mean stream-surfaces are crossed by the mean mass flux" in the case of Reynolds-averaged velocity. It is important to consider Favre's statement in the context of RANS and LES. While in RANS, steady-state stream surfaces would be desirable for the description of the flow-state, but this may not hold true for LES filter volumes. The resolved-scale velocity represents the local value of the filtered Eulerian velocity field, and may not necessarily represent the velocity of a frame of reference in which there is net zero SGS mass diffusion through the LES filter volume. Therefore, in this thesis, in addition to the Favre-filtered velocity formulation, we also consider unclosed terms arising in filtered-velocity based equations, which we refer to as the Reynolds-filtered formulation. We also note that

the resolved-scale thermodynamic variables may be represented identically, Reynolds-filtered or Favre-filtered, irrespective of the choice of resolved-scale velocity. This is important as the representation of resolved-scale thermodynamic quantities is required to be consistent with the laws of thermodynamics [33, 16]. From the point of resolved-scale vorticity statistics, the Reynolds-filtered velocity is the preferred variable. This is because the curl of the Favre-filtered velocity does not mathematically equal the Favre-filtered vorticity. This holds more generally for the resolved-scale velocity gradient tensor. Representation of resolved-scale vorticity by a compound variable involving the density field can have implications during subgrid-scale (SGS) modeling where information from small velocity scales, close to the filter width primarily guides the closure. In some previous work that use the Favre-filtered velocity formulation, the filtered velocity is algebraically estimated for closure even though it is not transported. This is discussed within an eddy viscosity framework in [40, 42], and within the stretched-vortex model in Sidharth et al. [103]. However, the equations based on Reynolds-filtered velocity are not commonly used because they require closure of additional SGS terms in the momentum equation. This includes an unsteady time-derivative term that can, in the case of strong density variations, be more significant than the SGS stress term [20]. In the present work, we will address this issue by deriving a new set of equations based on Reynolds-filtered velocity, and that has a closure set with SGS terms that depend on double correlations. Although the equations are developed for LES, they are applicable to RANS due to the formal equivalence.

1.3 Review of relevant literature

A review of the progress made in variable-density turbulence modeling is relevant as it helps identify unclosed terms that are important in these classes of flows. Since spatio-temporal variations in fluid density can have different physical origins, a variety of modeling techniques exist, spanning low-speed variable-density turbulent mixing to the high-speed turbulent flows and combustion. RANS modeling for variable-density turbulence has been a research field for several decades. Chassaing [18] and Chassaing et al. [19] provide a comprehensive review of variable-density modeling in RANS closure schemes. In first-order closures, variable-density effects in the $k - \epsilon$ framework have

been extensively studied. Important variable-density terms investigated are the turbulent mass flux [91], the pressure-dilatation [98], and the dilatational dissipation [129]. Also, terms associated with baroclinic torque and compression in the solenoidal dissipation rate equation have received interest [105, 62]. Some modeling techniques estimate the variance of density [114, 5] and pressure [130]. Within second-order closures, density fluctuation correlations have been analyzed in the work of Shih et al. [102], Chassaing et al. [17], Yoshizawa et al. [126] and Schwarzkopf et al. [100]. Pressure-strain [1] and pressure-acceleration-mass-flux terms [70] have been shown to be important for closure in second-order moment equations. It is important to note that in both first-order and second-order modeling, the Favre-averaged velocity is usually the solution variable. [102] investigate the evolution of non-density-averaged velocity in a variable-density mixing layer, but use constant-density approximation for the turbulent pressure-acceleration term appearing in the equation for mean velocity. In the class of algebraic second-order closures, an explicit algebraic stress model for compressible variable-density turbulent flows has been proposed [47], where the effect of density-velocity correlations on turbulence is accounted for. The authors in this work state their preference of Reynolds averaging over Favre averaging due to turbulent dissipation being a function of the fluctuating velocity field, and not the density-averaged fluctuating velocity. Similarly, in the class of stochastic methods for turbulent flow simulation, variable-density effects such as differential acceleration have been included in the work of [3].

A significant effort to understand variable-density and dilatational effects in turbulence has been carried out for turbulent premixed flames [94, 71, 92]. For example, [68] have pointed out that modeling of variable-density effects in turbulent flames is important and that there can be large differences between the Favre-averaged and the Reynolds-averaged scalars and velocities in the flame zone. Also, assumptions such as neglecting third-order covariances can lead to inconsistent results. They also find that the Favre-averaged turbulent kinetic energy production due to the pressure-acceleration-mass-flux term can override the suppression due to dilatation and cause counter-gradient turbulent diffusion of scalar concentration [9, 69, 6]. The authors state that their results "constitute a warning as to the dangers of carrying over the empiricism developed in constant-density flows to variable density flows in general and to turbulent reacting flows with significant heat release in particular." Counter-gradient diffusion of scalars

is more generally a variable-density effect in turbulence and has also been observed in inert helium-air mixing [65]. Variable-density effects in turbulent flames have also been discussed extensively in [22]. It must be noted however that the major focus of RANS analysis has been restricted to variable-density effects on the transport of second-order turbulent quantities. With regard to LES, there have been efforts to understand the role of filtered velocity and Favre-filtered velocity in turbulent flame dynamics. [15] show that the difference between the orientation of the vorticity vector obtained from the filtered velocity and Favre-filtered velocity in planar turbulent flames can be large. [101] account for the difference between the Favre-filtered scalar and the filtered scalar using the SGS specific volume flux, similar to the approach presented in [103]. The concept of counter-gradient diffusion due to variable-density effects is observed in LES as well, but with different physical connotations [60].

1.4 Scope of the current work

The thesis is organized as follows: Chapter 2 provides the governing equations for large eddy simulations of variable-density compressible flows. Both Reynolds-filtered and Favre-filtered formulations are discussed. The resolved-scale vorticity and conserved scalar equations are also considered. In the same chapter, the Karman-Howarth-Monin equation for variable-density compressible turbulent flows is derived for the second order velocity structure function under the assumption of local homogeneity. The equation presents an exact relation for dissipation rate of specific kinetic energy in the presence of density inhomogeneity and compressibility effects. Chapter 3 then discusses the primary numerical method employed for the computations reported in this thesis. The class of flows of interest involves variable-density turbulent mixing with and without heat release. Specific emphasis is placed on low numerical dissipation properties in the presence of under-resolved mixing interfaces, as is often the case in large-eddy simulations of these flows. Next, in Chapter 4, the effect of baroclinic vorticity in turbulent fine structures are studied within the framework of a stretched-spiral vortex. The results help qualitatively interpret the effect of variable-density mixing on the enstrophy spectrum of turbulent small scales. In Chapter 5, we carry out direct numerical simulations of two flows that involve compressible variable-density mixing. The first setup

is isotropic while the second setup is anisotropic and involves variable-density mixing transition of a heavy gas layer due to vorticity deposition by a planar shock. The fields from the direct simulations are explicitly filtered to inspect and analyze the importance of the subgrid-scale terms listed in Chapter 2. It is found that the variable-density SGS terms are as important as the SGS specific stress, which arises from spatial correlations of the velocity fields only. In Chapter 6, we carry out large-eddy simulations of flows with heat release using the Reynolds-filtered governing equations. The results serve to inform us of variable-density SGS effects in an *aposteriori* sense. The variable-density SGS terms are active, and play a role to improve stability computations while providing reasonable comparison with experimental measurements.

The present work aims to provide a self-consistent approach to modeling subgrid-scale variable-density effects in turbulent flows. An overarching theme of the work is to investigate the unweighted velocity fields, as opposed to mass weighted velocity fields. The two variables represent different physical observables, and follow different dynamics. One key difference is that the dimensional complexity of closure for the Favre-filtered momentum equation is higher. While the Reynolds-filtered momentum equation involves only second moment closure terms, the Favre-filtered equation requires closure of a third moment. Although there do not exist analytical closures, some resolved-scale variables do not have the information to even approximate certain SGS terms. For example, Favre-filtered velocity may be approximated using the filtered velocity and filtered density field. But the reverse is not true, as filtered specific volume is not a solution variable. Therefore, the choice of a resolved-scale velocity dictates how effectively its own dynamics can be modeled. Separately, computing Reynolds-filtered velocity implies computing Reynolds-filtered vorticity. Terms such as SGS baroclinic torque have exact origin in SGS terms appearing in the Reynolds-filtered velocity equation. The vorticity corresponding to Favre-filtered velocity is however a density convolved variable and does not have any contribution from SGS baroclinic torque in its dynamics. We expect filtered vorticity to be a genuine representation of the large-scale vorticity field, particularly in regions of large density variations. With these compelling reasons, we choose to focus on the Reynolds-filtered velocity dynamics, but not to present it as an alternative to Favre-filtered velocity dynamics but to improve our understanding of

how variable-density effects manifest themselves in the interscale dynamics of turbulent flows. Recent literature suggests that Reynolds-filtered variables in the presence of reactions do merit attention particularly to reduce modeling errors.

Chapter 2

Governing equations

In this chapter we discuss the governing equations for high Reynolds number compressible gas flows. The fields in a high Re flow can span multiple decades of length and time scales. Representation of the entire spectrum of scales is computationally prohibitive and therefore only the energy-containing large scales must be solved for. The equations are therefore filtered such that the small-scales are integrated away using a kernel. The dynamics of the filtered fields however, depends on the excluded small scales due to non-linearities in the Navier-Stokes equations. This dependence arises in the form of unclosed subfilter (or subgrid) terms. Representation of subgrid terms ensures, in a physically consistent sense, regularization of the non-linear terms in the equations, which is essential for discrete computation. Figure 2.1 shows how discrete sampling of a filtered field results in a smooth representation. Discrete undersampling of full-scale fields however, can lead to build up of large point-to-point fluctuations due to dealiasing.

We first focus on the filtered Navier-Stokes equations and two choices of resolved-scale velocities. Second, we identify the variable-density terms in Karman-Howarth-Monin equation for locally homogeneous turbulence to understand their effect on velocity correlations.

2.1 Filtered Navier-Stokes equations

Let us first review the formalism for filtering the Navier-Stokes equations and revisit the resulting governing equations. A spatio-temporal linear filter for a flow-realization

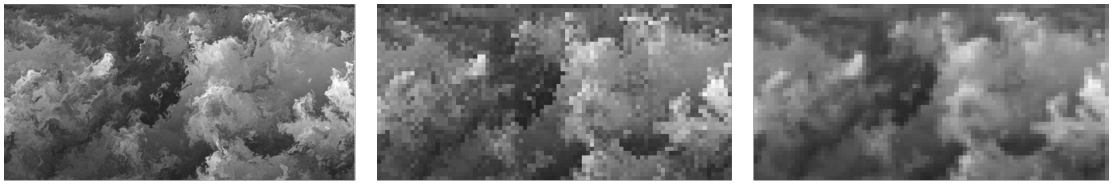

(a) DNS scalar field (b) Sampled at 8Δ (c) Filtered and sampled at 8Δ

Figure 2.1: An example illustrating the importance of filtering before undersampling for discrete representation of a smooth field. The image is from the reference [76]

with $\mathbf{x} = x_i$ may be defined as

$$\overline{f(\mathbf{x},t)} = \int G_{\Delta_x,\Delta_t}(\mathbf{x}-\mathbf{x}',t-t')f(\mathbf{x}',t)d^3\mathbf{x}'dt' \tag{2.1}$$

where G_{Δ_x,Δ_t} is the convolution kernel with an associated filter length scale Δ_x and a filter time scale Δ_t, satisfying

$$\int G_{\Delta_x,\Delta_t}(\mathbf{x}-\mathbf{x}')d^3\mathbf{x}'dt' = 1 \tag{2.2}$$

For large eddy simulation, filters are spatial and no temporal filtering is considered in this paper. It must be noted that the continuous filter is independent of the filter associated with the discrete solution field and the discrete differential operators used for numerical computation. We assume that the continuous filter is homogeneous and therefore commutes with the continuous differential operator. The governing equations for filtered mass, momentum, and energy are obtained from the filtered Navier-Stokes equations.

$$\frac{\partial}{\partial t}\begin{pmatrix} \bar{\rho} \\ \overline{\rho u_i} \\ \frac{1}{2}\overline{\rho u_k u_k} + \bar{E}_{\text{int}} \end{pmatrix} + \frac{\partial}{\partial x_j}\begin{pmatrix} \overline{\rho u_j} \\ \overline{\rho u_i u_j} + \bar{p}\delta_{ij} \\ \frac{1}{2}\overline{\rho u_k u_k u_j} + \overline{E_{\text{int}} u_j} + \overline{p u_j} \end{pmatrix} = \begin{pmatrix} 0 \\ \bar{\sigma}_{\rho u_i} \\ \bar{\sigma}_E \end{pmatrix} \tag{2.3}$$

E_{int} represents the internal energy per unit volume. The terms $\sigma_{\rho u_i}$ and σ_E correspond to diffusive molecular transport in the momentum and the energy equations, respectively. In the present analysis, the resolved-scale and the SGS terms that arise

from the expressions from $\bar{\sigma}_{\rho u_i}$ and $\bar{\sigma}_E$ are not expanded.

2.1.1 Favre-filtered velocity formulation

In the Favre-filtered velocity formulation, the filtered Navier-Stokes equations for variable-density flows are written in a form that uses the density-weighted filtered velocity as the resolved-scale velocity.

$$\frac{\partial}{\partial t}\begin{pmatrix} \bar{\rho} \\ \bar{\rho}\tilde{u}_i \\ \frac{1}{2}(\bar{\rho}\tilde{u}_k\tilde{u}_k + \tau^{\mathrm{F}}_{kk}) + \end{pmatrix} + \frac{\partial}{\partial x_j}\begin{pmatrix} \bar{\rho}\tilde{u}_j \\ \bar{\rho}\tilde{u}_i\tilde{u}_j + \bar{p}\delta_{ij} \\ \frac{1}{2}\bar{\rho}\tilde{u}_k\tilde{u}_k\tilde{u}_j + \bar{E}_{\mathrm{int}}\tilde{u}_j + \bar{p}\tilde{u}_j \end{pmatrix} + \frac{\partial}{\partial x_j}\begin{pmatrix} 0 \\ \tau^{\mathrm{F}}_{ij} \\ \frac{1}{2}\mathcal{K}^{\mathrm{F}}_j + \mathcal{H}^{\mathrm{F}}_j \end{pmatrix} = \begin{pmatrix} 0 \\ \bar{\sigma}_{\rho u_i} \\ \bar{\sigma}_E \end{pmatrix} \tag{2.4}$$

A Favre-filtered quantity is denoted by

$$\tilde{f} = \frac{\overline{\rho f}}{\bar{\rho}} \tag{2.5}$$

The resolved-scale velocity, $\tilde{u}_i$, is therefore obtained from the filtered momentum and the filtered density.

$$\tilde{u}_i = \frac{\overline{\rho u_i}}{\bar{\rho}} \tag{2.6}$$

The SGS terms in this formulation are the SGS stress tensor τ^{F}_{ij}, the SGS kinetic energy flux, $\mathcal{K}^{\mathrm{F}}_j$ and the SGS enthalpy flux $\mathcal{H}^{\mathrm{F}}_j$.

$$\tau^{\mathrm{F}}_{ij} = \overline{\rho u_i u_j} - \bar{\rho}\tilde{u}_i\tilde{u}_j,\ \mathcal{K}^{\mathrm{F}}_j = \overline{\rho u_k u_k u_j} - \bar{\rho}\tilde{u}_k\tilde{u}_k\tilde{u}_j,\ \mathcal{H}^{\mathrm{F}}_j = \overline{(E_{\mathrm{int}} + p)u_j} - (\bar{E}_{\mathrm{int}} + \bar{p})\tilde{u}_j \tag{2.7}$$

The filtered convective stress $\overline{\rho u_i u_j}$ is equivalent to the Favre-filtered specific stress $\bar{\rho}\widetilde{u_i u_j}$. The expression for the SGS stress $\tau^{\mathrm{F}}_{ij} = \bar{\rho}(\widetilde{u_i u_j} - \tilde{u}_i\tilde{u}_j)$ appears as a variable-density analog of the constant-density specific stress tensor $\overline{u_i u_j} - \bar{u}_i\bar{u}_j$.

The variable-density SGS contribution to the momentum equation can be written explicitly if we represent the SGS terms using central moments [39]. Let us denote the

central moments under the filter operator as

$$\mathcal{T}[a,b] = \overline{ab} - \bar{a}\bar{b} \tag{2.8}$$

$$\mathcal{T}[a,b,c] = \overline{abc} - \bar{a}\mathcal{T}[b,c] - \bar{b}\mathcal{T}[a,c] - \bar{c}\mathcal{T}[a,b] - \bar{a}\bar{b}\bar{c} \tag{2.9}$$

where a, b, c are field variables. The SGS stress tensor can then be expressed as

$$\tau_{ij}^{\mathrm{F}} = \bar{\rho}(\widetilde{u_i u_j} - \tilde{u}_i\tilde{u}_j) = \bar{\rho}\mathcal{T}[u_i,u_j] + \mathcal{T}[\rho,u_i,u_j] - \frac{1}{\bar{\rho}}\mathcal{T}[\rho,u_i]\,\mathcal{T}[\rho,u_j] \tag{2.10}$$

Equation 2.10 [42] shows that the SGS stress tensor in either formulation involves three unclosed terms: the SGS specific stress tensor $\mathcal{T}[u_i,u_j]$, the SGS mass flux $\mathcal{M}_i = \mathcal{T}[\rho,u_i]$, and the SGS trivariate moment $\mathcal{T}[\rho,u_i,u_j]$. Although absent in the mass conservation equation, the SGS mass flux $\mathcal{M}_i$ affects the Favre-filtered velocity SGS stress τ_{ij}^{F}.

Similarly, the SGS term $\mathcal{K}_j^{\mathrm{F}}$ appearing in the filtered total energy equation can be shown to consist of a fourth-order moment SGS term.

2.1.2 Reynolds-filtered velocity formulation

Now, let us represent the filtered Navier-Stokes equations using the filtered velocity. In this formulation, the equations are

$$\begin{aligned}\frac{\partial}{\partial t}\begin{pmatrix}\bar{\rho}\\ \bar{\rho}\bar{u}_i + \mathcal{M}_i\\ \bar{E}_{\mathrm{int}} + \frac{1}{2}\bar{\rho}\bar{u}_k\bar{u}_k + \frac{1}{2}\tau_{kk}^{\mathrm{R}}\end{pmatrix} + \frac{\partial}{\partial x_j}\begin{pmatrix}\bar{\rho}\bar{u}_j\\ \bar{\rho}\bar{u}_i\bar{u}_j + \bar{p}\delta_{ij}\\ \frac{1}{2}\bar{\rho}\bar{u}_k\bar{u}_k\bar{u}_j + \bar{E}_{\mathrm{int}}\bar{u}_j + \bar{p}\bar{u}_j\end{pmatrix}\\ + \frac{\partial}{\partial x_j}\begin{pmatrix}\mathcal{M}_j\\ \tau_{ij}^{\mathrm{R}}\\ \mathcal{K}_j^{\mathrm{R}} + \mathcal{H}_j^{\mathrm{R}}\end{pmatrix} = \begin{pmatrix}0\\ \bar{\sigma}_{\rho u_i}\\ \bar{\sigma}_E\end{pmatrix}\end{aligned} \tag{2.11}$$

The SGS terms with the superscript 'R' denote the same SGS terms as in the $\tilde{u}_i$ formulation, but with $\bar{u}_i$ as the resolved-scale velocity. Here,

$$\begin{aligned}
&\mathcal{M}_i = \overline{\rho u_i} - \bar{\rho}\bar{u}_i, \quad \tau_{ij}^{\mathrm{R}} = \overline{\rho u_i u_j} - \bar{\rho}\bar{u}_i\bar{u}_j \\
&\mathcal{K}_j^{\mathrm{R}} = \overline{\rho u_k u_k u_j} - \bar{\rho}\bar{u}_k\bar{u}_k\bar{u}_j, \quad \mathcal{H}_j^{\mathrm{R}} = \overline{(E_{\mathrm{int}} + p)u_j} - (\bar{E}_{\mathrm{int}} + \bar{p})\bar{u}_j
\end{aligned} \tag{2.12}$$

The additional SGS quantity $\mathcal{M}_i$ is the SGS mass flux and represents the spatial correlation of density with velocity under the filter operator. It is a measure of the difference between the quantity $\bar{\rho}\bar{u}_i$ and the filtered momentum. With the use of central moments, the SGS stress in this formulation can be written as

$$\tau_{ij}^{\mathrm{R}} = \overline{\rho u_i u_j} - \bar{\rho}\bar{u}_i\bar{u}_j = \bar{\rho}\mathcal{T}\left[u_i, u_j\right] + \mathcal{T}\left[\rho, u_i, u_j\right] + \bar{u}_i\mathcal{T}\left[\rho, u_j\right] + \bar{u}_j\mathcal{T}\left[\rho, u_i\right] \tag{2.13}$$

We observe that the term τ_{ij}^{R} like τ_{ij}^{F}, consists of the SGS specific stress, the SGS trivariate moment term, and the SGS mass flux term. However the resolved-scale momentum equation in this formulation also includes the rate of change of SGS mass flux.

In order to understand the unclosed time derivative, we examine the differences between $\bar{u}_i$ and $\tilde{u}_i$ by comparing their respective inviscid transport equations. The governing equation for the Favre-filtered velocity is obtained using the transport equations for the filtered momentum and filtered density. The equation for filtered velocity is obtained by filtering the transport equation for velocity. If we compare the two transport equations, it is seen that in the equation for $\bar{u}_i$, there exist SGS terms other than the SGS specific stress $\mathcal{T}\left[u_i, u_j\right] = \overline{u_i u_j} - \bar{u}_i\bar{u}_j$.

$$\frac{\partial\tilde{u}_i}{\partial t} + \tilde{u}_j\frac{\partial\tilde{u}_i}{\partial x_j} + \frac{1}{\bar{\rho}}\frac{\partial\bar{p}}{\partial x_i} + \frac{1}{\bar{\rho}}\frac{\partial\bar{\rho}(\widetilde{u_i u_j} - \tilde{u}_i\tilde{u}_j)}{\partial x_j} = 0 \tag{2.14}$$

$$\frac{\partial\bar{u}_i}{\partial t} + \bar{u}_j\frac{\partial\bar{u}_i}{\partial x_j} + \frac{1}{\bar{\rho}}\frac{\partial\bar{p}}{\partial x_i} + \frac{\partial(\overline{u_i u_j} - \bar{u}_i\bar{u}_j)}{\partial x_j} - \mathcal{T}\left[u_i, \frac{\partial u_j}{\partial x_j}\right] - \frac{1}{\bar{\rho}}\mathcal{T}\left[\rho, \frac{1}{\rho}\frac{\partial p}{\partial x_i}\right] = 0 \tag{2.15}$$

These additional SGS terms are associated with dilatation, $\nabla \cdot u$, and pressure acceleration, $\nabla p/\rho$. This is due to the non-conservative nature of velocity in the presence of variable-density effects.

The transport equations for $\tilde{u}_i$ (2.14) and $\bar{u}_i$ (2.15), with the filtered density equation,

can be used to derive the transport equation for the SGS mass flux $\mathcal{M}_i$.

$$\begin{aligned}\frac{\partial \mathcal{M}_i}{\partial t} =& \frac{\partial(\overline{\rho u_i} - \bar{\rho}\bar{u}_i)}{\partial t} \\ =& -\frac{\partial \overline{\rho u_i u_j}}{\partial x_j} + \bar{u}_i \frac{\partial \mathcal{M}_j}{\partial x_j} + \frac{\partial \bar{\rho}\bar{u}_i\bar{u}_j}{\partial x_j} + \bar{\rho}\frac{\partial \mathcal{T}\left[u_i, u_j\right]}{\partial x_j} - \bar{\rho}\mathcal{T}\left[u_i, \frac{\partial u_j}{\partial x_j}\right] - \mathcal{T}\left[\rho, \frac{1}{\rho}\frac{\partial p}{\partial x_i}\right]\end{aligned} \tag{2.16}$$

For the sake of clarity, we do not consider terms corresponding to viscous molecular transport and work with the inviscid transport equations; including viscous transport term is straight-forward and produces an additional term, $\mathcal{T}\left[\rho, \sigma_{\rho u_i}/\rho\right]$ in (2.16). We note that the filtered momentum equation is a composite equation transporting two physical variables, $\bar{u}_i$ and $\mathcal{M}_i$. This implies that a part of the SGS term $\partial_j \tau^{\mathrm{R}}_{ij}$ corresponds to the convection of $\mathcal{M}_i$. Therefore, the equation for $\bar{u}_i$ can be simplified by decoupling it from the equation for SGS mass flux. Substituting for $\partial_t \mathcal{M}_i$ from (2.16), we obtain

$$\frac{\partial \bar{\rho}\bar{u}_i}{\partial t} + \frac{\partial \mathcal{M}_i}{\partial t} + \frac{\partial \overline{\rho u_i u_j}}{\partial x_j} + \frac{\partial \bar{p}}{\partial x_i} = \frac{\partial \bar{\rho}\bar{u}_i}{\partial t} + \frac{\partial \bar{\rho}\bar{u}_i\bar{u}_j}{\partial x_j} + \frac{\partial \bar{p}}{\partial x_i} + \mathcal{S}_{\rho u_i} \tag{2.17}$$

$$\text{where} \quad \mathcal{S}_{\rho u_i} = \bar{u}_i \mathcal{S}_\rho + \bar{\rho}\frac{\partial \mathcal{T}\left[u_i, u_j\right]}{\partial x_j} - \bar{\rho}\mathcal{T}\left[u_i, \frac{\partial u_j}{\partial x_j}\right] - \mathcal{T}\left[\rho, \frac{1}{\rho}\frac{\partial p}{\partial x_i}\right] \tag{2.18}$$

$$\text{and} \quad \mathcal{S}_\rho = \frac{\partial \mathcal{M}_j}{\partial x_j} = \frac{\partial(\overline{\rho u_j} - \bar{\rho}\ \bar{u}_j)}{\partial x_j} \tag{2.19}$$

$$\mathcal{S}_E = \frac{\partial}{\partial x_j}\left(\mathcal{T}\left[E_{\mathrm{int}}, u_j\right]\right) + \mathcal{T}\left[p, \frac{\partial u_j}{\partial x_j}\right] + \bar{u}_k \mathcal{S}_{\rho u_k} - \frac{1}{2}\bar{u}_k\bar{u}_k\mathcal{S}_\rho \tag{2.20}$$

Similarly, the filtered energy equation is also a composite equation, where the variable $\frac{1}{2}\tau^{\mathrm{R}}_{kk}$ is convected along with $\bar{E}_{\mathrm{int}}$ and $\frac{1}{2}\bar{\rho}\bar{u}_k\bar{u}_k$. A part of the SGS term $\partial_j(\mathcal{K}^{\mathrm{R}}_j + \mathcal{H}^{\mathrm{R}}_j)$ in the filtered energy equation therefore corresponds to the convective transport of SGS kinetic energy $\frac{1}{2}\tau^{\mathrm{R}}_{kk}$. Similar to the filtered momentum equation, the filtered energy equation can be reduced as well. The transport equations for filtered the kinetic energy, filtered momentum, and filtered velocity are used to obtain the transport equation for

$\frac{1}{2}\tau_{kk}^{\mathrm{R}} = \frac{1}{2}(\overline{\rho u_k u_k} - \bar{\rho}\bar{u}_k\bar{u}_k)$.

$$\begin{aligned}\frac{1}{2}\frac{\partial}{\partial t}\left(\overline{\rho u_k u_k} - \bar{\rho}\bar{u}_k\bar{u}_k\right) =& \frac{1}{2}\frac{\partial \overline{\rho u_k u_k}}{\partial t} - \frac{1}{2}\bar{u}_k\frac{\partial \bar{\rho}\bar{u}_k}{\partial t} - \frac{1}{2}\bar{\rho}\bar{u}_k\frac{\partial \bar{u}_k}{\partial t} \\ =& -\frac{\partial}{\partial x_j}\left(\frac{1}{2}\overline{\rho u_k u_k u_j} + \overline{p u_j}\right) + \mathcal{T}\left[p, \frac{\partial u_j}{\partial x_j}\right] + \frac{\partial \bar{p}\bar{u}_j}{\partial x_j} \\ &+ \frac{1}{2}\frac{\partial \bar{\rho}\bar{u}_k\bar{u}_k\bar{u}_j}{\partial x_j} + \bar{u}_k\mathcal{S}_{\rho u_k} - \frac{1}{2}\bar{u}_k\bar{u}_k\mathcal{S}_\rho\end{aligned} \tag{2.21}$$

Substituting $\partial_t \frac{1}{2}\tau_{kk}^{\mathrm{R}}$ in the filtered total energy equation, we obtain

$$\begin{aligned}&\frac{\partial}{\partial t}\left(\bar{E}_{\mathrm{int}} + \frac{1}{2}\bar{\rho}\bar{u}_k\bar{u}_k + \frac{1}{2}\tau_{kk}^{\mathrm{F}}\right) + \frac{\partial}{\partial x_j}\left(\overline{E_{\mathrm{int}}u_j} + \overline{\rho u_k u_k u_j} + \overline{p u_j}\right) \\ =&\frac{\partial}{\partial t}\left(\bar{E}_{\mathrm{int}} + \frac{1}{2}\bar{\rho}\bar{u}_k\bar{u}_k\right) + \frac{\partial}{\partial x_j}\left(\bar{E}_{\mathrm{int}}\bar{u}_j + \frac{1}{2}\bar{\rho}\bar{u}_k\bar{u}_k\bar{u}_j + \bar{p}\bar{u}_j\right) + \mathcal{S}_E\end{aligned} \tag{2.22}$$

where the SGS terms in the transport of the quantity $\bar{E}_{\mathrm{int}} + \frac{1}{2}\bar{u}_k\bar{u}_k$ are

$$\mathcal{S}_E = \frac{\partial}{\partial x_j}\left(\mathcal{T}\left[E_{\mathrm{int}}, u_j\right]\right) + \mathcal{T}\left[p, \frac{\partial u_j}{\partial x_j}\right] + \bar{u}_k\mathcal{S}_{\rho u_k} - \frac{1}{2}\bar{u}_k\bar{u}_k\mathcal{S}_\rho \tag{2.23}$$

Thus, the Reynolds-filtered LES equations can then be written as:

$$\frac{\partial}{\partial t}\begin{pmatrix}\bar{\rho}\\ \bar{\rho}\bar{u}_i\\ \bar{E}_{\mathrm{int}} + \frac{1}{2}\bar{\rho}\bar{u}_k\bar{u}_k\end{pmatrix} + \frac{\partial}{\partial x_j}\begin{pmatrix}\bar{\rho}\bar{u}_j\\ \bar{\rho}\bar{u}_i\bar{u}_j + \bar{p}\delta_{ij}\\ \frac{1}{2}\bar{\rho}\bar{u}_k\bar{u}_k\bar{u}_j + \bar{E}_{\mathrm{int}}\bar{u}_j + \bar{p}\bar{u}_j\end{pmatrix} + \begin{pmatrix}\mathcal{S}_\rho\\ \mathcal{S}_{\rho u_i}\\ \mathcal{S}_E\end{pmatrix} = \begin{pmatrix}0\\ \bar{\sigma}_{\rho u_i}\\ \bar{\sigma}_E\end{pmatrix} \tag{2.24}$$

where the SGS contribution to the governing equations is:

$$\mathcal{S}_\rho = \frac{\partial \mathcal{T}\left[\rho, u_j\right]}{\partial x_j} \tag{2.25}$$

$$\mathcal{S}_{\rho u_i} = \bar{u}_i\mathcal{S}_\rho + \bar{\rho}\frac{\partial \mathcal{T}\left[u_i, u_j\right]}{\partial x_j} - \mathcal{T}\left[\rho, \frac{1}{\rho}\frac{\partial p}{\partial x_i}\right] - \bar{\rho}\,\mathcal{T}\left[\nabla\cdot u, u_i\right] \tag{2.26}$$

$$\mathcal{S}_E = \bar{u}_i\mathcal{S}_{\rho u_i} - \frac{1}{2}\bar{u}_i\bar{u}_i\mathcal{S}_\rho + \frac{\partial \mathcal{T}\left[E_{\mathrm{int}}, u_j\right]}{\partial x_j} + \mathcal{T}\left[\nabla\cdot u, p\right] \tag{2.27}$$

The conservation-law form of the closed convective terms is maintained and the non-conservative SGS source terms arise as a consequence of choosing to solve for the filtered

velocity instead of the filtered momentum. The unclosed SGS terms are:

- SGS mass flux $\mathcal{T}\left[\rho, u_i\right] = \overline{\rho u_i} - \bar{\rho}\bar{u}_i$
- SGS specific stress $\mathcal{T}\left[u_i, u_j\right] = \overline{u_i u_j} - \bar{u}_i\bar{u}_j$
- SGS dilatational flux $\mathcal{T}\left[\nabla \cdot u, u_i\right] = \overline{(\nabla \cdot u)u_i} - (\nabla \cdot \bar{u})\bar{u}_i$
- SGS pressure work $\mathcal{T}\left[\nabla \cdot u, p\right] = \overline{(\nabla \cdot u)p} - (\nabla \cdot \bar{u})\bar{p}$
- SGS pressure acceleration $\mathcal{T}\left[\rho, \nabla_i p/\rho\right]/\bar{\rho} = -(\overline{\nabla_i p/\rho} - \nabla_i \bar{p}/\bar{\rho})$
- SGS internal energy flux $\mathcal{T}\left[E_{\text{int}}, u_i\right] = \overline{E_{\text{int}} u_i} - \bar{E}_{\text{int}}\bar{u}_i$

All of the SGS terms satisfy the principle of Galilean invariance. The new SGS terms corresponding to variable-density effects not previously analyzed in the LES literature are the SGS pressure acceleration and the SGS dilatational flux. The SGS pressure acceleration arises due to the non-linear interaction between pressure gradient and density. The SGS dilatational flux arises from the non-linear product of dilatation and velocity. We observe its similarity to the SGS pressure work, commonly referred to as the SGS pressure-dilatation. SGS pressure work has been studied extensively in the literature, because it appears in the transport equation of SGS kinetic energy, irrespective of the choice of the resolved-scale velocity variable. It should also be noted that in a multi-component reacting flow, $\bar{p}$ cannot be obtained directly from $\bar{E}_{\text{int}}$. In flows that involve non-constant $\partial p/\partial E_{\text{int}}|_\rho$, such as in the case of real/dense gas effects or multi-component mixture of gases with different heat capacity ratio, the term $\bar{p} - p(\bar{E}_{\text{int}}, \bar{\rho})$ requires closure as well. In such a case, non-linear relation between pressure and total internal energy effects the momentum equation through the filtered pressure. In this paper, we consider a single gas that obeys the ideal gas law. Therefore, the SGS term $\bar{p} - p(\bar{E}_{\text{int}}, \bar{\rho})$ does not appear in the resolved-scale momentum equation.

The primary advantage of the new equations over the conventional Reynolds-filtered formulation is the presence of a framework in which SGS contributions arising from spatial and Lagrangian density variations may be explicitly quantified. The simplified

nature of the SGS terms avoids the trivariate central moment $\mathcal{T}\left[\rho, u_i, u_j\right]$ in the filtered momentum equation and the quadrivariate central moment $\mathcal{T}\left[\rho, u_k, u_k, u_j\right]$ in the energy equation. This is a result of decoupling the transport equation for the SGS mass flux $\mathcal{M}_i$ and the SGS kinetic energy $\frac{1}{2}\tau_{kk}^{\mathrm{R}}$ from the filtered momentum and the filtered energy equations. The decoupling concept for the energy equation is not restricted to a Reynolds-filtered formulation. For Favre-filtered equations, solving for the variable $\bar{E}_{\mathrm{int}} + \frac{1}{2}\bar{\rho}\tilde{u}_k\tilde{u}_k$ (referred to as computable energy in Vreman 1995), instead of the filtered total energy $\bar{E}_{\mathrm{int}} + \frac{1}{2}\bar{\rho}\widetilde{u_k u_k}$ removes $\mathcal{K}_j^{\mathrm{F}}$. Following a procedure similar to (2.21), we may obtain the following Favre-filtered kinetic energy equation in which no quadrivariate central moments appear.

$$\frac{\partial}{\partial t}\left(\frac{\bar{\rho}\tilde{u}_k\tilde{u}_k}{2} + \bar{E}_{\mathrm{int}}\right) + \frac{\partial}{\partial x_j}\left(\overline{E_{\mathrm{int}}u_j} + \frac{\bar{\rho}\tilde{u}_k\tilde{u}_k\tilde{u}_j}{2} + \bar{p}\tilde{u}_j\right) + \tilde{u}_i\frac{\partial \tau_{ij}^{\mathrm{F}}}{\partial x_j} + \left(\overline{p\frac{\partial u_j}{\partial x_j}} - \bar{p}\frac{\partial \tilde{u}_j}{\partial x_j}\right) = \bar{\sigma}_E \tag{2.28}$$

2.1.3 Filtered vorticity equation

The resolved-scale vorticity computed from the equations is a consequence of the choice of the resolved-scale velocity. While the Reynolds-filtered formulation computes filtered vorticity $\bar{\omega}_i$, in the case of Favre-filtered velocity, the resolved-scale vorticity variable is $\omega_i^{\mathrm{F}} = \nabla \times \overline{\rho u_i}/\bar{\rho}$. This is different from the filtered vorticity $\bar{\omega}_i$, or even the Favre-filtered vorticity $\tilde{\omega}_i$. Consider the filtered inviscid vorticity equation with the SGS terms represented as central moments.

$$\frac{\partial \bar{\omega}_i}{\partial t} + \frac{\partial \bar{\omega}_i\bar{u}_j}{\partial x_j} + \frac{\partial \mathcal{T}\left[\omega_i, u_j\right]}{\partial x_j} = \bar{\omega}_j\frac{\partial \bar{u}_i}{\partial x_j} + \mathcal{T}\left[\omega_j, \frac{\partial u_i}{\partial x_j}\right] - \epsilon_{ijk}\left(\frac{\partial(\overline{1/\rho})}{\partial x_j}\frac{\partial \bar{p}}{\partial x_k} + \mathcal{T}\left[\frac{\partial(1/\rho)}{\partial x_j}, \frac{\partial p}{\partial x_k}\right]\right) \tag{2.29}$$

The SGS contributions to vorticity flux, vortex stretching, and baroclinic torque can be seen to appear separately. We observe that the curl of the SGS pressure acceleration is the SGS baroclinic torque.

$$-\epsilon_{ijk}\mathcal{T}\left[\frac{\partial}{\partial x_j}\left(\frac{1}{\rho}\right),\frac{\partial p}{\partial x_k}\right]=\epsilon_{ijk}\frac{\partial}{\partial x_j}\left(\frac{1}{\bar{\rho}}\mathcal{T}\left[\rho,\frac{1}{\rho}\frac{\partial p}{\partial x_k}\right]\right) \tag{2.30}$$

The SGS acceleration field contributes to the filtered vorticity, and more generally to the entire filtered velocity gradient tensor. The symmetric part of the SGS pressure acceleration gradient tensor $\partial_j(\mathcal{T}\left[\rho,\partial_k p/\rho\right]/\bar{\rho})$ appears as a source term in the filtered strain rate $\bar{S}_{ij}$ equation. SGS pressure acceleration, due its dependence on both pressure and density field, can distinguish between entropic and acoustic density fluctuations. This can be important for modeling [50, 93].

Therefore, we see that the curl of the Reynolds-filtered and Favre-filtered velocities represent physically different resolved-scale vorticity variables. In particular, the subgrid-scale baroclinic torque affects Reynolds-filtered vorticity $\bar{\omega}_i$, but does not explicitly affect ω_i^{F}.

2.1.4 Filtered scalar advection equation

It is important to discuss scalar advection equation in the context of variable-density flows. For example, flows that involve multicomponent mixing and combustion require advection of species densities. When a combustion model is used, a reaction progress variable is advected. The filtered inviscid scalar advection equations with $\tilde{u}_i$ and $\bar{u}_i$ are

$$\frac{\partial\bar{\rho}\tilde{c}}{\partial t}+\frac{\partial\bar{\rho}\tilde{u}_j\tilde{c}}{\partial x_j}+\frac{\partial\mathcal{C}_j}{\partial x_j}=\overline{\rho\Omega}_c \tag{2.31}$$

$$\frac{\partial\bar{\rho}\tilde{c}}{\partial t}+\frac{\partial\bar{\rho}\bar{u}_j\tilde{c}}{\partial x_j}+\frac{\partial\mathcal{T}\left[\rho c,u_j\right]}{\partial x_j}=\overline{\rho\Omega}_c \tag{2.32}$$

where scalar c is the advected variable. Ω_c represents the source term in the transport equation of the scalar c. The unclosed term in the Favre-filtered velocity scalar equation can be expressed with central moments similar to the subgrid-scale stress τ_{ij}^{F}

$$\mathcal{C}_j=\overline{\rho u_j c}-\bar{\rho}\tilde{u}_j\tilde{c}=\bar{\rho}(\widetilde{cu}_j-\tilde{c}\tilde{u}_j) \tag{2.33}$$

$$=\bar{\rho}\mathcal{T}\left[c,u_j\right]+\mathcal{T}\left[\rho,u_j,c\right]-\frac{1}{\bar{\rho}}\mathcal{T}\left[\rho,u_j\right]\mathcal{T}\left[\rho,c\right] \tag{2.34}$$

In the equations above, the Favre-filtered scalar is transported. It is also possible to derive the transport equation for the filtered scalar and express the equation in a conservation law form:

$$\frac{\partial \bar{\rho}\bar{c}}{\partial t} + \frac{\partial \bar{\rho}\bar{u}_j\bar{c}}{\partial x_j} + \mathcal{S}_{\rho c} = \bar{\rho}\bar{\Omega}_c \tag{2.35}$$

where the subgrid-scale contribution $\mathcal{S}_{\rho c}$ is expressed in the form of central moments as

$$\mathcal{S}_{\rho c} = \bar{\rho}\frac{\partial \mathcal{T}\left[c, u_j\right]}{\partial x_j} + \bar{c}\ \mathcal{S}_\rho - \bar{\rho}\mathcal{T}\left[c, \frac{\partial u_j}{\partial x_j}\right] \tag{2.36}$$

Equation (2.35) is obtained by decoupling the inviscid transport equation for $\mathcal{T}\left[\rho, c\right]$ from (2.31), similar to the procedure we adopt for the resolved-scale momentum and the energy equations. We observe that usage of filtered velocity does not involve the trivariate moment $\mathcal{T}\left[\rho, u_j, c\right]$ in the unclosed terms. In the case of Favre-filtered scalar and the filtered velocity, the effect of density appears in subgrid-scale conserved scalar flux $\mathcal{T}\left[\rho c, u_j\right]$. If the filtered scalar is transported, the effect of SGS mass flux and SGS dilatation can be represented explicitly.

2.2 Variable-density Karman-Howarth-Monin equation

Subgrid-scale terms are related to structure functions by the following relation by Germano [41]

$$\tau_{ij}(x) = \frac{1}{2}\iint G(x-y)G\left(x-y'\right)d_{ij}\left(y,y'\right)dydy' \tag{2.37}$$

$$d_{ij}(x,x^{\wr}) = (u_i(x) - u_j(x^{\wr}))(u_j(x) - u_j(x^{\wr})) = (u_i - u_i^{\wr})(u_j - u_j^{\wr}) \tag{2.38}$$

Therefore, the structure functions encase subgrid scale information within them and understanding their evolutions in multi-scale turbulent flows with appropriate assumptions can improve our understanding of laws that govern motion at different scales. Separation of scales in turbulent flows is of importance to theory as well as numerical computations.

In incompressible turbulence, the Kolmogorov 4/5-law is an exact relation that describes a scale invariant net energy cascade for scales that lie in the inertial subrange. In the presence of inhomogeneity and anisotropy, the more general Karman-Howarth-Monin (K-H-M) equation describes the interscale tranfer of energy. The two point K-H-M equation contains terms that can be used to analyze the scale-by-scale energy transfer, specifically via the divergence of the non-linear transport term in $r = x - x'$ space. By understanding the role of different terms in the K-H-M equation in a variable-density compressible setting, we can identify different mechanisms of interscale energy transfer in addition to the conventional Richardson-Kolmogorov cascade.

We briefly review related work in the literature. Lai et al. [64] derived the generalized K-H-M equation for variable-density effects in the incompressible limit and employed it to analyze the negative turbulent kinetic energy production in a turbulent jet of heavy gas. The VD K-H-M predicted a decelerated energy cascade due to non-Boussinesq effects. In the case of compressible turbulence, two forms of exact relations have been derived as a compressible analog the conventional energy cascade. Galtier and Banerjee [38] derived an exact relation in compressible isothermal turbulence for two point correlations

$$\begin{aligned} -2\varepsilon_E = &\left\langle \left(\nabla' \cdot \mathbf{u}'\right)(R - E)\right\rangle + \left\langle (\nabla \cdot \mathbf{u})\left(\tilde{R} - E'\right)\right\rangle \\ &+\nabla_{\mathbf{r}} \cdot \left\langle \left[\frac{\delta(\rho\mathbf{u}) \cdot \delta\mathbf{u}}{2} + \delta\rho\delta e - C_s^2\overline{\delta}\rho\right]\delta\mathbf{u} + \overline{\delta}e\delta(\rho\mathbf{u})\right\rangle \end{aligned} \tag{2.39}$$

using the identity

$$\frac{\langle R\rangle + \langle\tilde{R}\rangle}{2} = \langle E\rangle - \frac{1}{4}\langle\delta(\rho\mathbf{u}) \cdot \delta\mathbf{u}\rangle - \frac{1}{2}\langle\delta\rho\delta e\rangle \tag{2.40}$$

where $E = \rho u^2/2 + \rho e$, $R = \rho\mathbf{u} \cdot \mathbf{u}'/2 + \rho e'$ and $\tilde{R} \equiv \rho'\mathbf{u}' \cdot \mathbf{u}/2 + \rho' e$, $\overline{\delta}X \equiv \left(X + X'\right)/2$ and ε_E is the mean total energy injection rate. Falkovich et al. [31] proposed an exact relation in the form a current-density correlation function.

$$\sum_j \langle\rho(0)v_j(0)\left[\rho(\boldsymbol{r})v_j(\boldsymbol{r})v_i(\boldsymbol{r}) + p(\boldsymbol{r})\delta_{ij}\right]\rangle = \frac{\epsilon r_i}{3} \tag{2.41}$$

Here, dissipation is defined as $\epsilon = \langle\rho(0)\boldsymbol{v}(0) \cdot \boldsymbol{f}(0)\rangle$. However, stationarity of the fourth

order correlation $\langle \rho(0,t)v_j(0,t)\rho(\boldsymbol{r},t)v_j(\boldsymbol{r},t)\rangle$ is assumed. Aluie [2] used a coarse grained approach to prove that the interscale transfer of kinetic energy in developed compressible turbulence was local. He proved the scale locality of baropycnal flux $\partial_j\bar{p}/\bar{\rho}\mathcal{T}[\rho,u_j]$ and assumed that pressure-dilatation term $\bar{p}\nabla\cdot\bar{u}$ is negligible at small scales. The theory behind scale locality [29] in developed turbulence has also been recently applied to understand turbulent dissipative anomalies [30] in compressible turbulence and the pressure-work defect due to shocks.

In this section, we focus on the second order structure function of velocity. We are not particularly interested to obtain a conventional cascade for fully developed compressible variable-density turbulence. Instead, we are interested in the new density-variation dependent terms that appear in the evolution equation for the structure function. The velocity-velocity correlation is the most important correlation in turbulent flows and the primary term constituting the Reynolds- and the Favre-filtered stress tensor. Therefore, we investigate the two point velocity difference instead of the momentum-velocity difference.

We derive the generalized compressible variable-density equations of the Karman-Howarth-Monin form which assume only local homogeneity but not local isotropy. We follow Monin's [80] procedure and derive the equations in a form presented in Hill [53]. The superscript $\wr$ on $u_i^\wr$ indicates the values of the field u_i at a position $x_i^\wr$ where the separation vector is defined as $\boldsymbol{r} = r_i = x^\wr - x$. Also, $\dot{u}_i$ indicates $\partial_t u_i$, ϑ denotes dilatation $\partial_k u_k$. We begin with the velocity equation

$$\dot{u}_i + u_k\partial_k u_i + \partial_i p/\rho = \nu\partial_k\partial_k u_i + \frac{\nu}{3}\partial_i\vartheta \tag{2.42}$$

Using $\langle u_j\dot{u}_i + u_i\dot{u}_j - u_i\dot{u}_j^\wr - u_j^\wr\dot{u}_i - u_i^\wr\dot{u}_j - u_j\dot{u}_i^\wr + u_j^\wr\dot{u}_i^\wr + u_i^\wr\dot{u}_j^\wr\rangle$, we obtain

$$
\begin{aligned}
&\dot{D}_{ij}(\boldsymbol{r}) + \langle \partial_k u_i u_j u_k - u_i u_j \vartheta - \partial_k (u_i u_j^{\prime} u_k) - \partial_k^{\prime}(u_i u_j^{\prime} u_k^{\prime}) + u_i u_j^{\prime}(\vartheta + \vartheta^{\prime})\rangle \\
&\quad + \langle \partial_k^{\prime} u_i^{\prime} u_j^{\prime} u_k^{\prime} - u_i^{\prime} u_j^{\prime} \vartheta^{\prime} - \partial_k (u_i^{\prime} u_j u_k) - \partial_k^{\prime}(u_i^{\prime} u_j u_k^{\prime}) + u_i^{\prime} u_j (\vartheta + \vartheta^{\prime})\rangle \\
&\quad = \langle T_{ij}(\boldsymbol{r})\rangle + \langle \nu \partial_k \partial_k u_i u_j \rangle - 2\langle \nu \partial_k u_i \partial_k u_j \rangle \\
&\quad - \langle \nu \partial_k \partial_k (u_i u_j^{\prime} + u_i^{\prime} u_j)\rangle - \langle \nu^{\prime} \partial_k^{\prime} \partial_k^{\prime} (u_i u_j^{\prime} + u_i^{\prime} u_j)\rangle + \langle \nu^{\prime} \partial_k^{\prime} \partial_k^{\prime} u_i^{\prime} u_j^{\prime}\rangle - 2\langle \nu^{\prime} \partial_k^{\prime} u_i^{\prime} \partial_k^{\prime} u_j^{\prime}\rangle \\
&\quad + \frac{1}{3}\langle (u_i - u_i^{\prime})(\nu \partial_j \vartheta - \nu^{\prime} \partial_j^{\prime} \vartheta^{\prime})\rangle + \frac{1}{3}\langle (u_j - u_j^{\prime})(\nu \partial_i \vartheta - \nu^{\prime} \partial_i^{\prime} \vartheta^{\prime})\rangle
\end{aligned}
\tag{2.43}
$$

where $D_{ij} = \langle d_{ij} \rangle$ and $d_{ij} = (u_i - u_i^{\prime})(u_j - u_j^{\prime})$ as defined in Eq. 2.38.

$$
T_{ij}(\boldsymbol{r}) \equiv \left\langle (u_i - u_i^{\prime}) \left(v \partial_j p - v^{\prime} \partial_j^{\prime} p^{\prime} \right) \right\rangle + \left\langle (u_j - u_j^{\prime}) \left(\frac{\partial_i p}{\rho} - \frac{\partial_i^{\prime} p^{\prime}}{\rho^{\prime}} \right) \right\rangle \tag{2.44}
$$

Using $\langle \partial_k^{\prime}(\cdot)\rangle = -\langle \cdot \rangle|_k$, and adding $\langle u_i^{\prime} u_j^{\prime} u_k \rangle|_k - \langle u_i u_j u_k^{\prime}\rangle|_k = 0$, the convective term can be written as

$$
\begin{aligned}
&\langle (\partial_k u_i u_j u_k - u_i u_j \vartheta) - (\partial_k (u_i u_j^{\prime}(u_k - u_k^{\prime})) - u_i u_j^{\prime}(\vartheta + \vartheta^{\prime}))\rangle \\
+&\langle (\partial_k^{\prime} u_i^{\prime} u_j^{\prime} u_k^{\prime} - u_i^{\prime} u_j^{\prime} \vartheta^{\prime}) - (\partial_k (u_i^{\prime} u_j (u_k - u_k^{\prime})) - u_i^{\prime} u_j (\vartheta + \vartheta^{\prime}))\rangle \\
=&\langle (u_i - u_i^{\prime})(u_j - u_j^{\prime})(u_k - u_k^{\prime})\rangle|_k - \langle d_{ij}(\vartheta + \vartheta^{\prime})\rangle + \langle u_i u_j \vartheta^{\prime} + u_i^{\prime} u_j^{\prime} \vartheta \rangle
\end{aligned}
\tag{2.45}
$$

Using the assumptions of local homogeneity,

$$
\langle u_i u_j \vartheta^{\prime}\rangle = \langle \partial_k^{\prime} u_i u_j u_k^{\prime}\rangle = -\langle u_i u_j u_k^{\prime}\rangle|_k = -\langle u_i^{\prime} u_j^{\prime} u_k \rangle|_k \tag{2.46}
$$

Therefore, the convective term can be written in a compact form as $D_{ijk}|_k - \langle d_{ij}(\vartheta + \vartheta^{\prime})\rangle$.

Adding $\nu\partial_k\partial_k u_i^{\wr}u_j^{\wr}=0$ and $\nu^{\wr}\partial_k^{\wr}\partial_k^{\wr}u_i u_j=0$, the viscous terms can be written as

$$\begin{aligned}
&\langle\nu\partial_k\partial_k u_i u_j\rangle - 2\langle\nu\partial_k u_i\partial_k u_j\rangle\\
&-\langle\nu\partial_k\partial_k(u_i u_j^{\wr}+u_i^{\wr}u_j)\rangle - \langle\nu^{\wr}\partial_k^{\wr}\partial_k^{\wr}(u_i u_j^{\wr}+u_i^{\wr}u_j)\rangle + \langle\nu^{\wr}\partial_k^{\wr}\partial_k^{\wr}u_i^{\wr}u_j^{\wr}\rangle - 2\langle\nu^{\wr}\partial_k^{\wr}u_i^{\wr}\partial_k^{\wr}u_j^{\wr}\rangle\\
&=\langle\nu\partial_k\partial_k d_{ij}\rangle + \langle\nu^{\wr}\partial_k^{\wr}\partial_k^{\wr}d_{ij}\rangle - 2\langle\nu^{\wr}\partial_k^{\wr}u_i^{\wr}\partial_k^{\wr}u_j^{\wr}+\nu\partial_k u_i\partial_k u_j\rangle\\
&=\langle d_{ij}(\nu+\nu^{\wr})\rangle|_{kk} - V_{ij}
\end{aligned} \tag{2.47}$$

where $V_{ij}=2\langle\nu^{\wr}\partial_k^{\wr}u_i^{\wr}\partial_k^{\wr}u_j^{\wr}+\nu\partial_k u_i\partial_k u_j\rangle$. We then consider the pressure-acceleration-velocity correlation term and note its structural similarity with the dilatation based viscosity term.

$$T_{ij}(\boldsymbol{r})\equiv\langle(u_i-u_i^{\wr})(v\partial_j p-v^{\wr}\partial_j p)\rangle+\langle(u_j-u_j^{\wr})(v\partial_i p-v^{\wr}\partial_i p)\rangle \tag{2.48}$$

Consider the first term in T_{ij}

$$\begin{aligned}
&\langle(u_i-u_i^{\wr})(v\partial_j p-v^{\wr}\partial_j p)\rangle\\
=&\langle u_i v\partial_j p\rangle - \langle u_i^{\wr}v\partial_j p\rangle - \langle u_i v^{\wr}\partial_j^{\wr}p^{\wr}\rangle + \langle u_i^{\wr}v^{\wr}\partial_j^{\wr}p^{\wr}\rangle\\
=&\langle u_i vp\rangle|_j - \langle\partial_j(u_i v)p\rangle - \langle u_i^{\wr}vp\rangle|_j + \langle u_i^{\wr}p\partial_j v\rangle\\
&-\langle u_i^{\wr}v^{\wr}p^{\wr}\rangle|_j - \langle\partial_j^{\wr}(u_i^{\wr}v^{\wr})p^{\wr}\rangle + \langle u_i v^{\wr}p^{\wr}\rangle|_j + \langle u_i p^{\wr}\partial_j^{\wr}v^{\wr}\rangle
\end{aligned} \tag{2.49}$$

Using $\langle u_i vp\rangle|_j-\langle u_i^{\wr}v^{\wr}p^{\wr}\rangle|_j=0$ and $-\langle u_i^{\wr}vp\rangle|_j=\langle vp\partial_j^{\wr}u_i^{\wr}\rangle, \langle u_i v^{\wr}p^{\wr}\rangle|_j=\langle v^{\wr}p^{\wr}\partial_k u_i\rangle$, we can write T_{ij} in the form

$$\begin{aligned}
&\langle(u_i-u_i^{\wr})(v\partial_j p-v^{\wr}\partial_j p)\rangle\\
=&-\langle pv\partial_j u_i\rangle - \langle pu_i\partial_j v\rangle + \langle vp\partial_j^{\wr}u_i^{\wr}\rangle + \langle u_i^{\wr}p\partial_j v\rangle\\
&-\langle p^{\wr}v^{\wr}\partial_j^{\wr}u_i^{\wr}\rangle - \langle p^{\wr}u_i^{\wr}\partial_j^{\wr}v^{\wr}\rangle + \langle v^{\wr}p^{\wr}\partial_j u_i\rangle + \langle u_i p^{\wr}\partial_j^{\wr}v^{\wr}\rangle\\
=&-\langle(pv-p^{\wr}v^{\wr})(\partial_j u_i-\partial_j^{\wr}u_i)\rangle - \langle(p\partial_j v-p^{\wr}\partial_j^{\wr}v^{\wr})(u_i-u_i^{\wr})\rangle
\end{aligned} \tag{2.50}$$

Therefore, in its compact form, $T_{ij}=\langle-2\delta\left(\frac{p}{\rho}\right)\delta S_{ij}-\delta\left(p\partial_j\frac{1}{\rho}\right)\delta u_i-\delta\left(p\partial_i\frac{1}{\rho}\right)\delta u_j\rangle$
The dilatational viscous term, on account of its structural similarity with the pressure

acceleration term is

$$V_{ij}^{\vartheta} = \frac{1}{3}\langle -2\delta\left(\vartheta\nu\right)\delta S_{ij} - \delta\left(\vartheta\partial_j\nu\right)\delta u_i - \delta\left(\vartheta\partial_i\nu\right)\delta u_j\rangle \tag{2.51}$$

With the assumption local homogeneity, the compressible variable-density Navier-Stokes equations result in the following equation for the two point velocity difference correlation

$$\dot{D}_{ij}(\boldsymbol{r}) + D_{ijk}(\boldsymbol{r})|_k - \langle d_{ij}(\vartheta + \vartheta')\rangle = -T_{ij}(\boldsymbol{r}) + \langle(\nu + \nu')d_{ij}\rangle|_{kk} - E_{ij}(\boldsymbol{r}) + V_{ij}(\boldsymbol{r}) \tag{2.52}$$

where $D_{ijk} = \langle d_{ij}(u_k - u_k'\rangle$.

The compressible variable-density version of the generalized Kolmogorov 4/5 law for homogeneous turbulence, derived in Frisch and Lindborg follows. Taking the trace of the $\dot{D}_{ij}$ equation, we obtain

$$\dot{D}_{ii} + D_{iik}|_k - \langle d_{ii}(\vartheta + \vartheta')\rangle = -T_{ii} + \langle(\nu + \nu')d_{ii}\rangle|_{kk} + E_{ii} + V_{ii}^{\vartheta} \tag{2.53}$$

The contracted dilatational viscous term is

$$V_{ii}^{\vartheta} = \frac{1}{3}\langle -2(\nu\vartheta\vartheta + \nu'\vartheta'\vartheta') - 2(\nu + \nu')\theta\theta' - \delta\left(\vartheta\partial_j\nu\right)\delta u_i - \delta\left(\vartheta\partial_i\nu\right)\delta u_j\rangle \tag{2.54}$$

and $E_{ii} = 2\langle\nu'\partial_k' u_i'\partial_k' u_j' + \nu\partial_k u_i\partial_k u_j\rangle$ If ϵ is defined as the dissipation of the ensembled averaged specific energy $\langle u_i u_i/2\rangle$, then we have $E_{ii} - \frac{2}{3}\langle\nu\vartheta\vartheta + \nu'\vartheta'\vartheta'\rangle = -4\epsilon$. For locally stationary turbulence ($r \ll L$) and $r \gg \eta$, the time-dependent, the viscous diffusion and viscous dilatation terms are neglected, so that we have

$$D_{iik}(\boldsymbol{r})|_k - \langle d_{ii}(\boldsymbol{r})\underline{\vartheta}\rangle - 2\left\langle\delta\left(\frac{p}{\rho}\right)\delta\vartheta\right\rangle - 2\left\langle\delta\left(p\partial_i\frac{1}{\rho}\right)\delta u_i\right\rangle \approx -4\epsilon \tag{2.55}$$

In the limit of constant-density incompressible turbulence, we have usual relation

$$D_{iik}(\boldsymbol{r})|_k \approx -4\epsilon \tag{2.56}$$

We interpret the terms due to compressibility and variable-density from a phenomenological standpoint. The term $d_i i\underline{\vartheta}$ is related to the mean (or large-scale) compression or dilatation. Compression results in increased dissipation rate ϵ. The other

two terms are related to dilatation and specific volume increments. These terms can change their sign depending on the nature of the fields.

Chapter 3

Numerics

3.1 Introduction

In this chapter, we describe the numerical method used in this thesis to solve the governing equations (Chapter 2). Numerical challenges associated with mixing and reactions in the context of large-eddy simulations have previously been discussed in Subbareddy et al. [112]. The governing equations are solved with a finite volume method using inviscid fluxes that employ upto 6th order polynomial interpolation over neighboring volumes. To preserve scalar boundedness, the well known linear scaling limiters of Zhang and Shu [131], adapted in the work by Kartha et al. [59] and Subbareddy et al. [111] are employed. Two dimensional simulations of scalar interface evolution in the presence of vorticity are carried out to demonstrate adequate representation of active/passive scalar dynamics.

3.2 Finite-volume framework for resolved-scale variables

The equations for large eddy simulations can be written in the form

$$\frac{\partial U}{\partial t} + \frac{\partial F_j}{\partial x_j} = W + \mathcal{S} \tag{3.1}$$

where U denotes the filtered (coarse-grained) representation of the solution variables, F and W are the flux and the source terms obtained from resolved-scale solution variable

set U. We avoid the overlines on the solution variables in this chapter for simplicity.

$$U = (\rho_s, \rho u, \rho v, \rho w, \rho\phi, E)^T, W = (\omega_s, 0, 0, 0, \omega_\phi, 0)^T \tag{3.2}$$

The subscript s denotes the mass conservation equation for the gas species s. $\mathcal{S}$ is the subgrid-scale contribution arising from coarse-graining at filter width Δ which serves as a cut-off on the observer length-scale to regularize the fields for their accurate representation on a computational grid. In the limit of direct numerical simulations, $\mathcal{S} \ll \partial_j F_j^{\text{vis}}$ must ideally hold, constraining the non-smoothness of the fields so resolved. The flux F_j consists of the inviscid and the viscous components.

$$F_j^{\text{inv}} = \begin{pmatrix} \rho_s u_j \\ \rho u u_j + p\delta_{1j} \\ \rho v u_j + p\delta_{2j} \\ \rho w u_j + p\delta_{3j} \\ \rho\phi u_j \\ (E+p)u_j \end{pmatrix}, F_j^{\text{vis}} = \begin{pmatrix} J_j^s \\ \sigma_{1j} \\ \sigma_{2j} \\ \sigma_{3j} \\ J_j^\phi \\ q_j + u_k\sigma_{kj} \end{pmatrix} \tag{3.3}$$

where density $\rho = \sum_s \rho_s$ and E is the total energy, sum of internal and kinetic energy.

$$E = \rho e + \frac{1}{2}\rho\left(u^2 + v^2 + w^2\right) + \sum_s \rho_s h_s^0 \tag{3.4}$$

The thermal energy of the gas mixture following the ideal as law is

$$\rho e = \sum_s \rho_s C_{v,s} T = \sum_s \frac{p_s}{\gamma_s - 1} \tag{3.5}$$

where γ_s is the specific heat ratio for species s. Integrating the conservation law over a finite volume V and assuming that U is constant in the volume, we obtain equation 3.6. In the semi-dicrete form, the surface integral is evaluated on the discrete faces f of the finite volume.

$$\frac{\partial U}{\partial t} + \frac{1}{V}\oint_{\partial V} (F_s \hat{n}_s)\, dS = W \tag{3.6}$$

$$\frac{\partial U}{\partial t} + \frac{1}{V}\sum_{\mathrm{f}} \left(F_f \hat{n}_f\right) S_f = W + \mathcal{S} \tag{3.7}$$

3.3 Inviscid flux

This subsection discusses the construction of the inviscid or the convective flux (computed from the resolved scale variables in LES). The base flux scheme employed in the present work is the kinetic energy consistent flux described in Subbareddy and Candler [109]. The Roe-type (or modified Steger-Warming type) approximate solution to the Riemann problem at the face with U^L and U^R states across the face f can be written in the form

$$F_f = \frac{1}{2}\left(F\left(U^L\right) + F\left(U^R\right)\right) - \frac{1}{2}\left(\left(R^{-1}|\Lambda|R\right)_f \left(U^R - U^L\right)\right) \tag{3.8}$$

$$= F_f^{\text{central}} + D_f \tag{3.9}$$

where the first term is a central portion of the flux and the second term represents the dissipative portion due to upwinding. The matrices in the dissipative portion are obtained from the eigendecomposition of the inviscid Jacobian $\partial F/\partial U = R\Lambda R^{-1}$. Λ is the diagonal matrix of the eigenvalues of the hyperbolic system of equations. The term $R|\Lambda|R^{-1}$ can be written in a compact form [14] when accounting for the sonic glitch correction that avoids representation of zero-speed characteristic waves in the solution.

$$R^{-1}|\Lambda|R = D_1 D_2 + D_3 D_4 + |\Lambda| I, \quad \text{where} \tag{3.10}$$

$$D_1 = \frac{1}{a}\begin{pmatrix} c_0 & c_0 u + a c_1 n_x & c_0 v + a c_1 n_y & c_0 w + a c_1 n_z & c_0 h_0 + a c_1 u' \end{pmatrix}^T, \tag{3.11}$$

$$D_2 = \begin{pmatrix} p_{\rho_s} & -u p_E & -v p_E & -w p_E & p_E \end{pmatrix} \tag{3.12}$$

$$D_3 = \begin{pmatrix} c_1 & u c_1 + c_0 n_x a & v c_1 + c_0 n_y a & w c_1 + c_0 n_z a & p_E \end{pmatrix}^T \tag{3.13}$$

$$D_4 = \begin{pmatrix} -u' & n_x & n_y & n_z & 0 \end{pmatrix} \tag{3.14}$$

$$p_E = \frac{1}{\rho}\left.\frac{\partial p}{\partial e}\right|_\rho \tag{3.15}$$

and the sonic glitch correction is incorporated with a small number ϵ.

$$c_0 = \frac{a}{2}\left(\sqrt{\frac{\lambda^+}{a}+\epsilon^2}+\sqrt{\frac{\lambda^-}{a}+\epsilon^2}-\sqrt{\frac{u'}{a}+\epsilon^2}\right) \tag{3.16}$$

$$c_1 = \frac{a}{2}\left(\sqrt{\frac{\lambda^+}{a}+\epsilon^2}-\sqrt{\frac{\lambda^-}{a}+\epsilon^2}\right) \tag{3.17}$$

The face normal velocity component is denoted by u'. To reduce dissipation, D_f is coupled with a flow-dependent shock or discontinuity sensor $\alpha \in [0,1]$.

The central part of the flux can be constructed with higher order polynomial representations of the conserved variable state at the face U_f. Similarly, the left and the right states in the dissipative part of the flux can also be reconstructed. In this work, U^R and U^L are limited reconstructions with information from two neighbour cells from either side of the face. For turbulent flows, high order schemes are preferred with high-resolution modified wavenumber properties, ensuring low dissipation and low dispersion error for a wide range of resolvable wavelengths. We use an explicit sixth order KEC scheme for the symmetric portion of the flux. By kinetic-energy-consistent, we are implying that the flux for kinetic energy at face f in the semi-discrete form is given by

$$\sum_f \left(\rho k u_n S\right)_f = \sum_f \frac{1}{2}\left(u^R u^L + v^R v^L + w^R w^L\right)\left(\rho u' S\right)_f \tag{3.18}$$

where k is the kinetic energy, S is the face area and u_n the face normal velocity component. This flux is closely related to skew-symmetric form of the non-linear advection term and conserves k in the incompressible limit. The sixth order accuracy is obtained by polynomial reconstruction from neighbouring cell values and gradients. For example, the face state on a uniform grid (Figure 3.1) is interpolated as

$$\phi_f = \frac{\phi_L+\phi_R}{2} + \frac{8}{15}\left(\nabla\phi_L\cdot\Delta x_{f,L} + \nabla\phi_R\cdot\Delta x_{f,R}\right) - \frac{1}{45}\left(\nabla\phi_{L2}\cdot\Delta x_{f,L2} + \nabla\phi_{R2}\cdot\Delta x_{f,R2}\right) \tag{3.19}$$

The symmetric stencil for the central part is extremely dispersive for scalar convection and violates the boundedness properties of a conserved scalar. This is an important

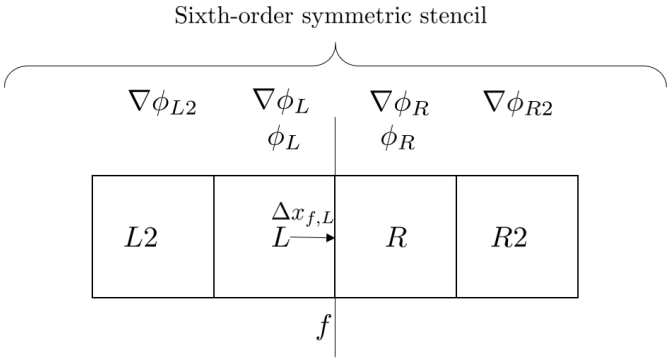

Figure 3.1: Illustration of the sixth order polynomial interpolation stencil for variable value at the face f.

property necessary for accurate simulations of reacting flows. We employ MUSCL interpolation for the states U^L and U^R for D_f, with a second order symmetric interpolation for $R|\Lambda|R$ that reverts to first order for high Mach number shocks using a pressure-difference sensor. This form of the dissipative part D_f cannot mitigate the boundedness issue. Therefore, we work with a limiting framework developed by Subbareddy et al. [112] for the high order representation of the central part.

3.3.1 Bound preserving linear scaling limiters

Unlike the velocity and the thermodynamic fields, the discrete convective operator for scalars must satisfy the boundedness property of the scalar. The property implies

$$\begin{aligned} &\text{If } m \leq u^n(x) \leq M, \quad \forall V \\ &\text{then } m \leq u^{n+1}(x) \leq M, \quad \forall V \end{aligned} \tag{3.20}$$

Zhang and Shu [131] proposed the following linear scaling limiter that scales the interpolant polynomial about its average, and thereby maintains its accuracy.

$$\tilde{p}_i(x) = \overline{u}_i^n + \theta_i \left(p_i(x) - \overline{u}_i^n\right), \quad \theta_i = \min\left\{\left|\frac{M - \overline{u}_i^n}{M_i - \overline{u}_i}\right|, \left|\frac{m - \overline{u}_i^n}{m_i - \overline{u}_i}\right|, 1\right\} \tag{3.21}$$

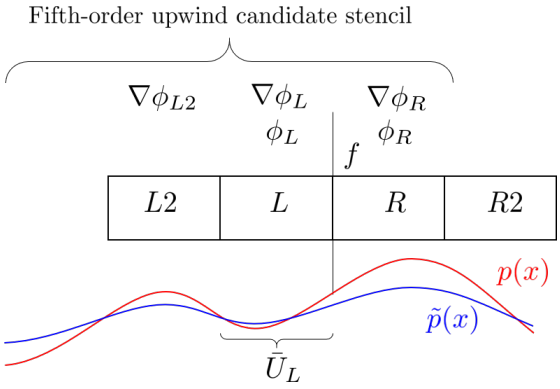

Figure 3.2: Illustration of the linear scaling limiter applied to the fifth order upwinded stencil

where

$$M_j = \max_{x \in S_j} p_j(x), \quad m_j = \min_{x \in S_j} p_j(x) \tag{3.22}$$

where S_j is the set of quadrature points over which the polynomial $p_j(x)$ is represented. It must be noted that this type of limiting does not enforce non-oscillatory, total-variation diminishing or total variation bounded behavior. For the sixth-order solution state interpolation to evaluate F_f^{central}, the scaling limiter is applied to the two upwinded fifth order candidate stencils. This is illustrated in Figure 3.2. It is important to note that only a specific choice of the reconstructed thermodynamic variable set works with the scaling limiter to avoid aphysical overshoots in the solution fields across sharp discontinuities. This variable set is (ρ_s, p). T can be used as a reconstructed face variable only in the absence of limiting. Use of ρ_s instead of Y_s is crucial to avoid overshoots in temperature, as is also discretely reconstructs and limits the moles of each species n_s on the face.

3.3.2 Dissipative component for scalar fluxes

The dissipative part of the flux, as we mention earlier, employs a shock sensor α to avoid excessive dissipation in vorticity dominated flows. However, in the presence of large gradients in the scalar field, such as across a material interface, the dissipative fluxes in the scalar equation must be active in order to prevent dispersive oscillations. Therefore, α must incorporate a scalar discontinuity sensor in addition to a shock sensor.

Kartha et al. [59] proposed an effective switch that appears as a by-product of the linear scaling limiter.

$$\alpha_\phi = \min\left[1, \max\left(1-\theta_L, 1-\theta_R\right)\right] \tag{3.23}$$

However, as outlined in [112], the switch is over-conservative and results in excess dissipation in mass, momentum and energy even if the gas species are passive in nature. In the paper, the authors carefully control the dissipation using an artificial compression method (ACM)-type switch. In the present work, we use the sensor of the form provided in Equation 3.23, and explore some alternate strategies that help reduce dissipation in the vorticity field and result in stable evolution of a sharp scalar interface.

One method to reduce dissipation involves applying the sensors to the specific characteristic variables in D_f. For example, we can distinguish between the sensor that activates dissipation on the characteristic variables corresponding to species mass ρ_s from that applied to face-parallel velocity component and the acoustic waves. If we denote the two sensors by α_ρ and α respectively, Equation 3.10 becomes

$$R^{-1}|\Lambda^\alpha|R = D_1^\alpha D_2 + D_3^\alpha D_4 + D_5^\alpha \tag{3.24}$$

where

$$D_1^\alpha = \frac{1}{a}\begin{pmatrix} c_0^\rho & c_0^\rho u + a c_1^\alpha n_x & c_0^\rho v + a c_1^\alpha n_y & c_0^\rho w + a c_1^\alpha n_z & c_0^\rho h_0 + a c_1^\alpha u' \end{pmatrix}^T \tag{3.25}$$

$$D_3^\alpha = \begin{pmatrix} c_1^\alpha & u c_1^\alpha + c_0^\alpha n_x a & v c_1^\alpha + c_0^\alpha n_y a & w c_1^\alpha + c_0^\alpha n_z a & p_E \end{pmatrix}^T \tag{3.26}$$

$$c_0^\rho = c_0(\alpha\lambda^+, \alpha\lambda^-, \alpha_\rho u'),\ c_0^\alpha = c_0(\alpha\lambda^+, \alpha\lambda^-, \alpha u'),\ c_1^\alpha = c_1(\alpha\lambda^+, \alpha\lambda^-, \alpha u') \tag{3.27}$$

For ideal gases, D_5^α is

$$D_5^\alpha = \begin{pmatrix} \alpha_\rho\lambda & & & & \\ -uu'(\alpha-\alpha_\rho) & \alpha\lambda & & & \\ -vu'(\alpha-\alpha_\rho) & & \alpha\lambda & & \\ -wu'(\alpha-\alpha_\rho) & & & \alpha\lambda & \\ u_iu_i(\alpha_\rho-\alpha) & uu'(\alpha-\alpha_\rho) & vu'(\alpha-\alpha_\rho) & wu'(\alpha-\alpha_\rho) & \alpha_\rho\lambda \end{pmatrix} \tag{3.28}$$

In principle, the switch on the face-parallel component of the velocity can be off even in

the presence of shocks, and every individual gas species can employ a sensor based on its field. However, for simplicity and robustness, α_ρ corresponds to the most conservative values obtained from the scaling limiter.

Another method to reduce dissipation in the solution fields is to ensure that the passive scalar flux is decoupled from the flux of mass, momentum and energy discretely. The dissipation in the presence of a sharp scalar discontinuity then does not require dissipation in the flow variables to be activated. The shock and the scalar nonsmoothness sensors therefore activate different dissipative parts of the flux. If the subscript c denotes the central part of the flux and D denotes the dissipative part of the flux for the corresponding variables, the decoupling can be achieved in the following manner

$$(\rho u')_f = \rho_c u'_c + \alpha D_\rho \tag{3.29}$$

$$(\rho \phi u')_f = (\rho u_i)_f \phi_f + \alpha_\phi (D_\rho \phi_f - D_{\rho\phi}) \tag{3.30}$$

In the case of multiple species, we have $D_\rho \phi_c = D_{\rho\phi}$ which ensures consistency in the mass flux. Here α_ϕ is the discontinuity detector in the scalar field ϕ and is independent of α, which detects shock and density jumps.

3.3.3 Two-dimensional numerical tests

We now present some numerical tests which demonstrate the capability of the method to handle flows with stirring and mixing due to interfacial instabilities. Of particular interest are the flows where baroclinic torque is active and modifies the vorticity content in the domain. The tests are two-dimensional and inviscid. Therefore, specific vorticity ω/ρ is conserved in the absence of baroclinic torque.

Material interface wrapping by an isentropic vortex

The first case corresponds to wrapping of a material interface by an isentropic vortex (see Figure 3.3 for the schematic). The test case evolves with the scalar fields being wound into a spiral by the vortex (Figure 3.4). The flow tests the numerical method for handling stable and robust convection of sharp interfaces, in the presence of conserved vorticity. Figure 3.5 shows the thickness of the interface relative to the grid resolution at late time. The initial interface is spread across 4 grid cells.

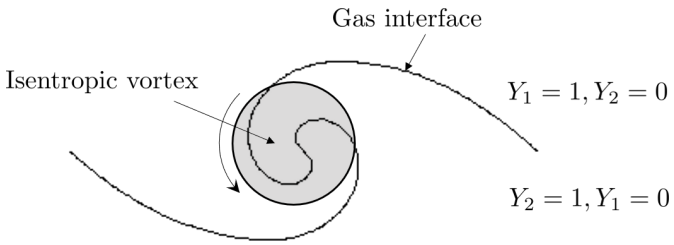

Wrapping of material interface by a vortex: initial setup

Figure 3.3: Winding material interface: schematic

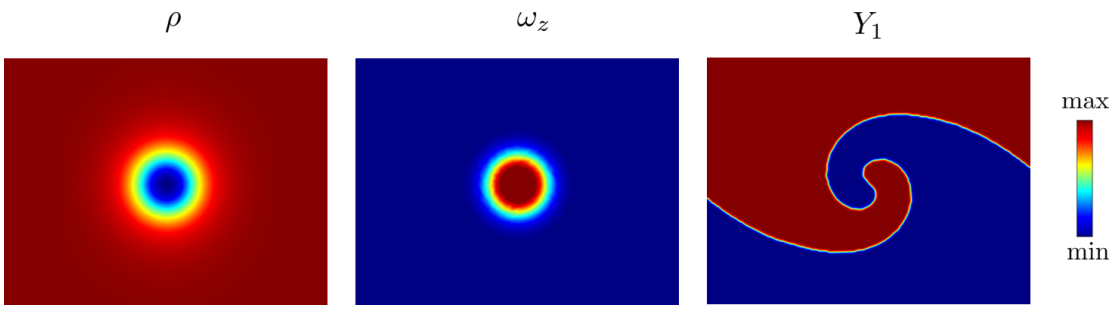

Figure 3.4: Winding material interface: initial conditions

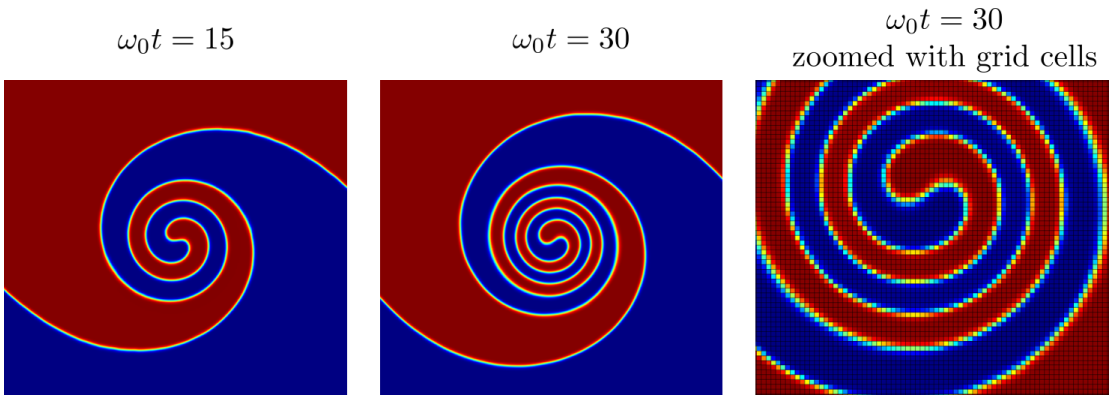

Figure 3.5: Winding material interface: mass fraction field at different time instances.

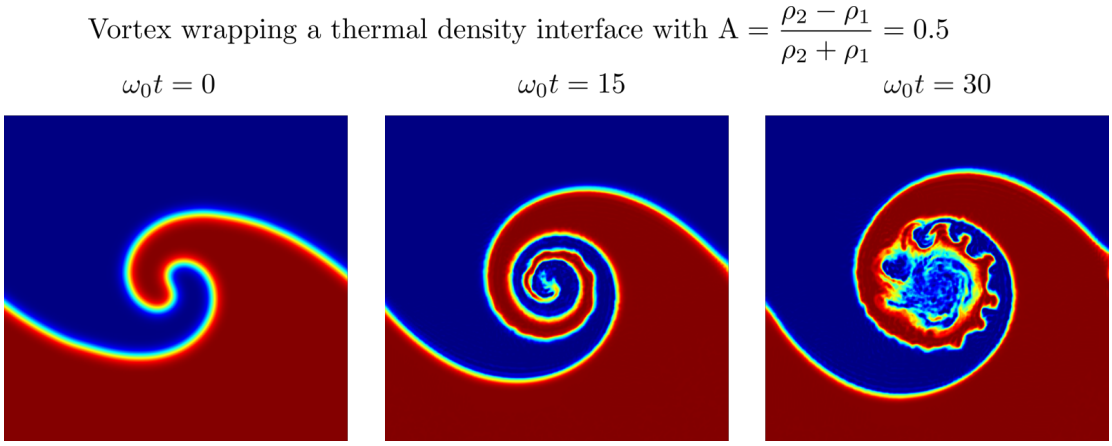

Figure 3.6: Winding density interface: density field at different time instances

Density interface wrapping by initially axisymmetric vortex

The second test is similar to the first case, except the initial density field consists of an interface being wrapped by a vortex. The density mismatch is thermal in nature and corresponds to an interface in temperature. In this scenario, vorticity in the domain does not remain conserved and is affected by barolinic torque. The torque is produced by the interface misaligning with the radial pressure gradient due to the low-pressure vortex core. Compared to the previous case, Figure 3.6 shows that the interface becomes unstable and quickly leads to chaotic mixing at the core. Baroclinic torque plotted in Figure 3.7 explains the development of a vorticity spiral in addition to the initial content at the core. The small-scale fluctuations in the baroclinic torque correspond to the rapid pressure fluctuations, which are acoustic in nature, while the mean background torque corresponds to the slow hydrodynamic pressure gradients.

Kelvin-Helmholtz rollup of a material-vorticity sheet

In the previous test case, the dissipation due to the sharp scalar interface on the vorticity field is not discernible. We therefore design a stringent test case where a thin layer of gas species coexists on a vorticity sheet (Figure 3.8). This is inspired by the situation in non-premixed reacting shear layers where under-resolved thin sheets of intermediate and final products exist at the edge of the shear layer. The setup of the 2D temporal shear layer is taken from the reference[125]. The vortex sheet is perturbed with a streamwise

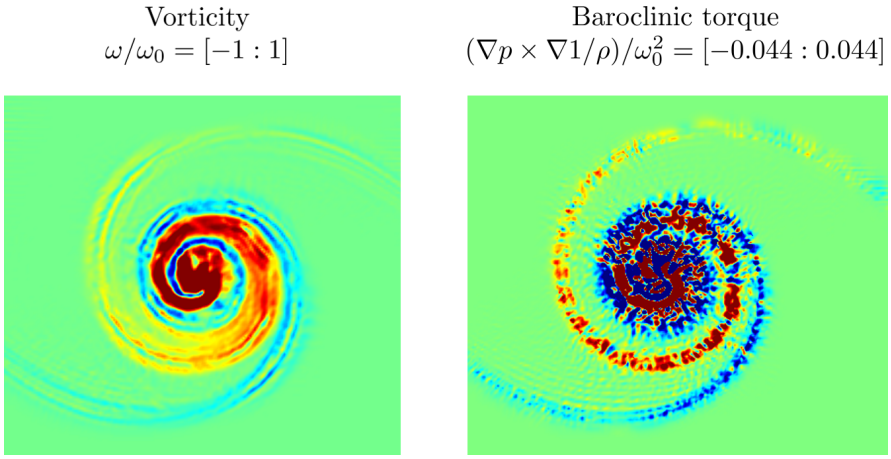

Figure 3.7: Winding density interface: baroclinic torque and deposited vorticity

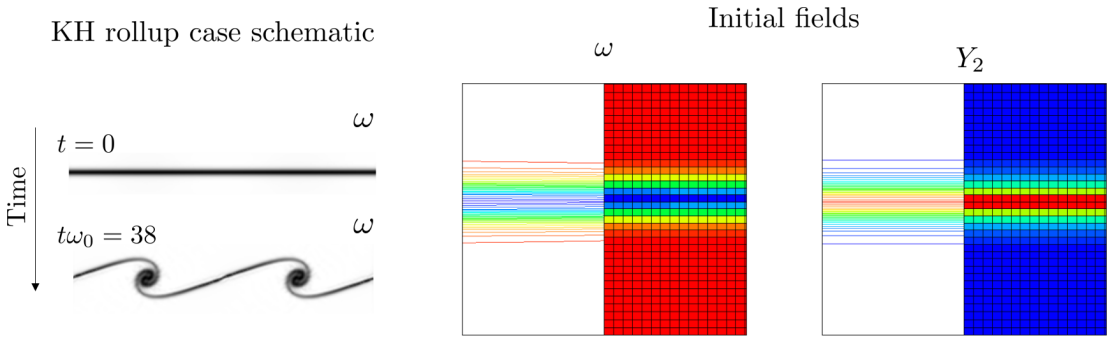

Figure 3.8: KH rollup of a material-vorticity sheet: initial conditions

wavelength causing the shear layer to roll-up into Kelvin-Helmholtz billows. However, the dissipation required for ensuring boundedness of the thin layer of gas species can cause vorticity to dissipate resulting in a weak roll-up. This test case demonstrates the numerical decoupling of the passive scalar dynamics from the dynamics of flow variables. Figures 3.9 and 3.10 show the comparison of the flow variables with and without the use of the decoupling methodology.

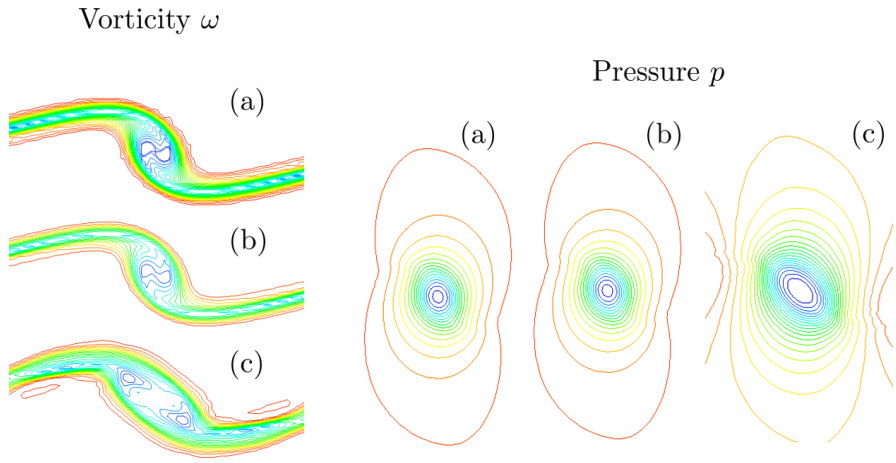

Figure 3.9: KH rollup of a material-vorticity sheet: flow variable contours corresponding to (a) no interfacial species and interfacial species with (b) decoupled scalar dissipation and (c) MSW based dissipation

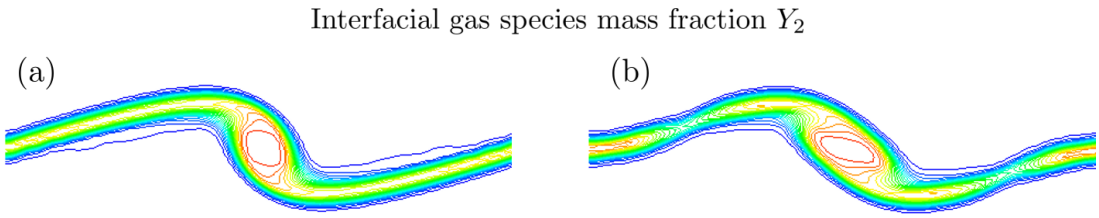

Figure 3.10: KH rollup of a material-vorticity sheet: interface species mass fraction contours using (a) decoupled scalar dissipation and (b) MSW based dissipation

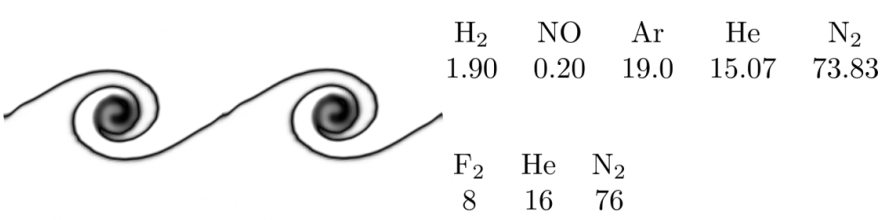

Figure 3.11: 2D reacting mixing layer: mole fractions in the top and bottom streams

Kelvin-Helmholtz rollup of a reacting interface

The previous test cases transport binary gas species passively. In this test case, we demonstrate that the low-dissipation numerical method is effective in the case of reacting scalars. The constituents in the top and the bottom stream of the 2D mixing layer are shown in Figure 3.11. The reaction system involves H2-F2 chemistry. The following reaction set is used, with the reaction rate defined as $k = AT^{\eta}\exp(-E_a/RT)$. Baroclinic torque and vorticity dilatation are active in the reaction zone (Figure 3.12)

							ΔQ	A	η	E_a/R
H	+	F_2	$\rightleftharpoons$	HF	+	F	-133.9	3.0×10^6	1.5	845.5
NO	+	F_2	$\rightleftharpoons$	NOF	+	F	-76.6	4.2×10^8	0.0	1150.0
F	+	H_2	$\rightleftharpoons$	HF	+	H	-411.3	2.6×10^9	0.5	307.0

Table 3.1: Reaction set and rate parameters for the 2D reacting mixing layer case

and are associated with large density gradient zones at the edges of the mixing layer. A comparison of the fluxes with and without the low-dissipation scalar flux is shown in Figure 3.13.

Single-mode Richtmyer-Meshkov instability

The previous test cases considered material interface evolution in the presence of a vortex and a vortex sheet. We now consider a test case where a shock deposits vorticity on a perturbed density interface which then later evolves under the action of the deposited vorticity. The test case is the classical Richtmyer-Meshkov instability, the initial setup for which is illustrated in Figure 3.14. The initial vorticity due to the baroclinic torque

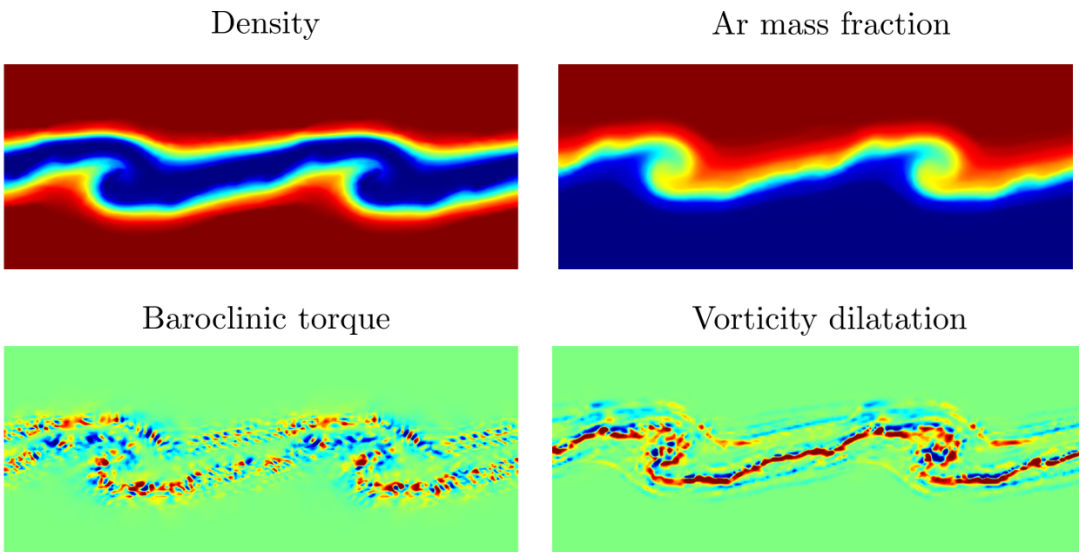

Figure 3.12: 2D reacting mixing layer: fields computed using decoupled scalar dissipation

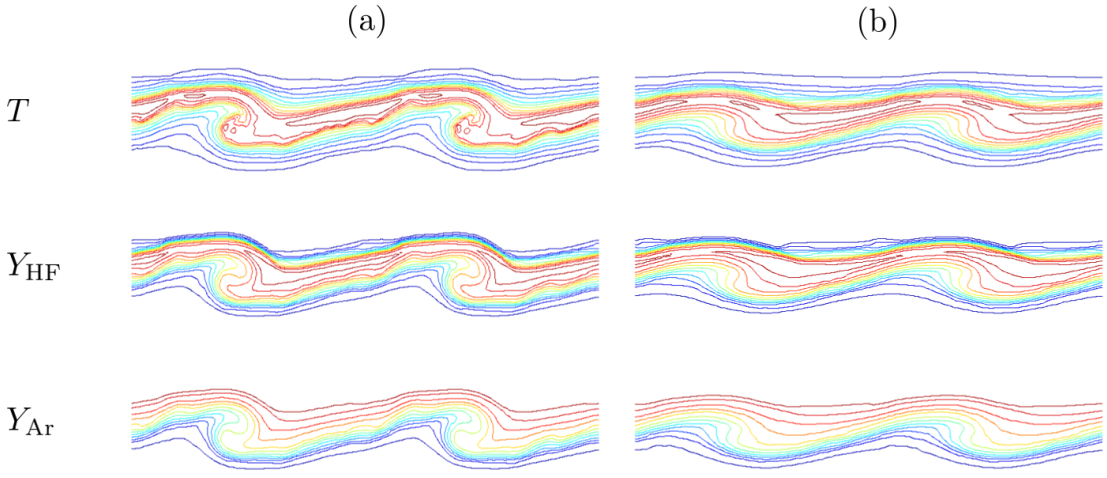

Figure 3.13: 2D reacting mixing layer: comparison of fields using (a) decoupled scalar dissipation and (b) MSW based dissipation

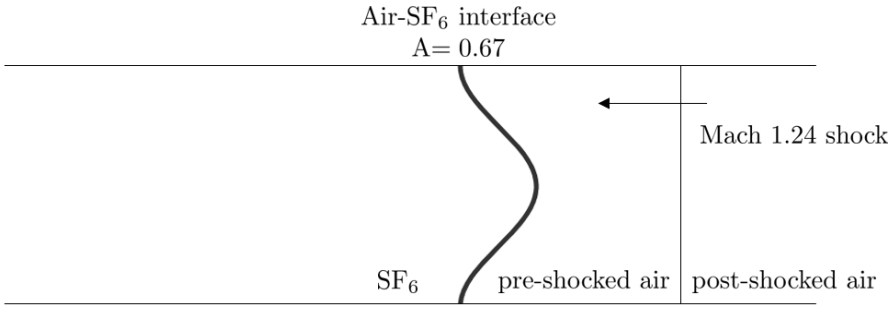

Figure 3.14: Single mode Richtmyer-Meshkov instability: schematic of the initial condition.

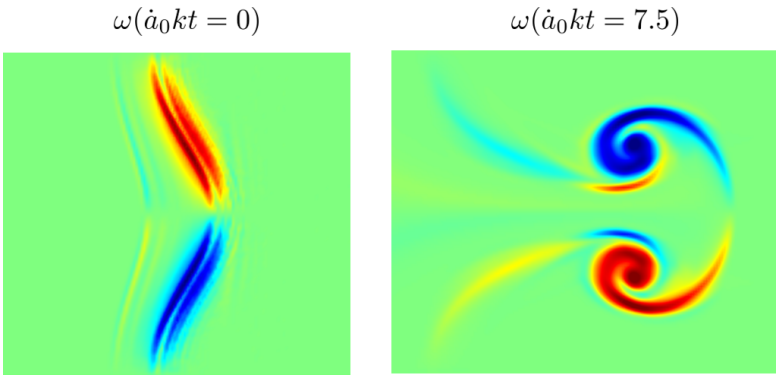

Figure 3.15: Single mode Richtmyer-Meshkov instability: vorticity evolution.

and its non-linear evolution are shown in Figure 3.15. The numerical method in the present work captures the bubble and the spike evolution adequately. A qualitative and quantitative comparison with the experiments of Collins and Jacobs [24] is shown in Figure 3.16 and Figure 3.18 respectively. The initial density interface is of a finite thickness spanning 8 grid cells. Evolution of the instability in the case of a sharp discontinuity is also shown. The low dissipation scalar flux method retains the interface quality even at late times (Figure 3.17).

3.4 Viscous fluxes and subgrid-scale terms

The viscous terms use second-order spatially accurate operators. While the order of the resulting scheme is lower than the inviscid flux, bulk quantities of interest are

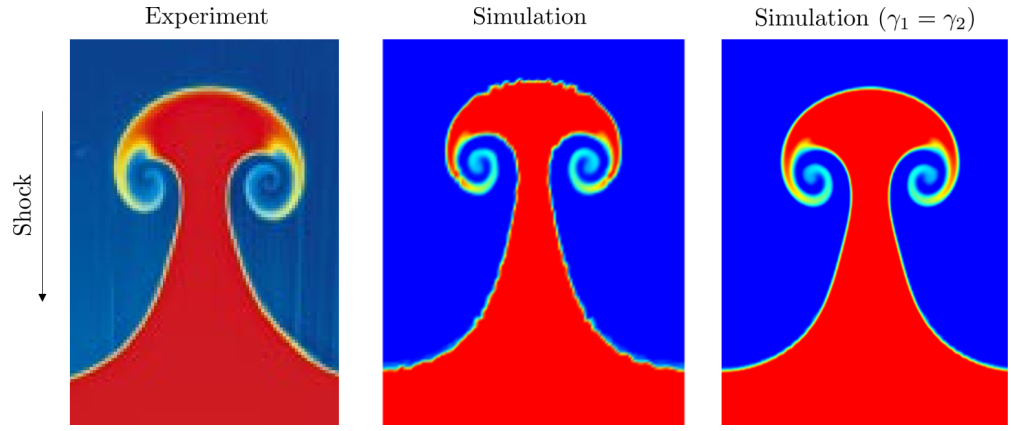

Figure 3.16: Single mode Richtmyer-Meshkov instability: qualitative comparison with experimental visualization.

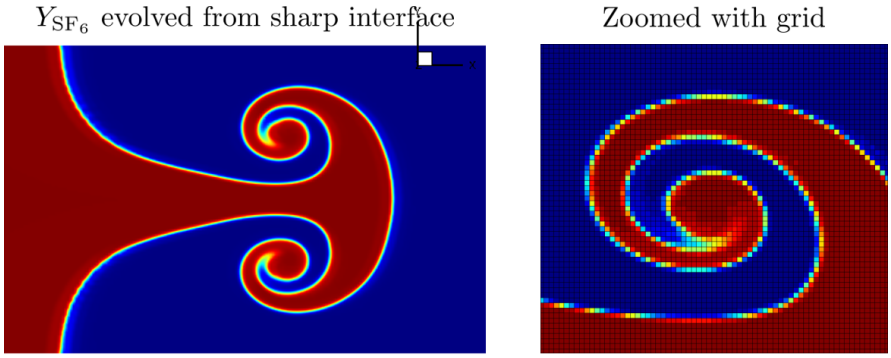

Figure 3.17: Single mode Richtmyer-Meshkov instability: evolution of a sharp interface.

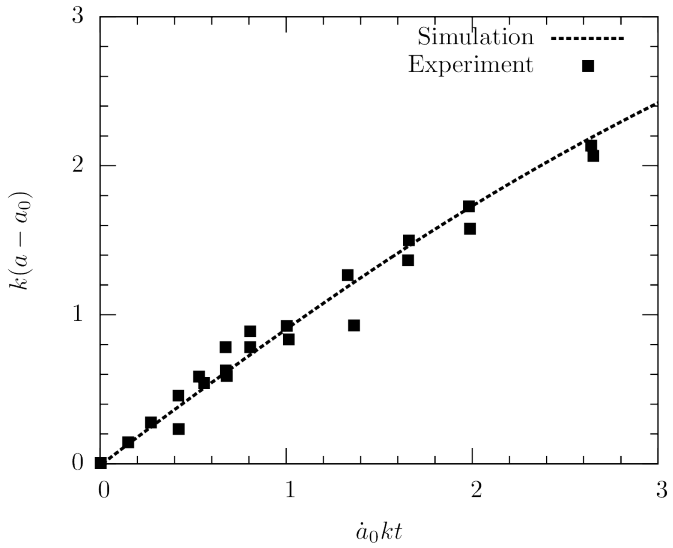

Figure 3.18: Non-dimensional amplitude of the single mode Richtmyer-Meshkov instability as a function of non-dimensional time: comparison with experiment

not affected severely. In large eddy simulations, where the subgrid-scale terms are responsible for a large fraction of energy dissipation, the order of accuracy of viscous terms is less important. A smaller stencil for the viscous terms saves communication time between different processors. The subgrid-scale terms are also computed using second order approximations for spatial gradients.

3.5 Time integration

For DNS calculations, we employ explicit time integration. The third order, strong-stability-preserving explicit Runge-Kutta scheme by Gottlieb et al. [46] is used. For stiff chemistry source terms in large-eddy simulations, a time-splitting method to exploit the difference in flow and reaction time scales is employed. The reaction source terms are integrated individually in each cell using the fourth-order semi-implicit GRK4A method of Kaps and Rentrop [57]. The Strang splitting [108] is used, resulting in second order time accuracy.

Chapter 4

Variable-density stretched spiral vortex analysis

To understand the qualitative effect of density variations on the energy of small scales, we consider a model for turbulent fine structure. One model for turbulent fine structure was proposed by Lundgren [73] and is also the theoretical basis of the stretched-vortex family of subgrid models [79]. In this chapter, we consider the properties of this model spectrum in the presence of variable-density mixing and enstrophy production by baroclinic torque, and discuss possible implications for subgrid-scale modeling. Since subgrid modeling has numerical, physical and discrete operator specific components to it, we do not derive an SGS model from this work. Only physical effects within the stretched-vortex framework are explored.

4.1 The stretched-spiral vortex model for turbulent fine scales

The stretched-spiral model for small-scale turbulent structures proposed by Lundgren [73, 74] analytically predicts the Kolmogorov $k^{-5/3}$ range in the energy spectrum. This model is an ensemble of two-dimensional vortices with a spiral pattern, stretching in an axisymmetric strain field (a representation the effect of large scale structures). The

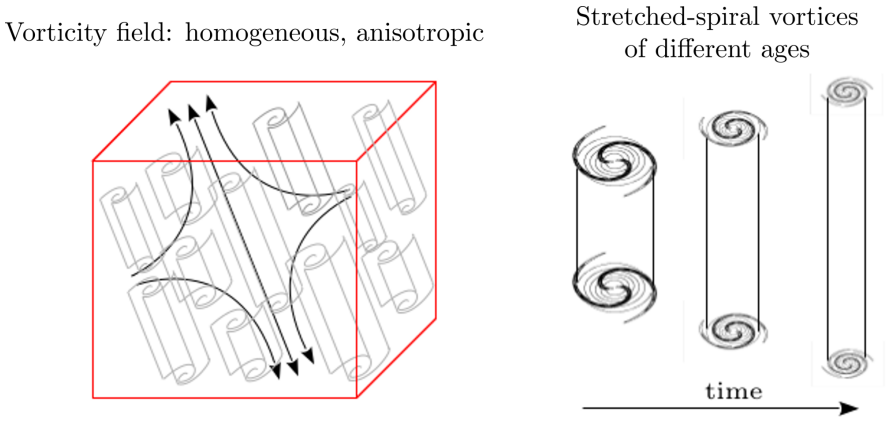

Figure 4.1: Illustration of the Lundgren stretched-spiral vortex model for turbulent fine scales

spectrum is attributed to energy cascade arising out of stretching and differential rotation. Spiral vortices are generated by unstable multi-modal sheet roll-ups [55] and vortex merging. This model is a more general case of Townsend's models of randomly oriented Burgers vortices that predict a k^{-1} energy spectrum scaling as well Burgers sheets that predict a k^{-2} scaling law. It must be noted that this picture of cascade wherein energy is transferred to smaller scales by winding of vorticity field in presence of axial strain is purely kinematic. The dissipation primarily occurs in the spiral structure. Lundgren showed the $k^{-5/3}$ spectrum is independent of the nature of the spiral structure.

The stretched-spiral vortex model originally satisfies the constant density Navier-Stokes dynamics. We investigate the effect of variable-density fluid on the three-dimensional energy spectrum, the $k^{-5/3}$ subrange in particular. The formulation of Lundgren's model decouples the time-evolution of the 2-D flow structure and the calculation of the 3D energy spectrum. This allows for two-dimensional numerical computations of variable-density spiral vortices which can be used to generate the 3-D energy spectra in the presence of a background axially strained field.

We summarize the dynamics of the Lundgren model. Consider the two-dimensional vorticity field $\omega_{2D}(x, y, t)$ superposed on an axisymmetric strain flow with the velocity field $(u_x, u_y, u_z) = (-ax/2, -ay/2, az)$ where $a(t)$ is the rate of strain. The stretched

vorticity field is then given by the expression

$$\omega(x,y,t) = S(t)\omega^{2D}[S(t)^{1/2}x, S(t)^{1/2}y, T(t)] \tag{4.1}$$

$$S(t) = \exp\left(\int_0^t a(t')dt'\right) \tag{4.2}$$

$$T(t) = \int_0^t S(t')dt' \tag{4.3}$$

where $S(t)$ is the amount by which the vortex tube is stretched and $T(t)$ is the strained time. An ensemble of vortices of different ages stretched in the strain field is used to compute the energy spectrum

$$E(k) = \frac{C}{k^2}\int_0^{T_c} S(T)^{1/2}\hat{\omega}^{2D}[S(T)^{-1/2}k, T]dT \tag{4.4}$$

where $C = 2\pi^2 l_0 N_c/L^3$ is a constant. The function $\hat{\omega}^{2D}$ denotes the enstrophy spectrum of the unstrained 2-D flow and is defined by

$$\hat{\omega}^{2D}(k,t) = k\int_0^{2\pi} \left|\bar{\omega}^{2D}(k\cos\theta_k, k\sin\theta_k, t)\right|^2 d\theta_k \tag{4.5}$$

where $\bar{\omega}^{2D}$ represents enstrophy in a cylindrical shell in 2-D wavenumber space per unit width of the shell.

$$\bar{\omega}^{2D} = \frac{1}{(2\pi)^2}\int\int \exp[-i(k_x x + k_y y)]\omega^{2D}(x,y,t)\ dxdy \tag{4.6}$$

For a constant strain rate $a(t) = a$, the stretching function $S = e^{at}$ and $T = (e^{at}-1)/a$ and hence, $S = 1 + aT$ is a possible stretching function. The time integration represents the effect of stretching and the finite-time cutoff is to prevent indefinite stretching and also signifies possible coalescence with a different vortex to renew the spiral structure. The derivation of expression in (4.4) involves a number of steps which may be briefly listed as follows: The energy spectrum is computed for turbulence in a cubic domain of side length L. The 3-D enstrophy spectrum may be obtained by integrating the Fourier integral of the vorticity correlation function over a spherical surface in wavenumber space. Vorticity is assumed to be concentrated in isolated tubes and the integral is

carried out by summation of 2D cross-section integrals in different tube segments of initial length l_0. Turbulence is assumed to be stationary such that the vortex segments of same strength and structure are created a rate N_c and are distinguishable only by age. This ergodic hypothesis permits summation over all the tube segments to be converted into time integral over the life-time of a vortex segment.

$$\sum_i (\ ) = N_c \int_0^{t_c} (\ ) dt \tag{4.7}$$

Assumption of homogeneous turbulence allows the energy spectrum to be computed from the enstrophy spectrum. The derivation does not require isotropy. We focus on the two-dimensional structure of the spiral. The analytical spiral vortex solution developed by Lundgren [73] is employed, the details of which are described. The solution is of the form of Fourier series in θ cylindrical coordinate.

$$\omega(r,\theta,t) = \sum_{n=-\infty}^{\infty} \omega_n(r,t) e^{in\theta} \tag{4.8a}$$

$$\omega_n(r,t) = f_n(r) \exp\left[-in\Omega(r)t - \frac{1}{3}n^2\Omega'^2\nu t^3\right] \tag{4.8b}$$

where f_n is an arbitrary function. The angular velocity $\Omega(r)$ and the average vorticity ω_0 satisfy the relation

$$r\omega_0 = \frac{d}{dr} r^2 \Omega(r) \tag{4.9}$$

For differential rotation, the function $\Omega(r)$ is monotonically decreasing. The asymptotic result, which involves solving Bessel function integrals by the method of stationary phase is given by Equation 4.10.

$$\hat{\omega}^{2D} = t^{-1} G(k/t) e^{-2\nu k^2 t/3}, \ \ G(k/t) = \frac{1}{\pi} \sum_{n=1}^{\infty} \frac{r_n}{n\Omega''(r_n)} |f_n(r_n)|^2, \ \ n\Omega'(r_n) = -k/t \tag{4.10}$$

$$E(k) \sim A k^{-5/3} \exp(-2\nu k^2/3a), \quad S \simeq aT \tag{4.11}$$

This results in the $k^{-5/3}$ Kolmogorov spectrum, shown in (4.11). Lundgren [74] explains that this spectrum is obtained because of the inviscid enstrophy preservation similarity form as shown in (4.12). Tightening spiral turns result in a self-preserving

temporal enstrophy cascade to higher wavenumbers.

$$\int_0^\infty \frac{G(k/t)}{t} \equiv \text{const} \tag{4.12}$$

The initial spiral velocity field for the variable density calculations is taken from Lundgren [74] and is of the form that corresponds to the analytical two-dimensional vorticity solution stated above. It consists of a central core with two-halo spirals. The functional form is expressed in the equations below.

$$\omega^{2D}(r,\theta,t) = C\exp(-\bar{r}^2)(2+\bar{r}^2\sum_{n=0}^{\infty}\cos(2n[\theta-\Omega t])\exp(-4n^2\Omega'^2\nu t^3/3)) \tag{4.13a}$$

$$\Omega = \frac{3}{8\bar{r}^2}C[1-(1+\bar{r}^2/3)\exp(-\bar{r}^2)] \tag{4.13b}$$

Here $C = \Gamma/3\pi r_0^2$; $\Gamma = 25000\nu$ is the circulation; $\bar{r} = r/r_0$ and r_0 is the radius of the central core. The initial velocity field is divergence free and corresponds to non-dimensionalized time $t = 50$. It is important to mention here that all the details above follow the work of Lundgren [73, 74] and Gomez et al. [45].

4.2 Variable-density effects on the model spectrum

We analyze the low Mach number variable density effects on the spectrum of the stretched-spiral vortex. Variable density flows have an important additional source of vorticity, namely the baroclinic torque. The torque results from misaligned pressure gradient and density gradient vectors (Equation 4.14).

$$\frac{\partial\vec{\omega}}{\partial t} + \nabla\times(\vec{\omega}\times\vec{v}) = \frac{1}{\rho^2}\nabla\rho\times\nabla p + \nabla\times\left(\frac{\nabla.\sigma}{\rho}\right) + \nabla\times\vec{F}^b \tag{4.14}$$

where σ is the viscous stress tensor and $\vec{F_b}$ is a non-conservative body force. During the life-time of the stretched-spiral vortex, the enstrophy contribution due to baroclinic torque changes the 3-D energy spectrum. We investigate these changes in the 3D spectra and their dependence on the strength of the resolved-scale density gradients. The initial density field is an isotropic field of unmixed fluids of densities ρ_1 and ρ_2 where the density differences are thermal. The initial pressure field is obtained by solving the

incompressible Poisson equation. The mean pressure corresponds to a Mach number of 0.1 based on u_{rms} We simulate two sets of different initial density fields with mean density $\bar{\rho} = 1.0\text{kg/m}^3$. Each set has fields corresponding to $A = (\rho_2 - \rho_1)/(\rho_2 + \rho_1) = 0.125, 0.250, 0.375, 0.500$. The difference between the two sets is the thickness of the interface between the fluids of different densities. Figure 4.4 illustrates this.

It must be noted that together all the simulations fall back on varying a single parameter of interest $\overline{|\nabla\rho|}$. Figure 4.2 shows the time-evolution of vorticity contours for the two-dimensional isentropic ($A = 0$) and the variable-density spiral vortex($A = 0.25$). Production of vorticity due to baroclinic torque and intensification of density gradients in the spirals are clearly visualized. The results of the variable-density study are presented in Figure 4.3. We observe that the energy content in the $k^{-5/3}$ range (the horizontal part of the line plots extending from approximately $kr_0 = 55$ to $kr_0 = 75$) increases with $\overline{|\nabla\rho|}$ of the initial density field. However, the $k^{-5/3}$ exponent of the range does not change. For all the computations, the time integration in (4.4) is carried out till $t = 120r_0^2/\Gamma$ for which $k^{-5/3}$ range converges within a small margin. The 3D energy spectrum is averaged over strain rate values ranging from $a = 0.8\Gamma/r_0^2$ to $a = 1.2\Gamma/r_0^2$ to regularize the spectrum. The grid sizes employed for computations differ from case to case and range from 512^2 to 2048^2 depending on the mean initial density gradient magnitude of the case. Higher $\overline{|\nabla\rho|}$ requires larger grid size. The sensitivity of the 3D spectrum to the grid and spatial distribution of the initial density field is demonstrated in Figure 4.4. The spatial distribution of the initial density field is a random parameter, although ρ_1, ρ_2 and the interface width may be fixed. It may be observed that the variance in the 3D energy spectrum due to randomness in the initial density field is small as compared to the change in the spectrum due to variable-density effects.

The factor of increase in 3D energy spectrum pre-factor in the $k^{-5/3}$ range relative to the isentropic (near constant density case) is denoted by $\mathcal{V}$ and plotted with the mean non-dimensionalized density gradient magnitude in Figure 4.5. A curve is fit through the data points obtained in the simulations. The curve can be forced to plateau where the identity of the spiral vortex core changes. This corresponds to extremely strong density gradients (high A with sharp interfaces). As seen in Figure 4.3, these cases alter the energy-containing wavenumber region as well, changing the definition of vortex core. However, local resolved-scale density gradients in LES calculations are not expected to

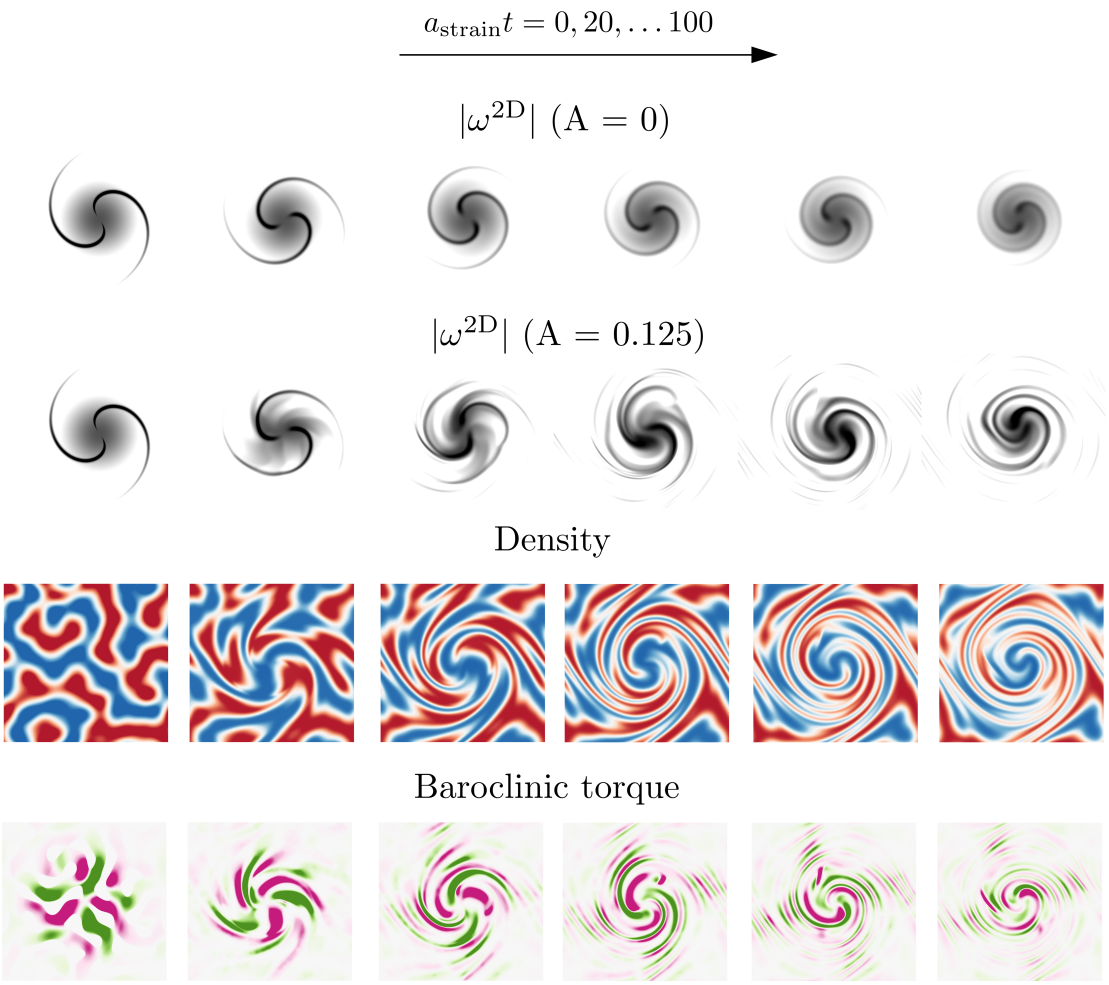

Figure 4.2: Time evolution of the variable-density stretched-spiral vortex core in strained time.

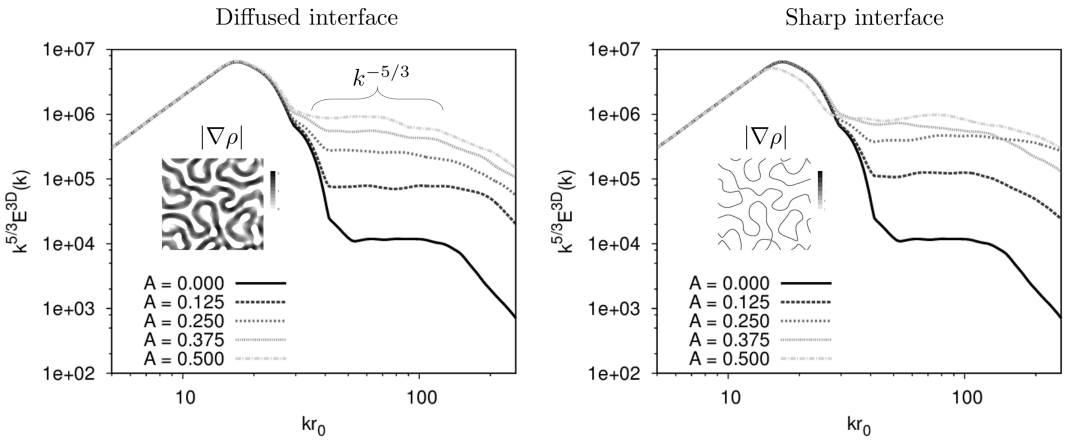

Figure 4.3: 3D specific energy spectrum computed from the model vorticity field.

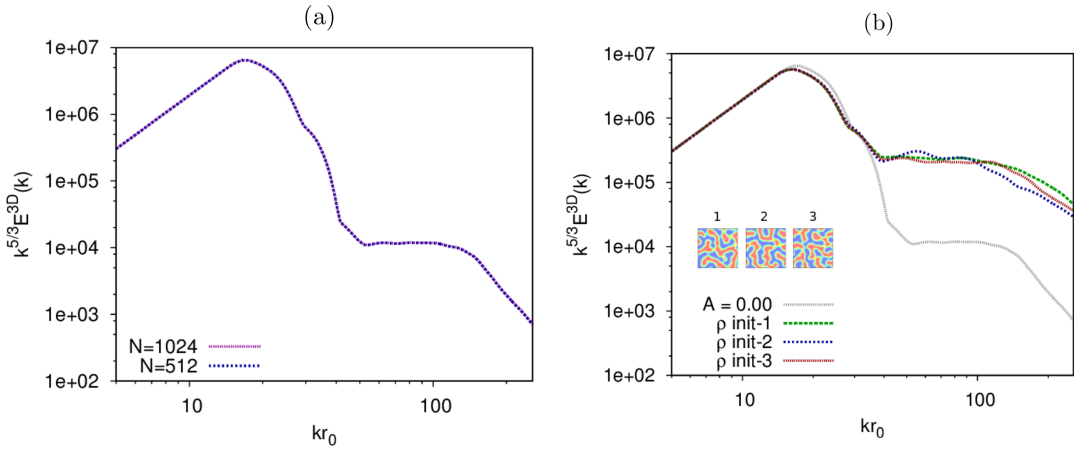

Figure 4.4: Sensitivity of the 3D specific energy spectrum to grid resolution and initial density field.

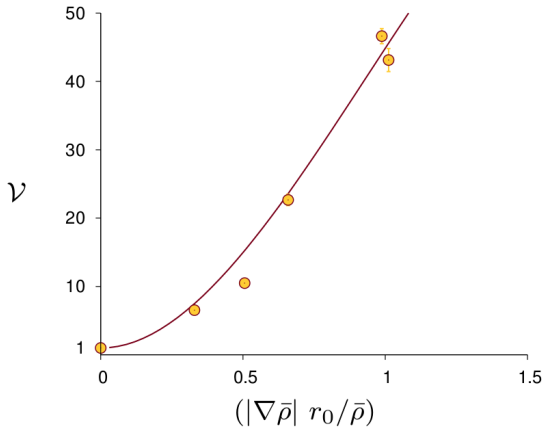

Figure 4.5: Factor of increase in the spectrum prefactor in the -5/3 subrange.

be as strong when non-dimensionalized with the subgrid vortex length scale.

4.2.1 Discussion

The presence of spatial density variations in Lundgren's physical-space model for turbulent cascade predicts increased enstrophy at small-scales. Vorticity production by baroclinic torque changes the self-similar nature of the temporal cascade as it does not obey the inviscid enstrophy preservation in the original constant-density version of the model. Variable-density effects therefore predict an increased transfer of enstrophy to small-scales, which accounts for the additional vorticity produced at each scale. Qualitatively, this picture is consistent with the variable-density K-H-M equation derived earlier in the thesis, where in addition to the interscale flux, dilatation and density gradient difference terms contribute to the rate of specific energy dissipation at each scale.

In the present work, the initial mass density distribution in the vortex plane is random but isotropic. Although any axial variation of the density field in the vortex tubes is not considered, the space-averaged enstrophy may still assume that the vortices are primarily distinguishable by age. Even if the vorticity field varies along a tube due to different initial density distribution, the plane integrated enstrophy is not sensitive to the initial distribution but only the effective density gradient magnitude. Therefore the increase in energy in the -5/3 subrange of the model spectrum due to density variations

can be treated as a physical effect and used to inform subgrid-scale modeling.

The stretched-vortex SGS model [79, 119] is related to Lundgren's physical space description for turbulent fine structure. The key ingredient in the physical-space version of the model is the estimation of the Kolmogorov pre-factor associated with the -5/3 spectrum. The model estimates it using structure function matching with the filtered velocity field. In the presence of filtered density variations, proposing an increase in the Kolmogorov pre-factor from the present results is not possible because the pre-factor is determined solely by the large-scale velocity field. However, an assumption in the model that may fail in the presence of baroclinic vorticity is the balance between production of energy in SGS scales via non-linear cascade and viscous dissipation of energy in the SGS scales. In the steady state equation for specific SGS kinetic energy, terms such as SGS mass flux, pressure acceleration and velocity dilatation will also contribute. An assessment of their contribution must be made via carefully designed numerical experiments of variable-density compressible turbulence.

Lastly, we must also admit that Lundgren's model for turbulent fine structure is only one possible description of turbulent cascade in the physical space. There also exist alternate descriptions, such as the gamma helical vortex tube model in Childress [21]. Therefore, any quantitative modeling of inertial range vorticity dynamics in the presence of baroclinic torque will be restricted to its set of assumptions.

Chapter 5

Direct numerical simulations : *a priori* analysis

In this chapter, we explicitly filter fields from variable-density turbulent flows and analyze the subgrid scale terms obtained within Favre- and Reynolds-filtered frameworks presented in Chapter 2. Two flows are considered: isotropic decaying turbulence with mixing of thermally inhomogeneous gases, and reshocked heavy gas mixing layer. The second case involves interaction of a shock with a Richtmyer-Meshkov unstable heavy gas layer that is shocked previously and is in its non-linear growth stage. The problem is anisotropic. Both flows involve baroclinic torque generated vorticity that affects the turbulent cascade during the transient state. Both flows involve turbulent mixing and eventual decay. While the dynamics in the first case is imposed via initial conditions, the shock-deposited vorticity dominates the second case. The goal of the study is to evaluate the subgrid-scale effects associated with inertia and compressibility on large-scale velocity. Subgrid terms that appear in the governing equations for both, density-weighted and unweighted large scale velocity are computed and analyzed.

Table 5.1: Primary flow-cases simulated for subgrid-scale analysis.

	Initial condition	Atwood number
Case 1	IC1 (homentropic ρ fluctuations)	-
Case 2a	IC2 (isotropic double-δ ρ pdf)	0.4
Case 2b	IC2 (isotropic double-δ ρ pdf)	0.7

5.1 Isotropic variable density decaying turbulence

5.1.1 Simulation setup and validation

We solve the compressible Navier-Stokes equations on a triperiodic domain with initialization for the variables ρ, u_i, p. The ideal gas law $p = \rho RT$ is used to compute the temperature field. Transport properties such as viscosity are taken to be constant, to avoid the influence of variable-density fluctuations on viscous transport processes. A triperiodic grid with 512 points along each co-ordinate direction is used for the simulations. Three cases are considered (Table 5.1) with turbulent Mach number M_t of 0.3, which is chosen as representative of high-speed turbulent boundary layers [63]. The initial velocity field is identical for the cases, and is initialized by extracting the solenoidal velocity component from a precursor simulation of compressible decaying turbulence simulation whose velocity derivative skewness has saturated to a value close to 0.5. Saturation in skewness implies that the rate of vorticity production via vortex stretching has stabilized and the flow has evolved from an artificial state into a turbulent state with realistic non-linear dynamics. The precursor simulation therefore ensures that the flows initialized in this study are closer to a realistic turbulent flow compared to a random isotropic velocity field. The precursor simulation is initialized with a $k^2 \exp(-2(k/k_0)^2)$ radial spectrum with $Re_\lambda = 100, M_t = 0.3, k_0/L = 6$ and simulated till $t/t_{\text{eddy}} = 3.0$.

Initial density, pressure, and temperature fields are initialized in two different ways denoted by IC1 and IC2. In IC1, the initial pressure field is obtained from the incompressible Poisson equation using the volume-averaged density. The density field is then initialized with $p/\rho^\gamma = \langle p \rangle / \langle \rho \rangle^\gamma$ ([95, 90]). Note that only the solenoidal velocity field from the precursor simulation is used for initialization. This is because with IC1 thermodynamic fields, the time evolution of mean dilatation variance with zero initial

dilatation is near-identical to that from a non-zero initial dilatation obtained from small parameter expansion about M_t ([90]). The two curves are found to nearly overlap for $t/t_{\text{eddy}} > 0.3$. A comparison of the turbulent kinetic energy decay in compressible turbulence using IC1 to results from Samtaney et al. [95] is provided below.

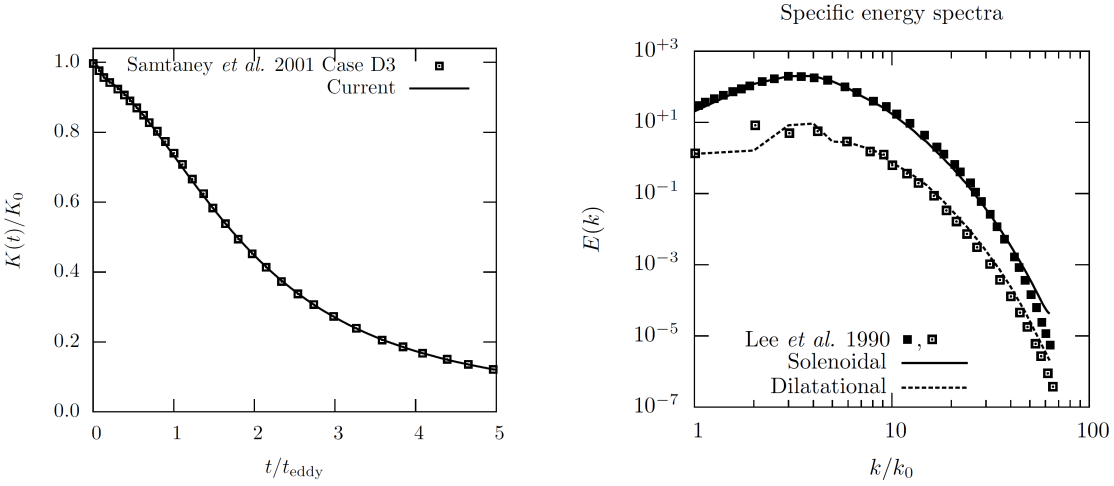

Figure 5.1: Comparison of decaying isotropic compressible turbulence simulations with literature.

IC2 corresponds to an isotropic double-δ distribution of the density field with the volume divided into two regions of densities ρ_1 and ρ_2, with a smooth interface. Similar scalar fields have been used previously in the work of Livescu and Ristorcelli [72] and Sandoval [97]. The scalar field is generated with non-zero spectral content for $2 \leq kL \leq 4$, where L is the length of the periodic domain. To generate a smooth interface, the field is filtered with an exponential filter with $k_c L = 4$, resulting in ρ pdf to deviate slightly from a strict double-δ distribution. Smoothing the ρ interface changes the mean and variance of the density distribution from 1.0 and 0.25 to 1.017 and 0.235 respectively. The Atwood number $A = (\rho_2 + \rho_1)/(\rho_2 - \rho_1)$ is an important parameter in quantifying the strength of hydrodynamic instability in stratified flows; a volumetric mean density $\langle\rho\rangle = 1.0$ is used to calculate ρ_1 and ρ_2. Cases 2a and 2b use IC2, but differ in the Atwood number. Case 2b has a larger Atwood number than Case 2a, and as expected, exhibits more pronounced variable-density effects. The largest value of Atwood number considered here corresponds to a density ratio of approximately 6, which is a typical of light/heavy fluid mixing in industrial applications. Larger density ratios exist in

combustion and multiphase systems, and are expected to produce stronger variable-density effects. The pressure in IC2 is determined by solving the inviscid variable-density Poisson equation. This equation is obtained by ensuring that the initial conditions do not provide a source of Lagrangian change in fluid density, $\mathrm{D}(\partial_j u_j)/\mathrm{D}t = 0$. The pressure at time $t = 0$ therefore satisfies

$$\frac{\partial}{\partial x_i}\left(\frac{1}{\rho}\frac{\partial p}{\partial x_i}\right) = -\frac{\partial u_j}{\partial x_i}\frac{\partial u_i}{\partial x_j} \tag{5.1}$$

We restrict the initial u_i, ρ fields to large length scales. The velocity field from the precursor simulation and the generated density field are filtered using a sharp-spectral filter with $k_c L = 32$. This ensures that the small scales in the density and velocity fields develop from the initial conditions together via vortex stretching and baroclinic torque. The viscosity is determined such that the initial Taylor length scale Reynolds number Re_λ is 500. Re_λ is large because the initial velocity spectrum is non-zero at low wavenumbers $kL < 32$, resulting in a large initial Taylor length scale λ. After the transient, the energy spectrum becomes broadband and Re_λ decreases. At $t/t_{\mathrm{eddy}} = 3$, the Taylor length scale Reynolds number reduces to $Re_\lambda = 85$. The fields corresponding to the initial conditions are visualized in figure 5.2.

The convective flux is evaluated using a stable low-dissipation scheme based on the kinetic-energy consistent method developed by [109]. A gradient reconstruction method described in [110] is used to make the symmetric part of the convective flux formally sixth-order accurate. In the regions of strong compression (shocklets), a Ducros-type shock sensor adds dissipation to the convective flux using the non-symmetric part of modified Steger-Warming flux-vector splitting scheme. The details of the flux scheme can be found in [13]. The viscous fluxes are computed using a second-order central scheme and use compact stencil second-order least-squares gradients. The low-storage third-order accurate strong-stability preserving Runge-Kutta scheme [46] is used for time integration. A CFL number of 0.7 based on the local fast characteristic wave speed is used.

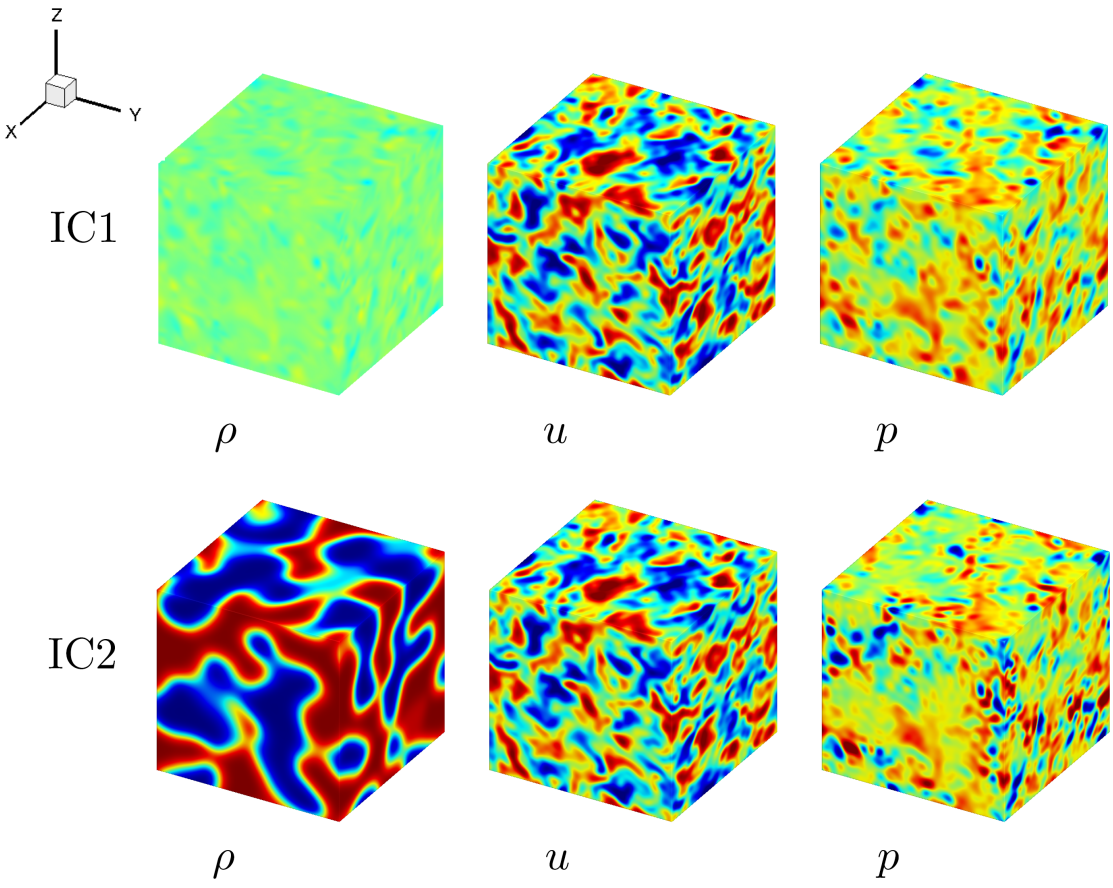

Figure 5.2: DNS initialization: ρ, u, p fields are shown.

5.1.2 Time histories and spatial statistics

Volume-averaged statistics from the three cases simulated are shown in figure 5.3. Time histories of six physical quantities are plotted: (a) kinetic energy, (b) enstrophy, (c) dilatation variance, (d) mass flux variance, (e) density variance, and (f) baroclinic torque variance. The volume averages of dilatation, mass flux and baroclinic torque are numerically close to zero, and hence, variances of these quantities are plotted. All the curves are normalized by the value corresponding to Case 2b at time $t = 0$. While the volume-averaged kinetic energy curves nearly overlap, quantities based on velocity gradients, namely the enstrophy and dilatation variance, exhibit prominent differences during $1 \leq t/t_{\text{eddy}} \leq 4$. This occurs when small velocity scales are produced by vortex stretching and variable-density mixing effects are active. Later, when mixing homogenizes the density field, the curves of kinetic energy, enstrophy and dilatation variance for Cases 2a and 2b begin to converge with the Case 1 curves.

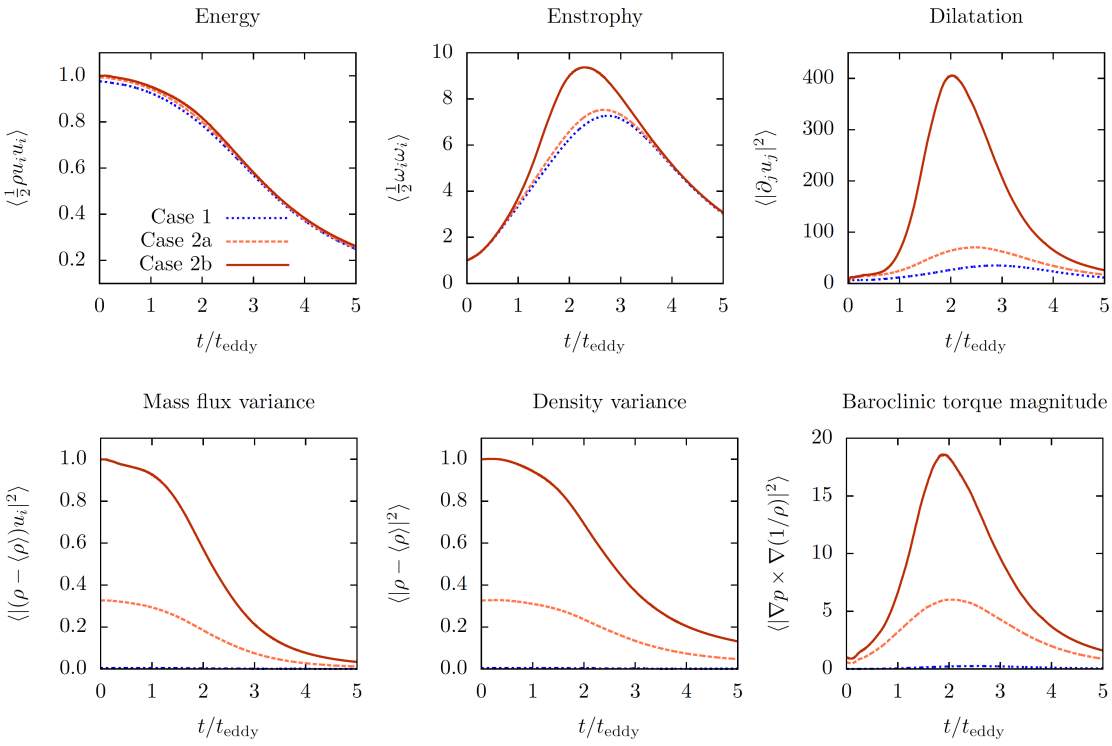

Figure 5.3: Time history of volume averaged quantities.

Velocity-gradient-based statistics are found to be more strongly affected by variable-density effects. In the case of enstrophy, the differences can be attributed to production of vorticity by baroclinic torque, which is the curl of the pressure-gradient acceleration. Baroclinic-torque-generated vorticity is further stretched by the background strain, thus compounding the enstrophy generation process. We also note that the differences in the curves are discernible only after one eddy turnover time, indicating the absence of impulsively-generated enstrophy by the initial conditions. The increase in dilatation variance (figure 5.3c) in Cases 2a and 2b can be explained by the pressure-gradient acceleration. The pressure-gradient acceleration tensor $\mathcal{A}_{ij} = \partial_j(\partial_i p/\rho)$ appears in the velocity gradient transport equation. The antisymmetric part $\mathcal{A}_{ij} - \mathcal{A}_{ji}$ is associated with baroclinic torque and the corresponding term in the dilatation rate equation is the trace of the tensor $\mathcal{A}_{ii}$. The symmetric part $\mathcal{A}_{ij} + \mathcal{A}_{ji}$ contributes to the rate of change of the strain rate tensor. The fluctuating mass flux variance and the density fluctuation variance decay monotonically, but have transience that lasts approximately two eddy turnover times, marked by inflection point in the curve. The fluctuating mass flux is also the mean fluctuating Favre-filtered velocity, and represents the spatial correlation of the density and the velocity fields. The initial density variance in Case 1 is seen to be extremely small relative to Cases 2a and 2b, and suggests that the variable-density effects in compressible decaying turbulence are expected to be small.

The kinetic energy radial spectra and the energy spectral density of the density field at $t/t_{\text{eddy}} = 3.0$ are plotted in figure 5.4.

The flow field at this time contains a small inertial subrange with a $k^{-5/3}$ slope present approximately between $0.2 \geq k\eta \geq 0.1$. The presence of initial thermal-density inhomogeneity increases the content in small scale velocity field, but the $k^{-5/3}$ spectrum is preserved. Increase in strength of density fluctuations leads to increased rate of kinetic energy transfer into higher wavenumbers. This is also reflected in the aliasing error that develops at high wavenumbers due to the use of a a low-dissipation central numerical scheme used in the direct simulation. The density field spectrum shows that the content in the large scales for Case 1 is relatively flat ($\sim k^0$), while Cases 2a and 2b, which involve mixing of variable-density fluids, exhibit a k^{-1} behavior at low wavenumbers. This may be interpreted as the Batchelor k^{-1} viscous-convective scaling in the high Schmidt number limit as the effective diffusivity for density is zero [28].

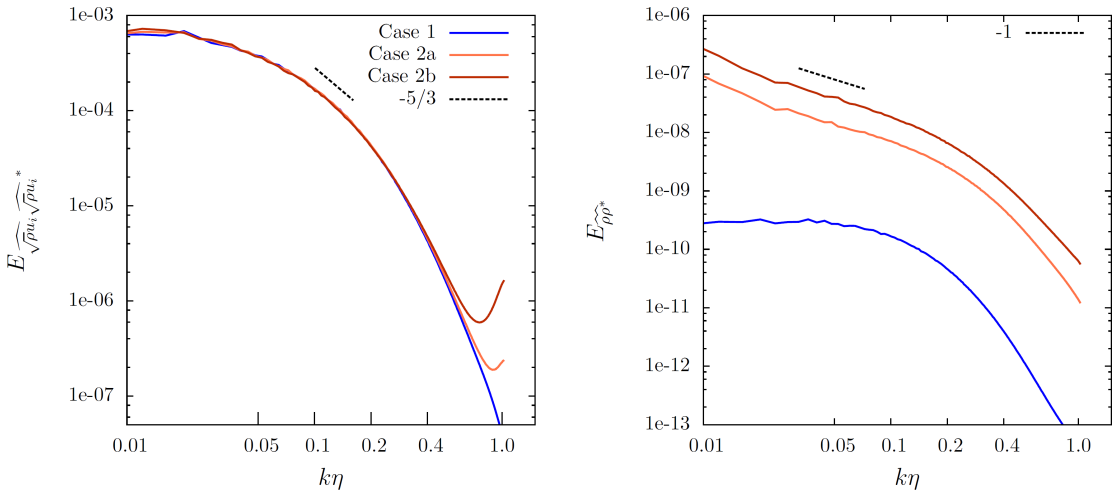

Figure 5.4: Three-dimensional shell-averaged radial spectra of kinetic energy (left) and energy spectral density of the density (right) at $t/t_{\mathrm{eddy}} = 3.0$.

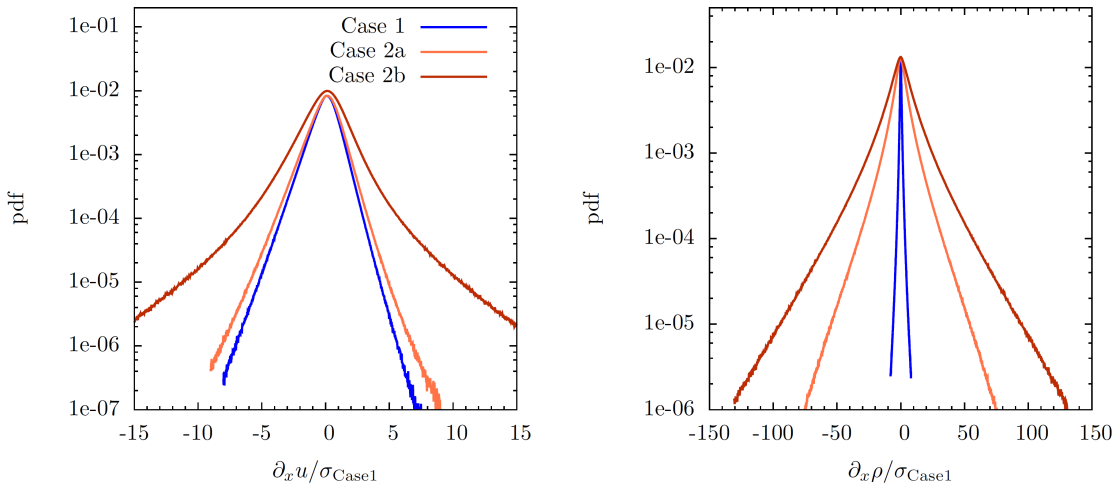

Figure 5.5: Probability distribution functions of x-gradients of x component of velocity (left) and the density (right) fields.

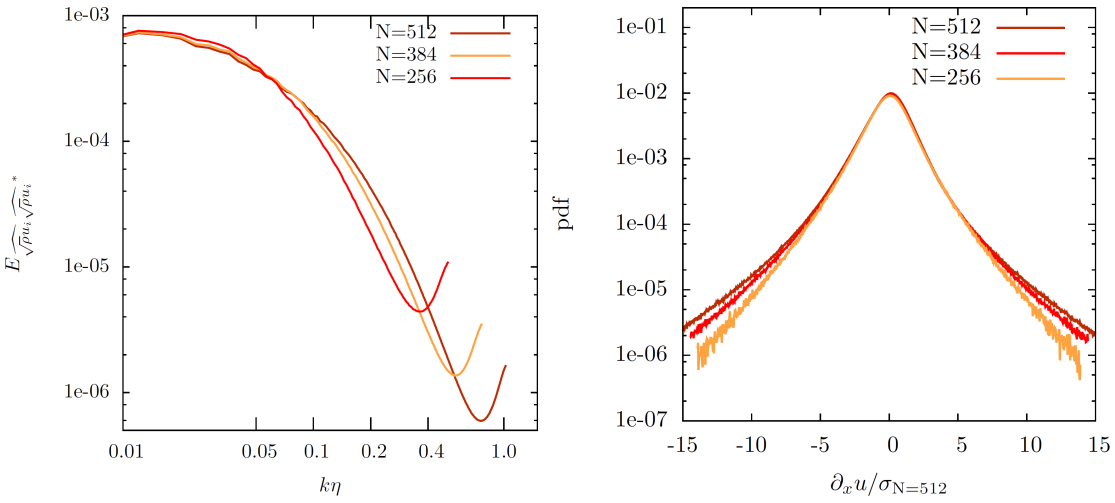

Figure 5.6: Grid refinement study of the field statistics at $t/t_{\mathrm{eddy}} = 3$ for Case 2b

Figure 5.5 shows the effect of variable-density mixing on the intermittency of the flow fields. Probability distribution functions of x-gradients of x component of the velocity and density are plotted. The mean values have been subtracted and the x-axis is scaled with the standard deviation for Case 1. Variable-density effects are seen to increase the probability of occurrence of the tail events and have distributions with larger standard deviation. The $\partial_x u$ and $\partial_x \rho$ pdfs show that all cases have a high degree of super-Gaussian (leptokurtic) character, indicating the presence of intermittency representative of high Re turbulence [99]. Figure 5.6 demonstrates the sensitivity of the statistical quantities to grid refinement.

5.1.3 Variable-density subgrid-scale analysis

In this section, we filter the DNS flow fields explicitly to study the SGS terms that appear in the Favre-filtered and Reynolds-filtered momentum equations. The first subsection compares the two resolved-scale velocity fields in Fourier and physical space. The second subsection compares the importance of the variable-density SGS terms with respect to the constant-density SGS terms. Central moments that involve ρ and $\nabla \cdot u$ as one of the variables under the filter operator are referred to as variable-density SGS terms. Terms that involve the SGS specific stress $\mathcal{T}[u_i, u_j] = \overline{u_i u_j} - \bar{u}_i \bar{u}_j$ are referred to as

constant-density SGS terms. This is the first study that computes the effect of the small-scale density variations on large-scale momentum in compressible turbulent mixing of variable-density fluids. We restrict the results to a budget analysis, and no *a priori* assessment of SGS closures is conducted. Similarly, as aforementioned, the effect of implicit filtering associated with an LES discretization is not discussed.

The time histories of dilatation and enstrophy suggest that the flows reach a state of decay after two eddy turnover times. Therefore, we carry out the variable-density SGS analysis of the instantaneous flow field at $t/t_{\text{eddy}} = 3.0$. The conclusions from the analysis are not sensitive to the time chosen in the decay regime. An exponential filter with $k_c\eta = 0.12$ is used to filter the fields, and all filtering operations are carried out in Fourier space. The value of 0.12 is chosen so that the cutoff wavenumber lies in the inertial subrange and approximately 82% of the kinetic energy is resolved. We find that the relative size of variable-density SGS terms reported in our study is not sensitive to the filter type and the choice of filter width.

5.1.4 Comparison of Reynolds-filtered and Favre-filtered velocity fields

The flow field corresponding to Case 2b with Atwood number of 0.7 is filtered to assess the differences between the $\tilde{u}_i$ and $\bar{u}_i$ velocity fields. The spectral content for both resolved-scale variables is found to be nearly identical for this case, with $\tilde{u}_i$ having slightly larger specific energy at wavenumbers beyond the filter cutoff (figure 5.7). This is true for the exponential and the sharp spectral filter. We also compare the filtered vorticity $\bar{\omega}_i$ and the curl of the Favre-filtered velocity $\nabla \times \tilde{u}_i$ in Fourier and physical space (figure 5.8 left). The curl of the Favre-filtered velocity $\omega_i^{\text{F}} = \nabla \times \tilde{u}_i$ is referred to as pseudo-vorticity in [15]. We also note that pseudo-vorticity ω_i^{F} is not the Favre-filtered vorticity $\tilde{\omega}_i$. The differences in the spectral content of the filtered vorticity and pseudo-vorticity are found to be similar to the differences in the spectral content of the velocity fields, except they are amplified because $E_{\widehat{\omega}_i\widehat{\omega}_i^*} \sim k^2 E_{\widehat{u}_i\widehat{u}_i{}^*}$

In physical space, the pdf of normalized difference between $\bar{u}_i$ and $\tilde{u}_i$ gradient fields is plotted. It is found that the difference between $\bar{\omega}_i$ and ω_i^{F} can exceed 100% in different regions of the flow. These is seen in figure 5.8 (right), where $|\bar{\omega}_i| - |\omega_i^{\text{F}}| > |\bar{\omega}_i|$ (area under the solid curve beyond horizontal-axis value of 1.0). The differences between the magnitude of $\bar{S}_{ij}$ and $S_{ij}^{\text{F}} = 1/2(\partial_i\tilde{u}_j + \partial_j\tilde{u}_i)$ can also be large, but are relatively less

pronounced than in the case of vorticity variables. In summary, the spectral content of the Favre-filtered and the Reynolds-filtered velocity fields in Case 2b do not exhibit strong disparities in the decay stage. However, differences in the resolved-scale velocity gradient fields in physical space are non-negligible.

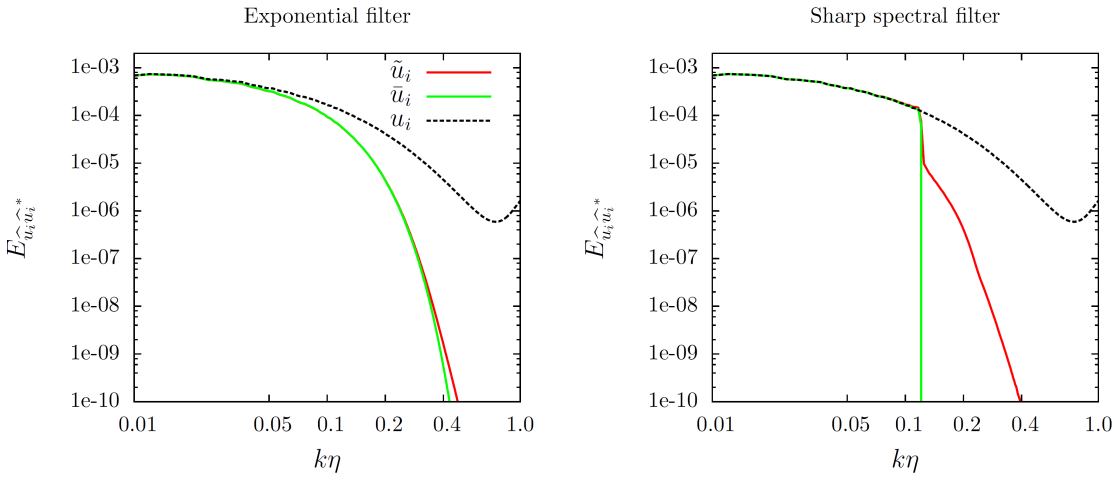

Figure 5.7: Resolved-scale velocity radial spectra from Case 2b filtered with $k_c\eta = 0.12$ with different filters: Favre-filtered velocity $\tilde{u}_i$ and filtered velocity $\bar{u}_i$ are compared.

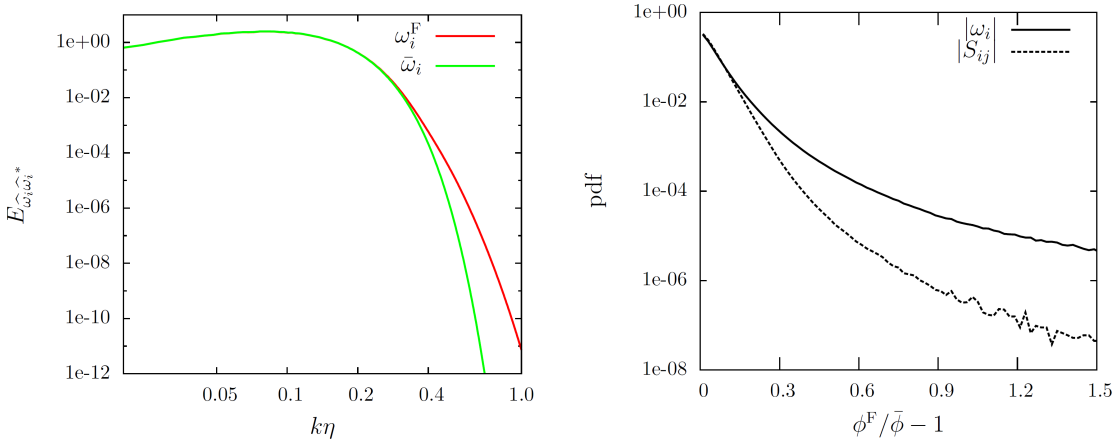

Figure 5.8: Comparison of filtered vorticity $\bar{\omega}_i$ and the curl of Favre-filtered velocity ($\omega_i^{\mathrm{F}} = \nabla\times\tilde{u}_i \neq \tilde{\omega}_i$) (left) and the relative difference between $\bar{u}_i$ and $\tilde{u}_i$ gradient quantities in physical space (right).

5.1.5 Variable-density SGS terms in resolved-scale momentum equation

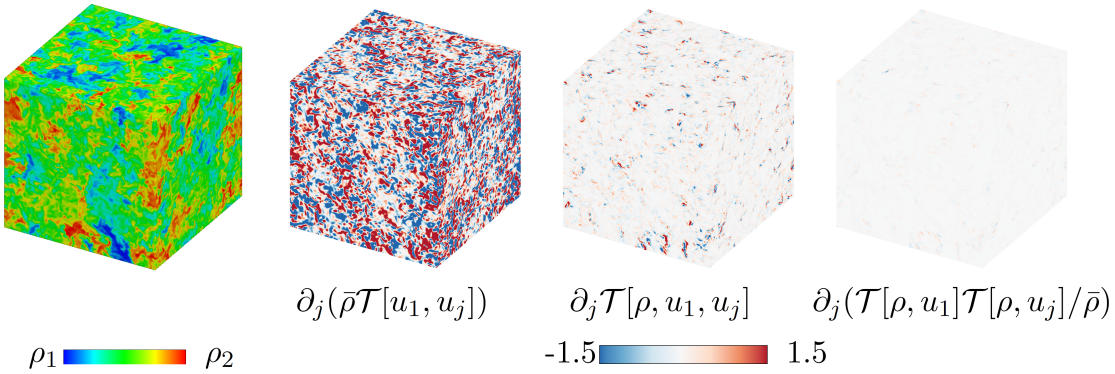

Figure 5.9: Case 2b: instantaneous density field at $t/t_{\text{eddy}} = 3$ (left), and snapshots of fields corresponding to the SGS terms in $\partial_t\bar{\rho}\tilde{u}_1$ equation (right). The SGS terms are non-dimensionalized by $|\langle\epsilon\rangle|/\sqrt{\langle u_i u_i/2\rangle}$.

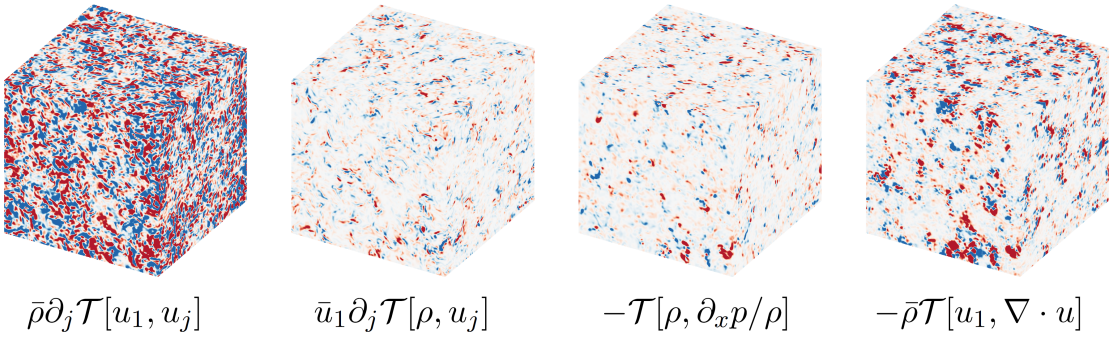

Figure 5.10: Case 2b: snapshots of fields corresponding to SGS terms in $\partial_t\bar{\rho}\bar{u}_1$ equation at $t/t_{\text{eddy}} = 3$. Legend is same as figure 5.9.

Subgrid-scale terms in the resolved-scale momentum equation are computed using the DNS fields at $t/t_{\text{eddy}} = 3.0$ with an exponential filter of $k_c\eta = 0.12$. The SGS terms involving density ρ and dilatation $\nabla \cdot u$ in the central moments are of primary interest. The SGS specific stress $\mathcal{T}[u_i, u_j]$ serves as the reference for comparison. The analysis is unique because the terms appearing in the resolved-scale momentum equation are considered, as opposed to terms appearing in the transport equations of SGS kinetic energy, SGS stress, or other second-moment SGS terms. The resolved-scale momentum

equations corresponding to both the variables, $\partial_t \bar{\rho}\tilde{u}_i$ and $\partial_t \bar{\rho}\bar{u}_i$ are considered; each equation has its own set of SGS terms.

$$\frac{\partial \bar{\rho}\tilde{u}_i}{\partial t} + \frac{\partial}{\partial x_j}\Big(\bar{\rho}\tilde{u}_i\tilde{u}_i + \bar{p}\delta_{ij} + \bar{\rho}\mathcal{T}\left[u_i, u_j\right] + \mathcal{T}\left[\rho, u_i, u_j\right] - \mathcal{T}\left[\rho, u_i\right]\mathcal{T}\left[\rho, u_j\right]/\bar{\rho}\Big) = \bar{\sigma}_{\rho u_i} \quad (5.2)$$

$$\frac{\partial \bar{\rho}\bar{u}_i}{\partial t} + \frac{\partial}{\partial x_j}\Big(\bar{\rho}\bar{u}_i\bar{u}_i + \bar{p}\delta_{ij}\Big) + \bar{u}_i\frac{\partial \mathcal{T}\left[\rho, u_j\right]}{\partial x_j} + \bar{\rho}\frac{\partial \mathcal{T}\left[u_i, u_j\right]}{\partial x_j} - \bar{\rho}\mathcal{T}\left[u_i, \frac{\partial u_j}{\partial x_j}\right] - \mathcal{T}\left[\rho, \frac{1}{\rho}\frac{\partial p}{\partial x_i}\right] = \bar{\sigma}_{\rho u_i} \quad (5.3)$$

The SGS terms arising from viscous transport, including $\mathcal{T}\left[\rho, \sigma_{\rho u_i}/\rho\right]$ are not considered in this analysis. Snapshots of the x-component of the Case 2b SGS vector field are shown in figures 5.9 and 5.10 for the $\partial_t \bar{\rho}\tilde{u}_i$ and $\partial_t \bar{\rho}\bar{u}_i$ equations, respectively. All SGS terms are plotted on the same scale and colormap. We see that the specific stress $\mathcal{T}\left[u_i, u_j\right]$ terms in both equations are large and space-filling. While the variable-density SGS terms in both forms of the momentum equations are sparsely active, they can be large in specific regions. In particular, we note that the SGS mass flux term in the $\partial_t \bar{\rho}\tilde{u}_i$ equation is extremely small and that SGS velocity-dilatation term is the most active variable-density SGS term in the $\partial_t \bar{\rho}\bar{u}_i$ equation.

The relative importance of the variable-density SGS terms is evaluated by normalizing by the local constant-density term. The resulting ratio fields quantify the importance of the variable-density SGS terms. Since the SGS terms are vectors, the ratio of scalar projections are evaluated; two scalars are considered for this purpose. The first scalar is the magnitude of the SGS vector. If we denote a particular variable-density SGS term by T_i, and the constant-density term by T_i^{cd}, the quantity $|T_i|/|T_i^{\mathrm{cd}}|$ indicates the relative magnitude. However, there are regions in the flow where $|T_i^{\mathrm{cd}}|$ can approach zero, which corrupts the statistics. To avoid this issue, we evaluate the regularized ratio $|T_i|/(|T_i^{\mathrm{cd}}| + |V_i|)$, where $V_i = \bar{\sigma}_{\rho u_i}$ is the resolved-scale viscous diffusion vector and represents a physical and dimensional regularization. Thus, $|V_i|$ ensures that the statistical information derived from the ratio field, particularly the pdf tail is not arbitrary. In comparison to the SGS terms T_i, the $|V_i|$ values are typically very small. However, the V_i field is space-filling and non-zero due to the presence of non-zero strain-rate in the entire domain. In the limit when $k_c\eta >> 1$ and the SGS terms are zero ($T_i, T_i^{\mathrm{cd}} \to 0$), then $V_i \to \sigma_{\rho u_i}$ where $\sigma_{\rho u_i}$ is the viscous term in the momentum equation. Note that

the SGS vectors require derivatives. Like the filters, we compute these derivatives in Fourier space.

Besides the magnitude of these terms, a scalar incorporating the orientation of the SGS vectors is also required. In this context, projection on the resolved-scale velocity vector is considered. This is a physically meaningful projection and quantifies the contribution of SGS terms to the kinetic energy associated with the resolved-scale velocity. The rate of change of the kinetic energy is

$$\frac{\partial \frac{1}{2}\bar{\rho}\tilde{u}_i\tilde{u}_i}{\partial t} = \tilde{u}_i\frac{\partial \bar{\rho}\tilde{u}_i}{\partial t} - \frac{1}{2}\tilde{u}_i\tilde{u}_i\frac{\partial \bar{\rho}}{\partial t}, \qquad \frac{\partial \frac{1}{2}\bar{\rho}\bar{u}_i\bar{u}_i}{\partial t} = \bar{u}_i\frac{\partial \bar{\rho}\bar{u}_i}{\partial t} - \frac{1}{2}\bar{u}_i\bar{u}_i\frac{\partial \bar{\rho}}{\partial t} \tag{5.4}$$

We see that the projection of the resolved-scale momentum equation SGS terms on the resolved-scale velocities is their contribution to the computable kinetic energy. The term $\bar{u}_i\mathcal{S}_\rho$ appearing in $\partial_t\bar{\rho}\bar{u}_i$ is an exception; its contribution reverses sign due to the term $\partial_t\bar{\rho}$. Similar to the magnitude ratio, the ratio of the projection on resolved-scale velocity is computed with V_i to regularize the denominator. The ratio signifies the relative contribution to the resolved-scale kinetic energy.

By computing the ratio at each point in the instantaneous flow field, we can compute the the probability distribution functions for these fields. A typical ratio field and its pdf are shown in figure 5.11. These distributions are plotted for $\tilde{u}_i$ (figure 5.12) and $\bar{u}_i$ (figure 5.13). Plots on the left are the magnitude ratio distributions, and those on the right are the resolved-scale velocity projection ratios. Each plot has three curves with distributions from Cases 1, 2a and 2b. Let us consider figure 5.12. The plots in the top row correspond to the trivariate moment term $\partial_j\mathcal{T}\left[\rho, u_i, u_j\right]$ and those in the bottom row correspond to the SGS mass flux term $-\partial_j(\mathcal{T}\left[\rho, u_i\right]\mathcal{T}\left[\rho, u_j\right]/\bar{\rho})$.

Reynolds-filtered momentum equation $\partial_t\bar{\rho}\bar{u}_i$ pdfs are plotted in figure 5.13 for the SGS mass flux term $\bar{u}_i\partial_j\mathcal{T}\left[\rho, u_j\right]$ (top row), SGS pressure-gradient acceleration term $-\mathcal{T}\left[\rho, \partial_i p/\rho\right]$ (middle row), and SGS velocity-dilatation $\bar{\rho}\mathcal{T}\left[u_i, \partial_j u_j\right]$(bottom row). All three variable-density SGS terms are found to be non-negligible for Cases 2a and 2b, but insignificant for Case 1. For both resolved-scale momentum variables, the terms are found to be more important by means of velocity projection ratio metric.

Integral values for the ratios are also evaluated. Average ratio values are large for Case 2b and small for Case 1. For example, the value corresponding to trivariate term in

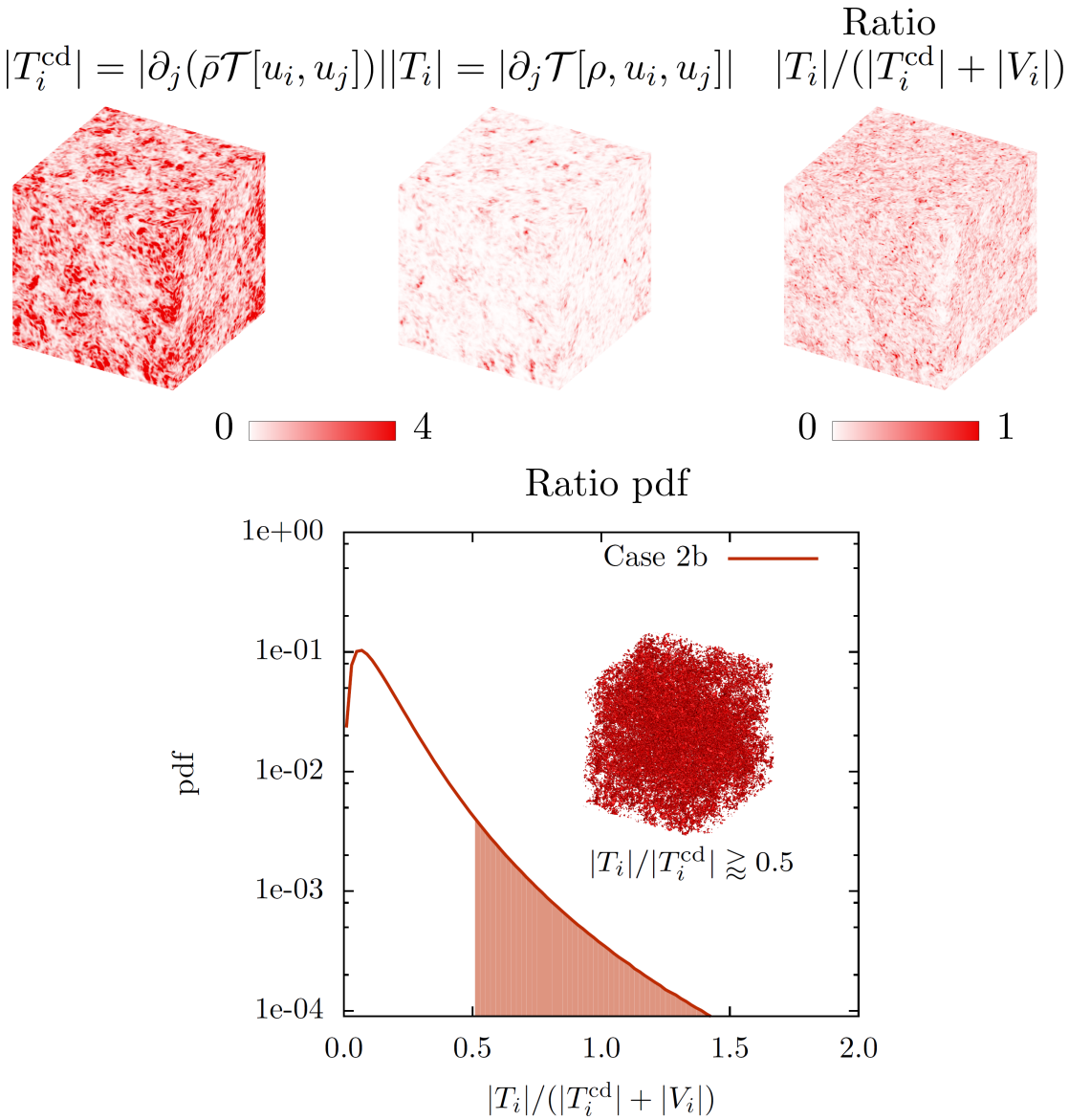

Figure 5.11: Case 2b: ratio pdf computed for trivariate moment magnitude in the $\partial_t\bar{\rho}\tilde{u}_i$ equation. The SGS terms are non-dimensionalized by $|\langle\epsilon\rangle|/\sqrt{\langle u_i u_i/2\rangle}$. Inset picture is an isosurface enclosing regions where ratio is greater than 0.5.

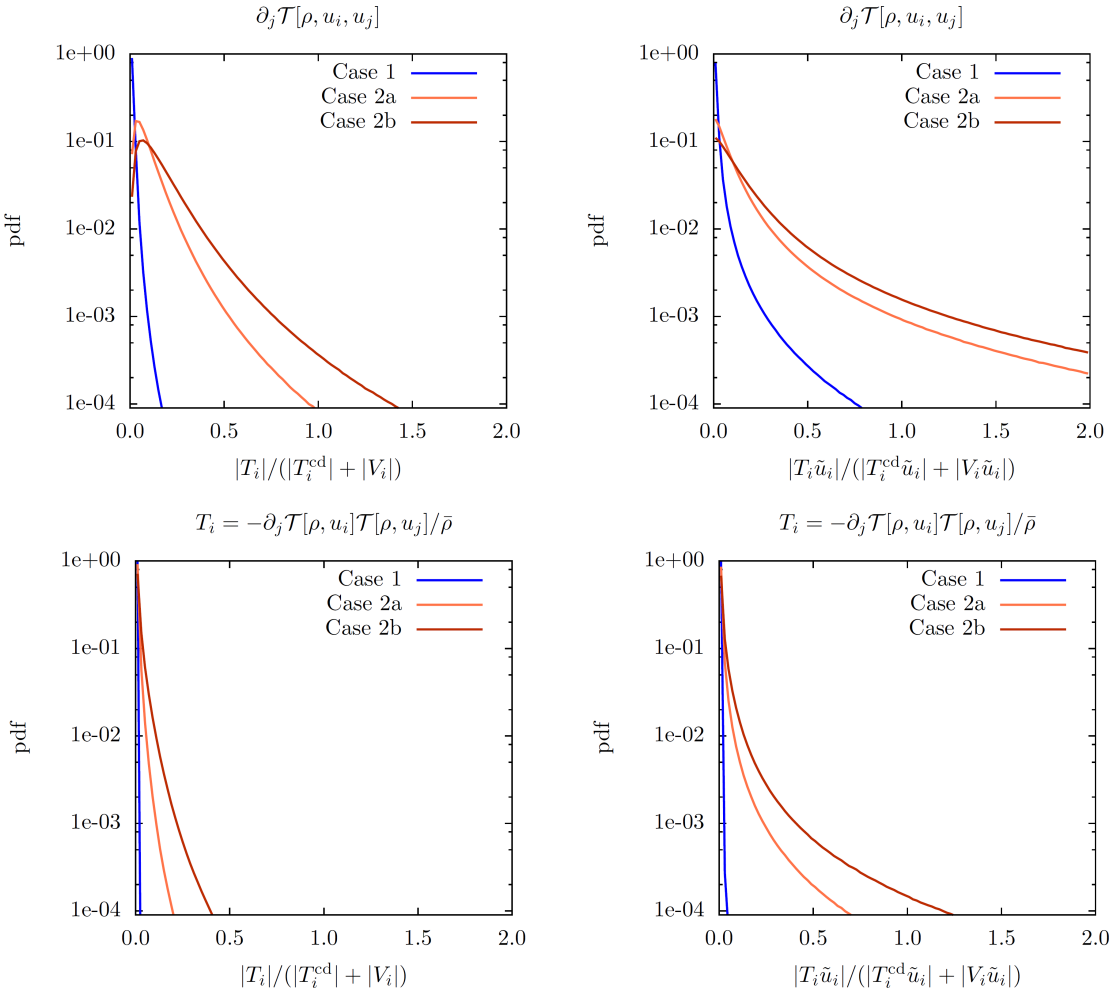

Figure 5.12: Probability distribution functions of the relative magnitude (left) and relative projection (right) for SGS terms in $\partial_t \bar{\rho}\tilde{u}_i$ equation from instantaneous flow field.

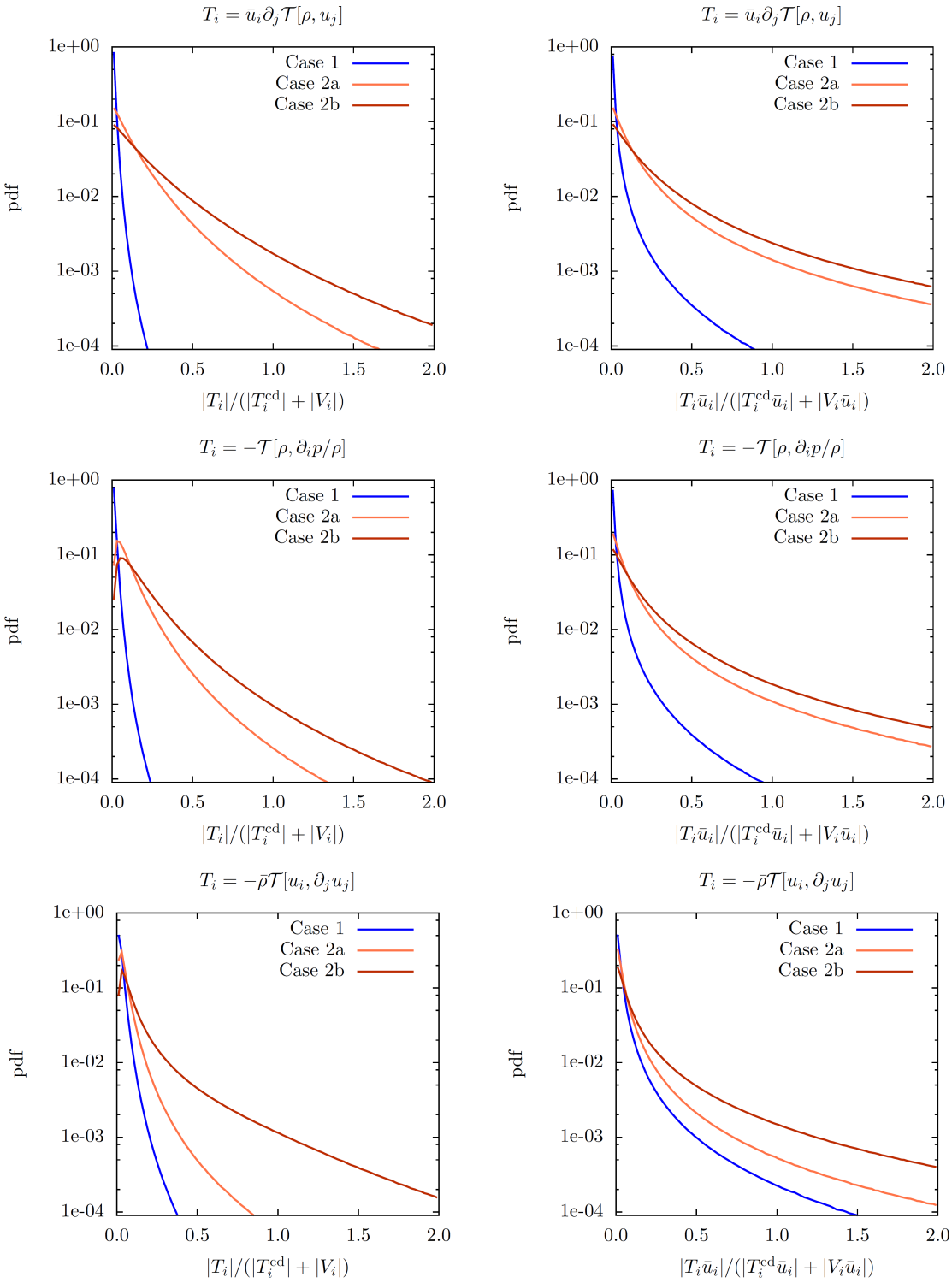

Figure 5.13: Probability distribution functions of the relative magnitude (left) and relative projection (right) for SGS terms in $\partial_t \bar{\rho}\bar{u}_i$ equation from instantaneous flow field.

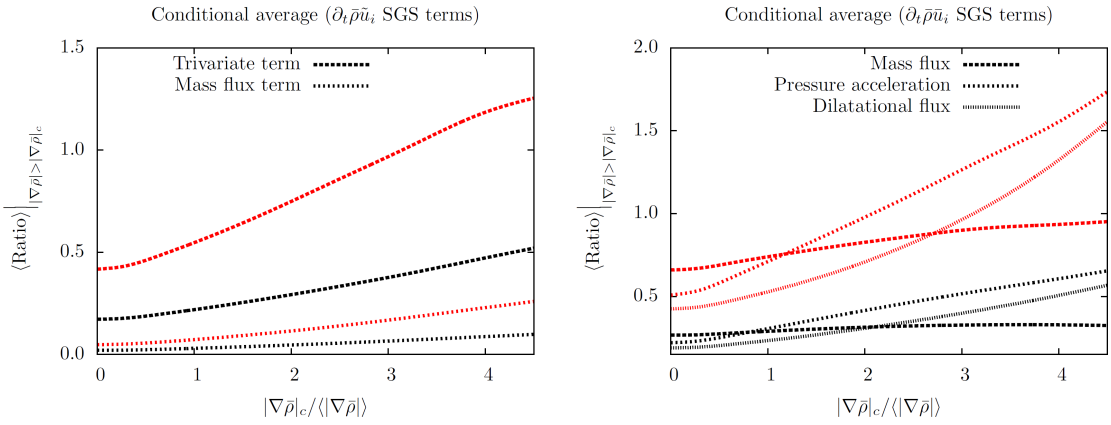

Figure 5.14: Conditional volumetric averages of relative magnitude (black) and relative projection (red) for SGS terms in Favre-filtered equation (left) and Reynolds-filtered equation (right) from instantaneous flow field.

Favre-filtered equation by projection metric is for Case 2b and 0 for Case 1. We note that averaging the ratio field over the entire volume suppresses the importance of variable-density SGS terms as it causes the average to be biased by homogenized flow pockets where the ratio values are close to zero. Therefore, for Case 2b, we present conditionally averaged ratio value in figure 5.14. The conditional average is the average over regions where $|\nabla\bar{\rho}|$ is greater than a specific value $|\nabla\bar{\rho}|_c$. As the value of $|\nabla\bar{\rho}|_c$ is increased, the conditional mean of the ratios corresponding to all terms is seen to increase. This implies that when regions with strong density gradients are sampled, variable-density SGS terms become relatively more important, even in a statistical sense. For case 2b, the mean values of variable-density terms are found to be larger than specific stress term from a projection metric in regions of strong resolved-scale density gradients.

Ratio distributions for the filtered vorticity transport equation are also computed . There are three inviscid SGS terms in the equation: the SGS vorticity flux $\partial_j\mathcal{T}\left[\omega_i, u_j\right]$, the SGS vortex stretching term $\mathcal{T}\left[\omega_j, \partial_j u_i\right]$, and the SGS baroclinic torque $\nabla\times\mathcal{T}\left[\partial_i p, 1/\rho\right]$. The pdf plots quantifying the importance of the SGS baroclinic torque relative to the SGS vorticity flux $\partial_j\mathcal{T}\left[\omega_i, u_j\right]$ and the SGS vortex stretching term $\mathcal{T}\left[\omega_j, \partial_j u_i\right]$; are plotted in figure 5.15. Both metrics, magnitude, and projection on $\bar{\omega}_i$ are considered. Projecting the SGS vectors onto the resolved-scale vorticity, similar to the projection of the SGS terms in momentum equation on the resolved-scale velocity, represents the

contribution of each SGS term to resolved-scale enstrophy $\bar{\omega}_i\bar{\omega}_i/2$. The resolved-scale viscous term $\nabla \times \bar{\sigma}_{\rho u_i}/\bar{\rho}$ is used for regularization of the denominator to compute the ratio fields. The ratio of SGS baroclinic torque to both SGS vorticity flux as well as SGS vortex stretching is computed, and is found to be important for Cases 2a and 2b, but unimportant for Case 1.

We now synthesize the important findings from the analysis. Turbulent flow fields with active variable-density effects have been investigated to quantify the role of variable-density SGS terms on the dynamics of the Favre-filtered and Reynolds-filtered velocity fields. Evidence for the significance of these terms is provided in the form of pdfs of their magnitude relative to the constant-density SGS terms. Two scalar metrics are chosen to compare the SGS vectors, namely their magnitude and their contribution to kinetic energy production and dissipation.

For the $M_t = 0.3$ flows studied, it is found that density fluctuations arising out of compressibility alone are weak, and that SGS terms arising from small-scale density fluctuations are also negligible. However, when density fluctuations are associated with thermal inhomogeneities, they interact with the pressure gradient field to produce acceleration fluctuations, thereby affecting velocity gradients. Not only is vorticity affected, but the dilatation content is also significantly altered. Therefore, flow compressibility strongly couples with thermal density inhomogeneities, and consequently, the flow dynamics of compressible variable-density turbulence are inherently different from incompressible variable-density turbulence [97]. Although we do not study compressible turbulent mixing of variable-density fluids with different molecular weights, such flows are expected to exhibit non-negligible variable-density SGS terms as well.

The analysis discusses variable-density effects on the Favre-filtered velocity SGS stress tensor in terms of central moments under the filter, which represent the spatial correlation between small scales. The trivariate moment $\mathcal{T}[\rho, u_i, u_j]$ is found to be the most dynamically important variable-density term in the SGS stress. The physics of this term merit attention because it contributes significantly to the computable resolved-scale kinetic energy $\bar{\rho}\tilde{u}_i\tilde{u}_i/2$. Using the new Reynolds-filtered momentum equation, we isolate the SGS inertial and dilatational effects and establish the dynamical importance of specific terms. The new form of the equations represents the effect of SGS pressure-acceleration, as well as the SGS mass flux and SGS dilatation correlations in

resolved-scale mass, velocity, and internal energy. The new SGS terms also provide a framework to study variable-density counter-gradient diffusion independently of the constant-density SGS terms. For example, in Case 2b, we find that SGS mass flux term and SGS pressure-acceleration term have a net positive contribution to $(1/2)\partial_t \bar{\rho}\bar{u}_i\bar{u}_i$, as opposed to SGS specific stress, which has a net negative contribution. In other words, while the constant-density terms drain energy from the large scales, two variable-density SGS terms transfer kinetic energy to the large scales.

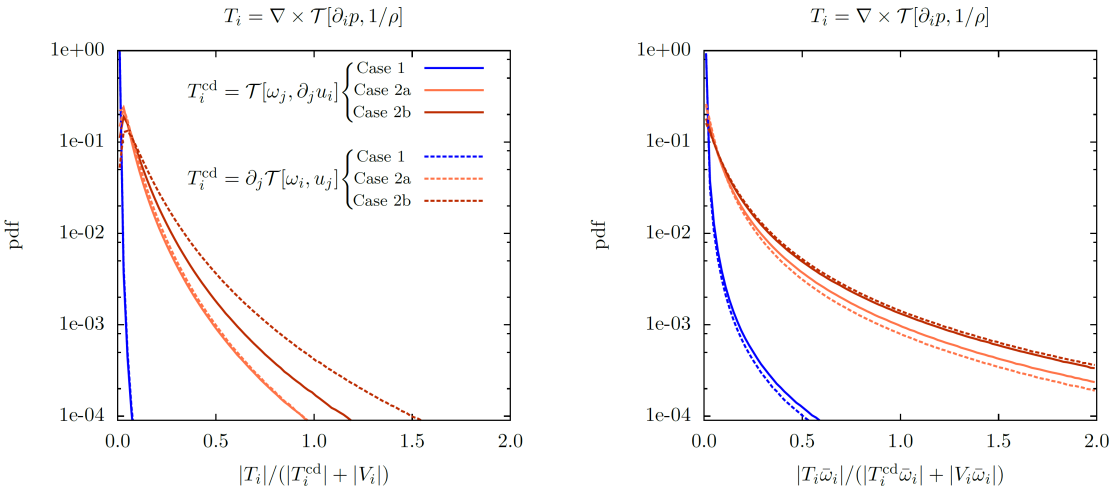

Figure 5.15: Probability distribution function of relative magnitude (left) and relative projection (right) for SGS terms in $\partial_t\bar{\omega}_i$ equation from instantaneous flow-field.

5.2 Mixing transition by shock-deposited baroclinic vorticity

Richtmyer-Meshov instability is a canonical flow problem where a distorted heavy-light gas interface is subjected to impulsive acceleration and the baroclinic vorticity production can often lead to late-time mixing transition. Inspired by presence of finite thickness gas layers in real-life flow problems, turbulent mixing in a gas-curtain setup has been investigated at Los Alamos National Laboratory for over a decade[86]. The setup consists of a row of closely spaced jets of heavy gas (SF6+tracer) flowing vertically downward from a linear array of nozzles with coflow (for stabilization). This initial heavy-gas flow

forms an effective gas curtain of varicose thickness, with maxima along the centerline of the nozzles. During the experiment, a planar shock wave in the air (lower density) passes through the gas curtain and exits the test region into air downstream. Due to the impulsive acceleration of the shock wave, both upstream and downstream interfaces are Richtmyer-Meshkov unstable and distort due to the array of counter-rotating vortices produced as the curtain moves downstream. At the upstream interface, interfacial perturbations grow in phase with the initial profile while at the downstream interface, the perturbation growth is out of phase with the initial profile. The varicose nature of the gas curtain thickness therefore transforms into a sinuous instability pattern leading to eventual growth of mushroom like structures during the non-linear phase of the instability. The resulting mixing layer can be made to interact with the original shock again (reshocked) by reflecting it off a wall. The reshock process is associated with deposition of multi-scale baroclinic vorticity and leads to rapid mixing transition. In the absence of reshock, only strong shocks can deposit enough vorticity to cause turbulent breakdown at late stages. However, the reshocked gas curtain, like reshocked Richtmyer-Meshkov problem leads to rapid breakdown and also serves to study the influence of multi-modal initial conditions in density and velocity field on late time mixing behavior post shock passage. In the experiments, evidence of inertial range development has been observed.

Several computational studies on Richtmyer-Meshkov turbulence and some on gas curtain turbulence have been reported in the literature. Most studies are coarse-grained simulations at high Reynolds numbers, primarily to replicate experimental conditions. Since the flow problem is highly non-linear, the spectral nature of the initial conditions as well as details of the numerical schemes affects the uncertainty in small-scale dynamics. A comparison of turbulent mixing produced by Richtmyer-Meshkov instability with two different methods on the same initial conditions is discussed in Tritschler et al. [117]. Similarly, two different sets of initial conditions: with narrow band and broadband spectral signatures were considered in several numerical studies. Development of a turbulent cascade is faster with broadband initial spectrum. Interestingly, the initial spectral content also affects the slope of the Fourier spectrum of energy and scalars at different stages of the problem.

Theories for spectral scaling in RMI type flows are scarce. Some phenomenological theories exist. Zhou [132] predicts a -3/2 spectrum based on external agent time scales.

The work of Hill et al. [52] with self consistent large-eddy simulations using the stretched-vortex subgrid-scale model propose a -5/3 continued spectrum.

In the results that follow, we study the characteristics of the flow that develops after the passage of the shock. The SGS terms in the momentum equation are computed at different time instances to identify their relative contribution.

5.2.1 Numerical setup and validation

We validate our numerical setup with 2D computations of experiments carried out at LANL by Balakumar et al. [4] that study the effect of a shocked SF_6 cylinder and an SF_6 gas curtain. The schematic for the initial setup of the two flows is shown in Figure 5.16. Shock heavy-gas cylinder interaction involves baroclinic vorticity deposition leading to

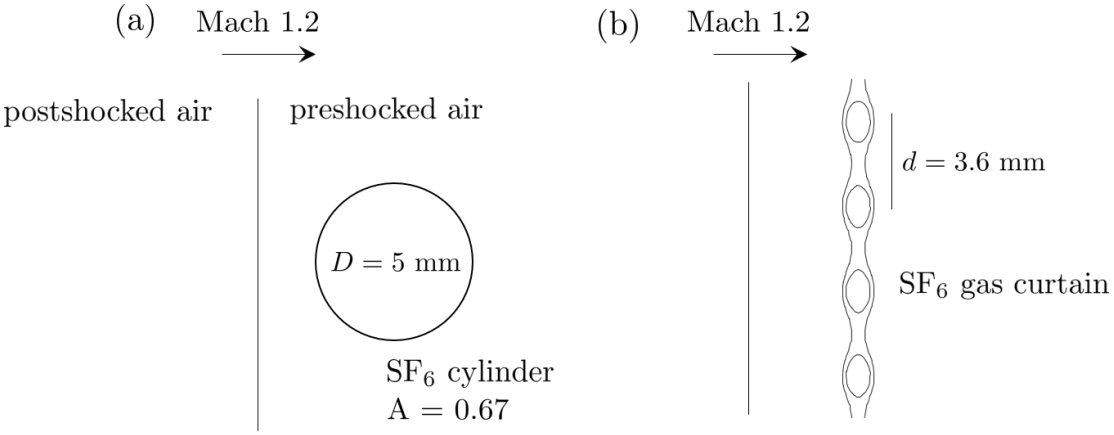

Figure 5.16: Schematic of the test cases for numerical validation

formation of a counter-rotating pair of vortices that cause mixing of the gas cylinder with ambient gas. The bridge of the heavy gas connecting the two vortex cores is associated with mass fraction gradient intensification due to rapid straining leading to large molecular mixing. In the vortex cores, scalar spirals develop and cause mixing due to increase in surface area. At intermediate times, secondary KH type instabilities develop in the outer edges of the vortices and in the cores due to vortex-accelerated baroclinic vorticity deposition. The gradient intensification is not only restricted to the mass fraction field but also the density field, thereby causing increased secondary baroclinic vorticity production. We simulate the interaction only in its two-dimensional

stages, before three-dimensional breakdown effects take over the mixing processes. The cylinder like the gas curtain case has inhomogeneity in the third direction due to gravity and diffusion effects.

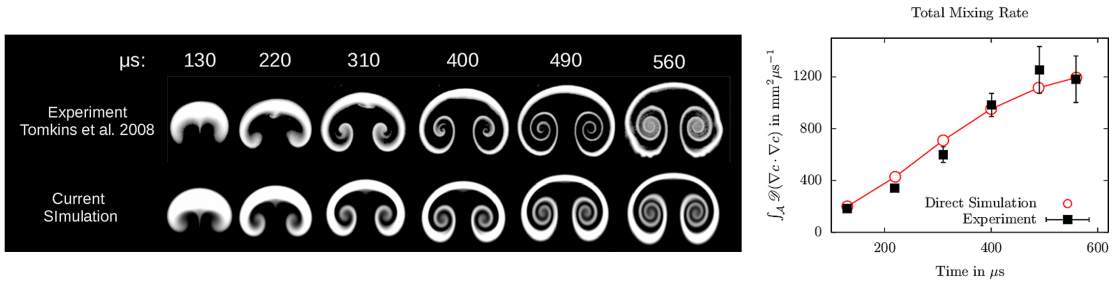

Figure 5.17: Time evolution of shock-heavy-gas-cylinder interaction.

The gas curtain is essentially a setup of several gas cylinders arranged in a row. The varicose nature of the heavy gas thickness results in formation of parallel counter-rotating vortex pairs on passage of the shock. The incident shock strength in the present case is not large enough to cause immediate transition to turbulence. To our knowledge, the simulation shown in Figure 5.18 is the most accurate representation of the flow in the experiment compared to past simulations reported in open literature. The key to the high temporal and structural accuracy of the gas layer evolution can be attributed to the correct initial condition. It is important to note that the intensity reported in the experiments is not a linear function of the SF_6 mass concentration. The two variables have a monotonic relationship and the maximum intensity may be calibrated with the correct Y_{SF_6} value, but the variation is weakly non-linear. This is the missing detail in other simulations that intended to reproduce the experimental results. Addition of small-scale noise, introduction of acetone in the heavy gas mixture and variation in the nozzle setup are important factors, but cannot account for the incorrect initial concentration map.

5.2.2 Computational setup

We simulate the reshock of a three-dimensional gas curtain that has been previously shocked with a Mach 1.2 shock. The homogeneity in the $y-z$ plane is important because if a 2D curtain is employed, the three-dimensional perturbations that cause

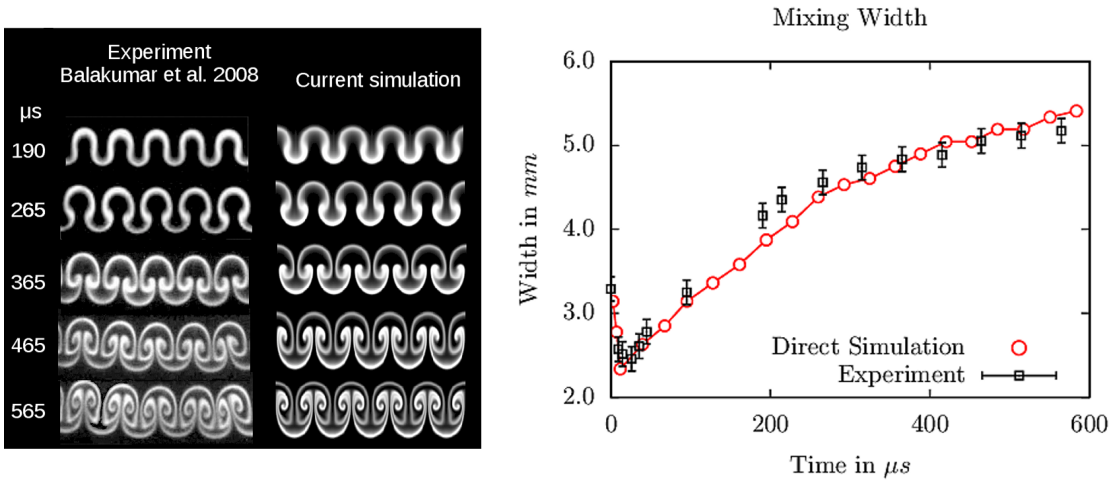

Figure 5.18: Time evolution of the 2D shock-heavy-gas-curtain problem. Mixing width is defined as the width between the locations where the $\langle Y_{SF_6} \rangle_y = 0.01$

turbulent breakdown can have their origin traced back to the dispersive properties of the non-linear scheme employed for shock and discontinuity capturing. This is clearly visualized in the simulations of Zhang and Shu [131] . The three-dimensional setup ensures that the mixing transition is not caused by numerics and grid convergence of the entire reshock dynamics can be demonstrated.

The reshock is caused by a Mach 1.17 shock, representative of a realistic interaction, where the Mach 1.2 shock that passes the curtain initially and reflects off the wall, has incurred losses. However, in our idealized setup, the rarefraction waves that can cause significant vorticity deposition, do not exist. The goal of the direct numerical simulation is to obtain a flow-field where multi-scale baroclinic vorticity plays a dominant role in the dynamics and analyze the flow for variable-density SGS interactions. Figure 5.19 shows the time-history visualization of the mass-fraction field. The initial field, obtained from non-linear growth in a 3D varicose curtain post interaction with a Mach 1.2 shock, differs significantly from the field obtained from a 2D varicose curtain discussed in the previous subsection. The shock passes the heavy gas layer by 25 μs and breakdown to turbulence is in its final stages by 200μs. Around 300-350 μs, the turbulence is fully broad-band and is in its decay stage. We are interested in analyzing the flow development post shock passage until it reaches a self-similar decay stage. The effect of

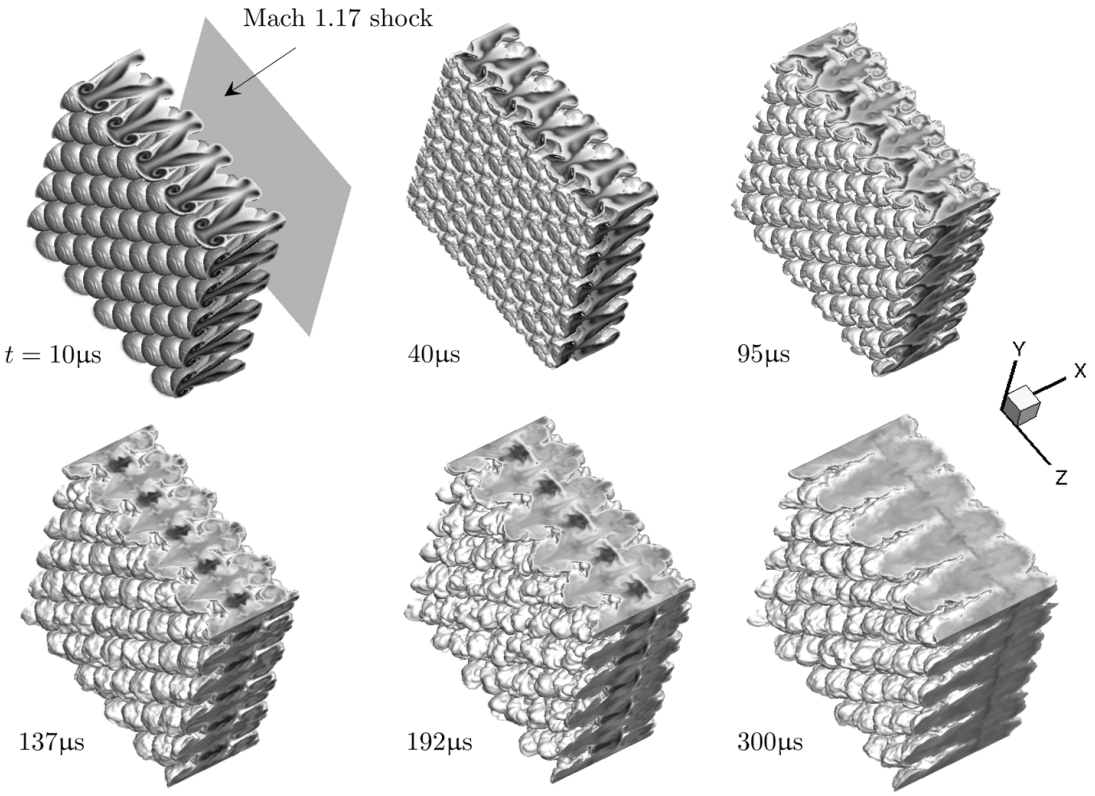

Figure 5.19: Evolution of the post reshock heavy gas layer visualized via grayscale Y_{SF_6} contour map between isosurfaces corresponding to $Y_{SF_6} = 0.01$.

initial conditions is clearly prevalent in all the stages considered in this work. Vortical

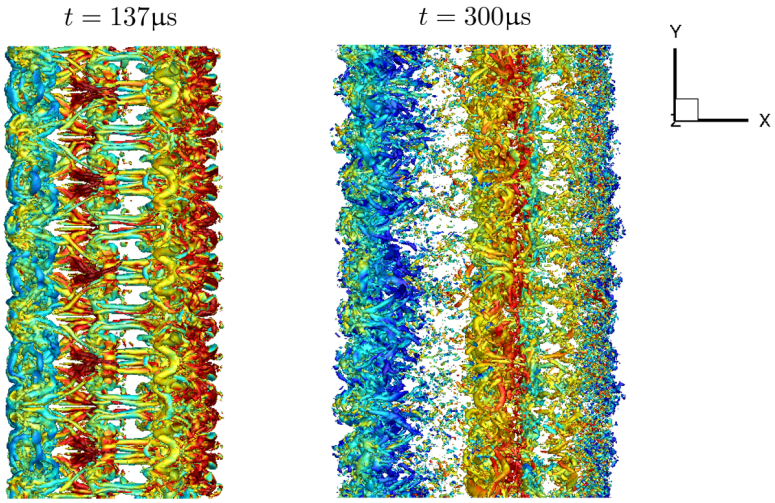

Figure 5.20: Vortical structures visualized with the second invariant of the velocity gradient tensor, colored with density.

structures visualized in Figure 5.20 are localized and strongly inhomogeneous in x. Late time turbulent structures indicate three turbulence zones corresponding to the edges and the centerline of the mixing layer. Density inhomogeneity in the mixing zone indicates that a well-mixed zone as in the case of canonical Richtmyer-Meshkov instability may not exist, and pockets of unmixed fluid entrained by the large-scale structures may not be molecularly mixed even in the late stages of flow development.

5.2.3 Turbulence and Mixing statistics

Figure 5.21 shows the growth of the mixing layer and mixedness using different metrics. δ_{Y1} and δ_ω are the mix widths corresponding to plane averaged mass fraction and vorticity profiles. δ_θ is defined as

$$\delta(t) = \int_{-\infty}^{+\infty} 4 \langle Y_{\mathrm{SF}_6} \rangle_{yz} \left(1 - \langle Y_{\mathrm{SF}_6} \rangle_{yz}\right) dx \tag{5.5}$$

where the averaging operator is the $y - z$ plane average. In RM flows, the mixed width is algebraic, typically of the form $\delta(t) \sim (t - t_0)_r^\theta$ where θ_r depends on the initial

perturbations and the shock Mach number. In our case, the definition of mixed width varies depending on the definition. Mixedness is defined by Youngs [128] as

$$\Theta_Y(t) = \frac{\int_{-\infty}^{+\infty} \langle Y_{\mathrm{SF}_6}\,(1 - Y_{\mathrm{SF}_6})\rangle_{yz}\,dx}{\int_{-\infty}^{+\infty} \langle Y_{\mathrm{SF}_6}\rangle_{yz}\left(1 - \langle Y_{\mathrm{SF}_6}\rangle_{yz}\right)dx} \tag{5.6}$$

We quantify mixedness based on volume fraction and mass fraction. Volume fraction based definition yields higher mixedness.

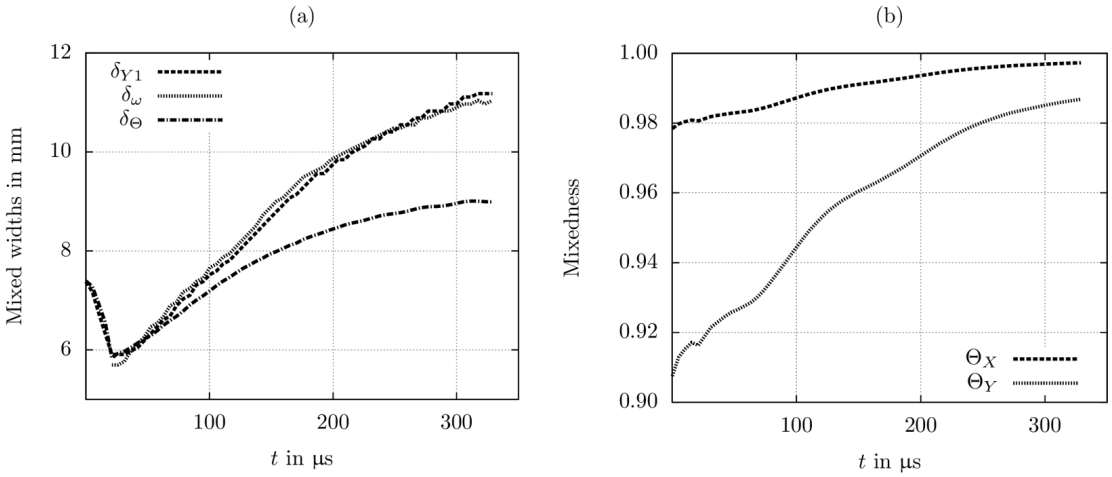

Figure 5.21: Mixed widths (a) and mixedness (b) as a function of time.

The time evolution of pdfs of the density and the mass fraction field provides a more detailed state of mixing in the flow-field as a function of time. The density and the mass fraction fields slowly approach a fully mixed state, which would imply convergence to a Dirac delta function in the pdf plot. At 300 μs, the pdfs of the field in the volume considered are seen to have a hump corresponding to the mixing layer state and the sharp peak corresponding to the ambient gas state outside the mixing layer. Presence of two maxima in the density and the scalar fields implies a two-stage mixing process, of which only one is captured in our simulation. The first corresponds to establishment of a homogeneous mixed state within the heavy gas layer from a partially mixed state caused by the vorticity from the initial reshock. Next, the fully mixed moderately heavy gas layer mixes with the ambient air. In the present simulations, we do not investigate this second stage of mixing.

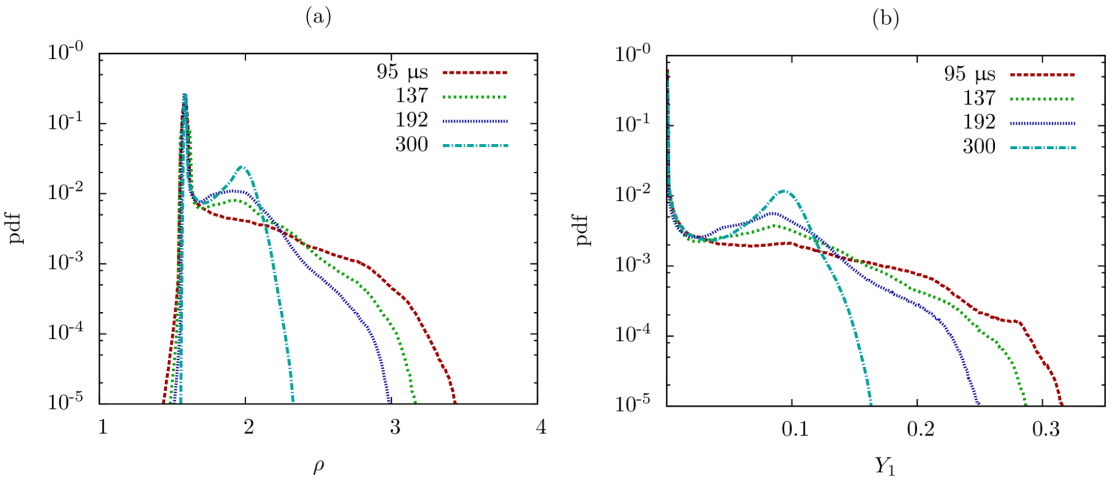

Figure 5.22: Time-evolution of (a) density and (b) heavy gas mass fraction.

Figures 5.23 and 5.24 show the evolution of the cross-plane specific energy and density spectra. The time evolution of the spectra for heavy gas mass fractions is similar to density and is not plotted. The spectra clearly exhibit a two-stage dynamics (different from the mixing stages discussed earlier). Initially, post reshock, the specific energy is amplified across all wavenumbers. This is followed by flow of energy into the smaller scales. This cascade process may be attributed to vortex stretching of the vorticity deposited by baroclinic torque. After the cascade of energy in the small-scales, the non-linear spectral smoothening of the spectrum occurs. It is during this stage that the onset of turbulence has begun, and is followed by decay and further transfer of energy to smaller scales. In this work, the Reynolds number based on u_{rms} and dissipation rate ϵ at 200 µs is 60.

5.2.4 A priori subgrid-scale estimates

The fields in the reshocked gas layer are filtered explicitly using a Gaussian filter at a length-scale $\Delta_c/Delta = 8.5$ which corresponds to $\Delta_/L = 0.03$ for SGS analysis. We first compute the SGS terms in the Favre-filtered momentum equation. From Figure 5.25 we infer that the variable-density SGS terms, referred to with labels T2 and T3 are not very large in a mean sense. The volume average is done in the entire test section of the simulation, $0 < x/L < 1$ and is not restricted to the mixing layer region.

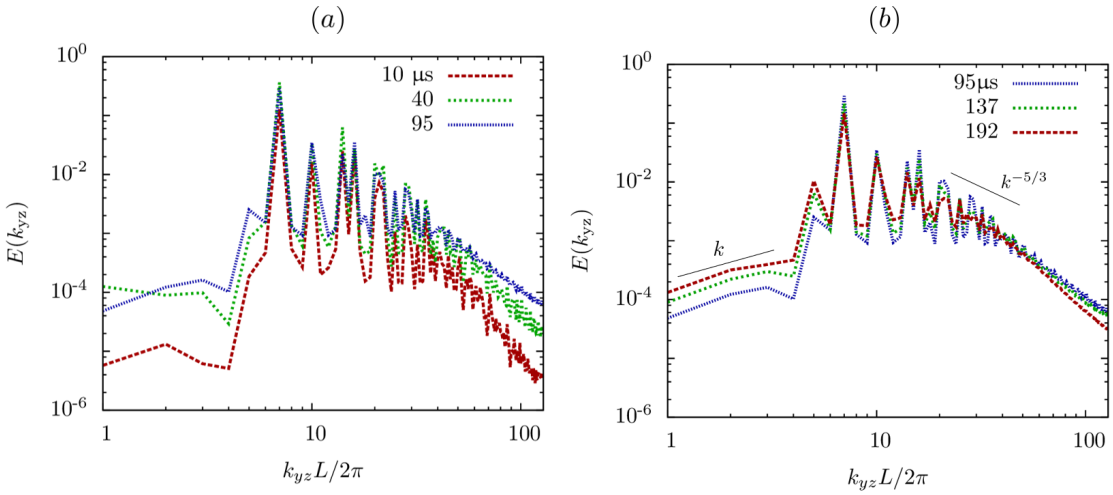

Figure 5.23: Specific kinetic energy spectra in the 2D wavenumber space: time evolution during (a) amplification stage and (b) non-linear spectral-smoothening stage.

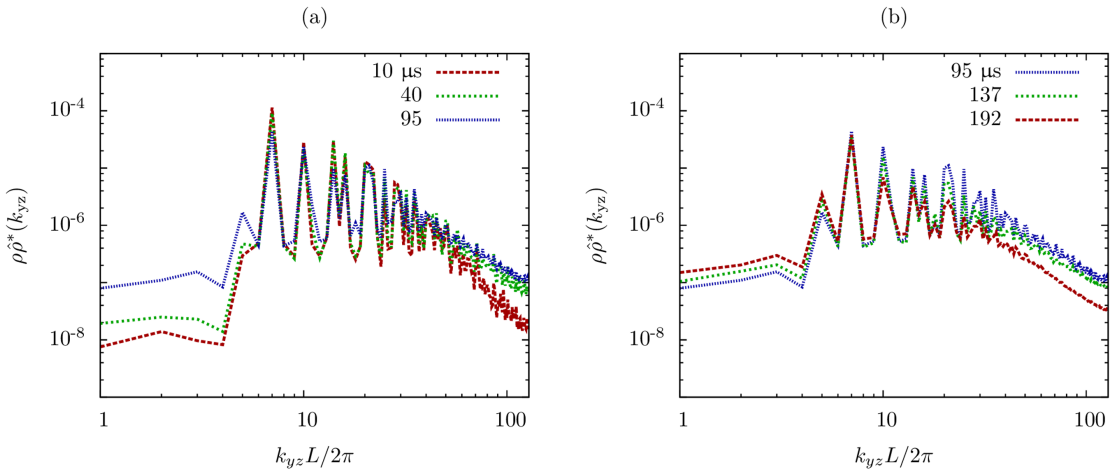

Figure 5.24: Density power spectra in the 2D wavenumber space: time evolution during (a) amplification stage and (b) non-linear spectral-smoothening stage.

However, the volume averages are representative of the strength of the SGS terms in the transitional and fully turbulent regions of the mixing layer. Variable-density effects clearly seem to decay as the mixing layer becomes fully turbulent towards 200 μs. The SGS triple moment is larger than the SGS mass flux term, as was observed in the case of decaying turbulence.

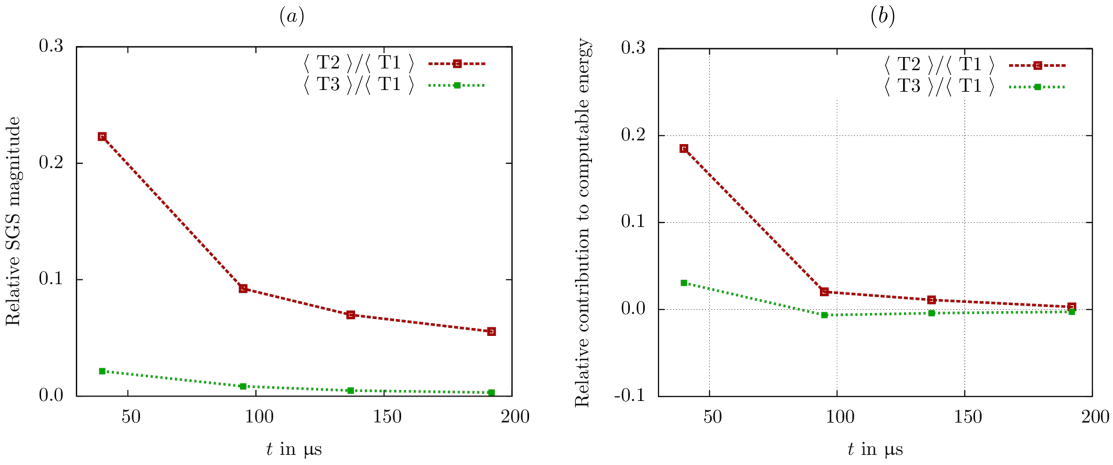

Figure 5.25: SGS terms in the Favre-filtered velocity based momentum equation. T1 is the SGS specific stress term, T2 is the SGS triple moment and T3 is the SGS mass flux term.

The Reynolds-filtered momentum equation displays different characteristics. While the SGS mass flux term is relatively small and dynamically insignificant, the SGS pressure acceleration term and the SGS velocity dilatation terms (labeled as T3 and T4 in Figure 5.26) are large. This indicates that SGS variable-density effects are more prominent in the equation for $\bar{u}_i$ compared to $\tilde{u}_i$. Both the terms remain relatively large until the mixing layer becomes fully turbulent. The large magnitude of the velocity-dilatation correlation term is surprising, but may be attributed to acoustic waves emanating from the transitional mixing layer. However, due to low compressibility of the flow, large velocity-dilatation correlation at the small scales requires attention. The sensitivity to filter-width and aliasing error buildup at small velocity scales in the simulation must be carefully studied for any physical conclusion drawn from the SGS velocity dilatation field.

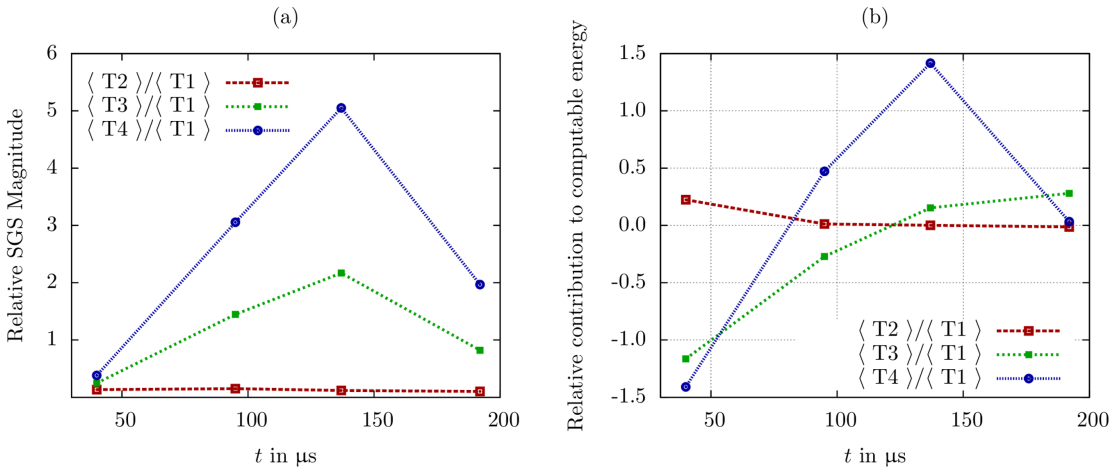

Figure 5.26: SGS terms in the Reynolds-filtered velocity based momentum equation. T1 is the SGS specific stress term, T2 is the SGS mass flux convection, T3 is SGS pressure acceleration term and T4 is the SGS velocity-dilatation correlation.

5.3 Conclusions

In this chapter, we performed direct numerical simulations of variable-density turbulent mixing at moderate Taylor-scale Reynolds numbers to quantify the strength of variable-density SGS terms that appear in the Favre-filtered and the Reynolds-filtered momentum equations. By explicitly filtering the DNS flow-fields, we find that the variable-density SGS terms can be locally large in the regions of large filtered density gradients. In particular, we observe that density variations affect velocity gradient fields more significantly than the kinetic energy, indicating higher sensitivity of the small velocity scales to variable-inertia effects. Of interest is also the increased dilatational (acoustic) fluctuations caused by density variations. Interaction of acoustic waves with stratified fluid produces baroclinic vorticity, which in turn generates acoustic waves due to the compressible nature of the flow. This process can produce more dilatational fluctuations than in canonical compressible turbulence. The magnitude of SGS terms involving dilatation reflect the presence of increased fluctuations. The multiscale nature of the dilatational field in compressible variable-density turbulence and its relationship to the vorticity field is important to understand for designing improved closures. In addition to analyzing the variable-density SGS effects, an important quantity is the trace

of the SGS specific stress, or SGS kinetic energy in the case of a Reynolds operator. Although the quantity involves spatial correlations of the velocity field, it is also affected by variable-density effects in the flow, via the small scale velocity field. The dynamics of the SGS specific stress and its trace, primarily the imbalance between the global production and dissipation due to baroclinic vorticity generation requires investigation.

Chapter 6

Large eddy simulations: *a posteriori* estimates

In this chapter, we carry out large eddy simulations of compressible variable density turbulent flows and provide estimates of variable-density subgrid-scale terms. Two flow-setups with heat release are considered. The first corresponds to a supersonic reacting flow in a recirculating mixing layer configuration with H2-F2 chemistry. The second case corresponds to shock-induced combustion of spherical inhomogeneity of dense H2-O2 gas mixture. The cases are simulated at resolutions constrained by computational resources, but nevertheless capture the dominant features of the flow-fields. Quantitative estimates are based on the subgrid-scale models employed with filter widths of the order of the grid cells.

6.1 Supersonic expansion ramp combustion

Supersonic combustion requires a high degree of molecular mixing between the fuel and the supersonic air stream. Yet, for sustenance of the combustion process, strong strain rates, that can extinguish flames, may not exist in the flow. Combustor design must also account to minimize total pressure loss for high propulsive efficiency.

Bonanos et al. [8] considered an expansion ramp geometry where the top high-speed stream is expanded over a ramp and the bottom stream is injected through perforations in the expansion ramp. When the bottom-stream flow cannot satisfy the entrainment

requirements of the shear layer, the shear layer reattaches as in a backward-facing step. In a reacting flow, the top stream re-entrant jet in the recirculation interacts with bottom-stream fluid to form a secondary shear layer where the ramp meets the bottom guide wall. The recirculating region, reentrant jet and the secondary shear layer lead to enhanced mixing relative to a free-shear layer. The length of the recirculation zone is controlled through the mass-injection ratio of the two streams. Increasing injection pushes the reattachment downstream. For high mass-injection ratios, the flow becomes similar to a plane shear layer. Heat release in the reacting case is equivalent to increasing the bottom stream mass flux in the non-reacting case due to reduced volumetric entrainment of free-stream fluid [51].

In this section, we consider a supersonic top stream with hydrogen and diluents reacting with a diluted fluorine stream injected from the ramp. Both, low and high heat release cases corresponding to rich and lean burn configurations are simulated. Heat release effects are pronounced in the lean case and it is therefore used for quantifying the modeled subgrid-scale terms. From a computational perspective, important uncertainties in the experiments are the inflow pressures in the top and the bottom stream and the exit backpressure. The inflow pressures determine the angle of the shear layer, while the backpressure strongly affects the reattachment region and its low-frequency dynamics. We attempt to infer these quantities from the experimental schlieren. While these factors make comparison of the simulations to the experimental data challenging, we are primarily interested in the large eddy simulation fields in a compressible reacting regime.

6.1.1 Details of experiments

The experiments reported in Bonanos et al. [8] have been performed in the Supersonic Shear Layer (S^3L) laboratory at Caltech. The experiments study mixing between gaseous streams in an expansion ramp geometry, similar to a rearward-facing step. This geometry while minimizing total-pressure losses, involves a recirculation zone and avoids high strain-rates to stabilize the flame. The experiments quantify molecular mixing in such a configuration using the "flip" experiment technique. This technique involves two sets of experiments with the compositions of the two gas streams interchanged. The reactions that occur upon molecular mixing are designed to lie in the fast-kinetic regime

and hence, chemical product formation is limited by mixing. The temperature rise associated with product formation in the two experiments is used to quantify mixing.

The experimental facility is a two-stream blow-down wind tunnel. The top stream is seeded with hydrogen H_2, nitric oxide NO and the bottom stream is seeded with fluorine F_2. Gases in both streams comprise of inert diluents to match mean molar mass and specific-heat ratio. NO is added as a catalyst in H_2 stream to generate radicals and initiate hydrogen-fluorine reaction. It combines with F_2 resulting in the in the hypergolic reaction NO + F_2 → NOF + F at room temperature. The test section, and the reaction set employed in the present computations, is shown in Figure 6.1.

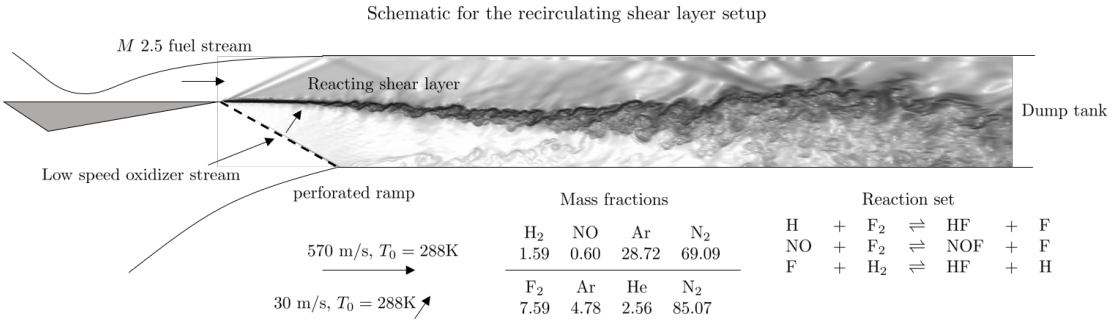

Figure 6.1: Schematic for the S3L facility at Caltech for studying supersonic mixing layers in an expansion ramp configuration.

As shown, the bottom stream is injected through the inclined expansion ramp, perforated with an open area fraction of 0.6. The measurement rake is placed downstream of the ramp . The experimental combustor's pressure coefficient is controlled with ramp mass injection and heat release. Using the information from the temperature sensors, the fraction of mixed fluid within the mixing layer is reported as

$$\frac{\delta_m}{\delta_p} = (1 - Z_{\phi=\phi_1}) \left[\frac{\delta_p}{\delta_t}\bigg|_{\phi=\phi_1} + \frac{\delta_p}{\delta_t}\bigg|_{\phi=\phi_2} \right] \tag{6.1}$$

where δ_p is the product thickness normalized by the temperature rise profile.

$$\delta_p = \int_{-h/2}^{h/2} \frac{\Delta T(y)}{\Delta T_f} dy \tag{6.2}$$

δ_t is the distance from the lower wall at which the temperature profile reaches 1% of

its normalized value. ϕ_1 and ϕ_2 are the equivalence ratios of the two experiments. Previous research in the facility reports that for the flow to be mixing limited such that the molecularly mixed fluids react completely, the Damköhler number (ratio of mixing time scale to the chemical-reaction time scale) $Da > 1.5$. For a range of inflow velocities, unlike free shear layers, increase in mixing with streamwise distance was observed in these experiments. As mentioned in Matheou et al. [77], the flip experiment technique also relies on the assumption that the flow-field does not change with heat release. The two experiments were considered to match on the basis of stagnation pressure profiles. While heat release may be a factor, computational evidence suggests that the flow behavior is more sensitive to the inflow pressures. In the Mach 2.5 experiment runs, the data suggests that the flow-fields are not sufficiently similar to be considered as candidates for estimation of molecular mixing. At the same measurement location, the low heat release flow displays shear-layer like characteristics, while the shear layer in the high heat release case has reattached and possibly separated again, before exiting the test section.

6.1.2 Computational Setup

The computational setup is illustrated in Figure 6.2. Finite rate chemistry for the H-F system is employed. Flow and composition details at the inlet may be found in Bonanos et al. [8]. Details for chemistry employed in the computation may be obtained from Kartha et al. [58].

In this study, for estimating the inflow profile in the top stream, a steady state laminar flow is computed in a Mach 2.5 nozzle used in the facility to obtain the top stream inflow conditions for the test section. The velocity and density profiles obtained from the steady state calculation are shown.

The outflow treatment is designed to resemble the experimental conditions. This contributes to the stability and accuracy of the computation, owing to the subsonic nature of the flow at the exit of the test section. In the experiment, the test section exits into a cylindrical dump tank where the products of the reaction are neutralized. In the computation, the dump tank is also simulated as a part of the flow domain as shown in Figure 6.2. The dump tank grid is however highly stretched in the radial and the axial directions. Also, chemistry and high order spatial numerics are gradually

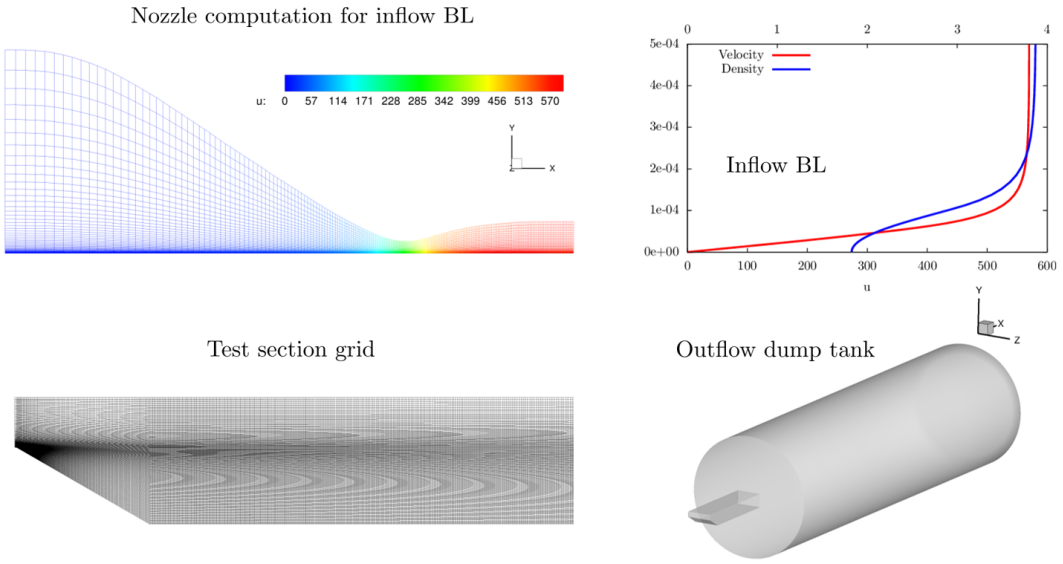

Figure 6.2: Computational setup associated with simulation of the supersonic reacting shear layer on an expansion ramp.

turned off as the flow enters the dump tank. All walls in the simulation are slip walls to avoid large computational cost associated with capturing the boundary layers in the top and bottom walls. The number of grid elements in the three-dimensional geometry is approximately 10 million with a 9:1 ratio for the number of elements in the test section to the number in the dump tank.

The initial condition for the three-dimensional simulations is a reacting two-dimensional flow obtained using 2D computations of an identical setup. The dump tank is however reinitialized to zero velocity, atmospheric pressure and nitrogen gas for the 3D computations.

6.1.3 Subgrid-scale closures

In the present computations, we utilize the stretched-vortex model for closure of the SGS specific stress and SGS scalar fluxes. For SGS pressure acceleration and SGS velocity

dilatation correlation, we use the gradient model.

$$\mathcal{T}[a,b] = \overline{ab} - \bar{a}\bar{b} \simeq G(a,b) = \frac{\Delta_c^2}{12}\frac{\partial \bar{a}}{\partial x_k}\frac{\partial \bar{b}}{\partial x_k} \tag{6.3}$$

Note that the stretched-vortex model is responsible for the appropriate SGS energy dissipation, which allows retention of the structural performance for the variable-density SGS terms associated with the Reynolds-filtered velocity.

We summarize the original stretched-vortex model[79, 119]. The stretched-vortex SGS model is based on a physical model for turbulent small scales wherein vorticity is concentrated in an ensemble of tubular structures. These structures have a two-dimensional spiral cross-section and stretch in an axisymmetric strain-rate field. The flow on the segment of a filament can be simplified as an axially stretched two-dimensional flow. The equations describing this flow admit analytical long-time asymptotic solutions from which ensemble statistics like the spectra and correlations are calculated. The subgrid-scale model therefore constructs an explicit description of the subgrid-scale velocity field: a superposition of stretched-spiral vortices in each computational cell with their orientation described by a probability density function (p.d.f.), $P(\alpha,\beta)$, where α and β are Euler angles relative to the laboratory frame. In the formulation where SGS ensemble dynamics is characterized by subgrid vortices aligned with Euler angles α_0 and β_0, the orientation p.d.f. is modeled with delta functions

$$P(\alpha,\beta) = \frac{4\pi}{\sin\alpha_0}\delta(\alpha-\alpha_0)\delta(\beta_0-\beta) \tag{6.4}$$

If the unit vector $\mathbf{e}_v$ along the vortex axis is

$$e_1^v = \sin\alpha_0\cos\beta_0, \quad e_2^v = \sin\alpha_0\sin\beta_0, \quad e_3^v = \cos\alpha_0 \tag{6.5}$$

the SGS stress tensor is given by the expression

$$\tau_{ij} = \bar{\rho}K(\delta_{ij} - e_i^v e_j^v), \quad K = \int_{k_c}^{\infty} E(k)dk \tag{6.6}$$

where K is the subgrid-scale specific kinetic energy, $k_c = \pi/\Delta_c$ and $\mathbf{e}^v$ is chosen to lie along the most extensive eigenvector of the resolved-scale strain-rate tensor $\tilde{S}_{ij}$. The

expression is obtained by assuming that the entire subgrid-scale specific kinetic energy resides in the two-dimensional plane of the subgrid vortices in an equipartitioned sense. In the case of wall turbulence, the expression is extended [23] taking into account the transport of axial velocity by the near-wall SGS vortices. The SGS energy spectrum $E(k)$ is obtained from the Navier-Stokes dynamics of the stretched-spiral vortices proposed by Lundgren[73].

$$E(k) = \mathcal{K}_0 \varepsilon^{2/3} k^{-5/3} \exp(-k^2 \lambda_v^2) \tag{6.7}$$

where $\lambda_v^2 = 2\tilde{\nu}/3|\tilde{a}|$. $\mathcal{K}_0$ is the Kolmogorov pre-factor; ε is the local dissipation rate; $\tilde{a} = \tilde{S}_{ij} e_i^v e_j^v$ is stretching along the SGS vortex axis imposed by the resolved scales, $\tilde{\nu}$ is the Favre-filtered kinematic viscosity. Integrating the spectrum, the SGS specific kinetic energy becomes

$$K = \mathcal{K}_0 \varepsilon^{2/3} k_c^{-2/3} P(k_c \lambda_v), \quad P(\kappa_c) = \frac{1}{2} \kappa_c^{2/3} \Gamma_{-1/3}(\kappa_c^2) \tag{6.8}$$

Here, Γ is the incomplete gamma function and the value of κ_c varies inversely with the strength of subgrid-scale activity. The constant $\mathcal{K}_0 \varepsilon^{2/3}$ is estimated from the local resolved-scale second order velocity structure function F_2 by matching it to the value predicted by the subgrid-scale spectrum. The structure function matching is done in a locally averaged sense.

$$\langle F_2 \rangle = \langle 4 \int_0^{k_c} E(k)[1 - J_0(kr)] \rangle \tag{6.9a}$$

$$F_2 = [\delta \tilde{u}_i]^2 = [\tilde{u}_i(\mathbf{x}) - \tilde{u}_i(\mathbf{y})]^2, \; r^2 = (\mathbf{x} - \mathbf{y})^2 - ((\mathbf{x} - \mathbf{y}) \cdot \mathbf{e}^v)^2 \tag{6.9b}$$

Here $\mathbf{y}$ is the integration variable; J_0 is the zeroth-order Bessel function of the first kind; and r is the distance from $\mathbf{y}$ to the vortex axis. The SGS specific kinetic energy can then be computed as

$$K = \frac{\langle F_2 \rangle}{\langle Q(k_c \lambda_v, d) \rangle} P(k_c \lambda_v, d) \tag{6.10}$$

where

$$Q(\kappa_c, r_c) = 4\kappa_c^{2/3} \int_0^{\kappa_c} \kappa^{-5/3} \mathrm{e}^{-\kappa^2} [1 - J_0(\kappa \pi r_c / \kappa_c) d\kappa, \quad r_c = r/\Delta_c \tag{6.11}$$

The averaging operator applied is the discrete ensemble average as shown below.

$$\langle \phi \rangle = \frac{1}{N} \sum_{\mathbf{y} \epsilon \mathcal{N}(\mathbf{x})} \phi \tag{6.12}$$

$\mathcal{N}(\mathbf{x})$ is the set of points neighbouring $\mathbf{x}$ where the resolved-scale information may be accessed. SGS heat flux q_j^T is closed with the expression given in equation 6.13. The expression is obtained by modeling the two-dimensional convective transport of temperature as a passive scalar by the SGS vortices.

$$q_i^T = -\frac{\overline{\rho} c_p \Delta_c K^{1/2}}{2} (\delta_{ij} - e_i^v e_j^v) \frac{\partial \tilde{T}}{\partial x_j} \tag{6.13}$$

Similarly, SGS mass flux is modeled as a passive scalar flux of density by the stretched-vortex velocity field using a SGS Schmidt number of 1.0.

6.1.4 Flow-field description

Figures 6.3 and 6.4 visualize an instantaneous snapshot of the high heat release case. The shear layer is highly inclined due to a pressure differential of 0.07 MPa between the top and the bottom streams. The time-scale associated with the flow development exceeds 2 ms. Due to restrictive time steps (of the order of 40 ns, we do not capture the steady-state statistics associated with the reattachment dynamics. However, the shear layer statistics is adequately captured as it develops over convective time scales.
Figure 6.5 shows the comparison of the mean temperature profiles with the experiment at the measurement location. The results corresponding to the high heat release case have been plotted at 1.5 ms, and change as time progresses. A careful study of the role of the dump tank and back pressure on the reattachment dynamics is warranted. The temperature rise plots show us that the Reynolds-filtered velocity equations can be successfully used for computation of supersonic flows with heat release.
To obtain the temperature rise plots, non-reacting computations were also carried out. Heat release is found to stabilize the mixing layer. Not only is the growth rate reduced, but the reattachment point is significantly delayed. This phenomenon, including the reduction in shear expansion angle is also observed in the experiment. Heat release increases the effective pressure coefficient of the combustor, as the experimental results

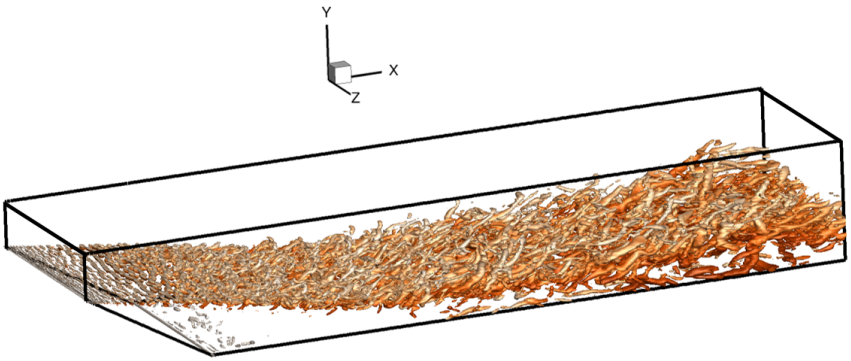

Figure 6.3: Large-scale vorticies visualized with the second invariant of the Reynolds-filtered velocity gradient tensor. The structures are colored with the product HF mass fraction. Orange represents high values and gray represents low.

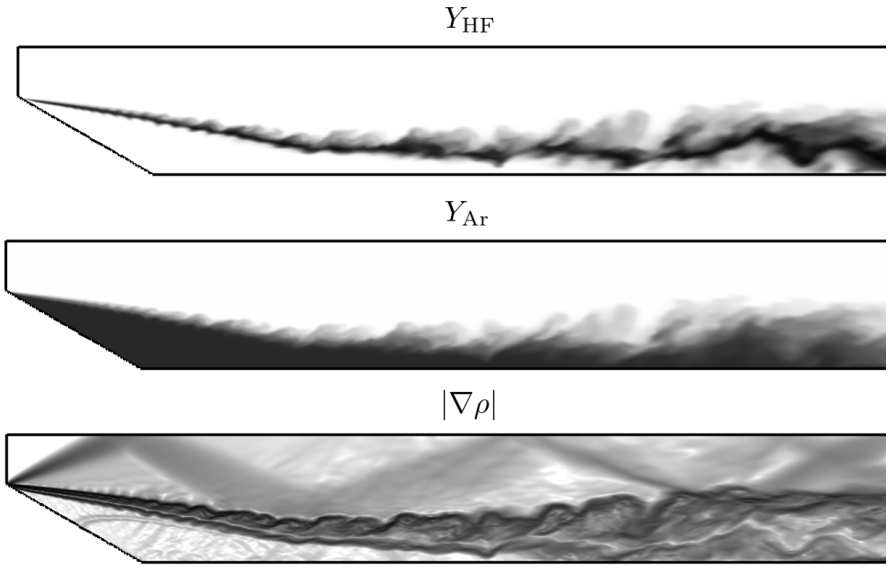

Figure 6.4: Mid-plane visualizations of fields at a time instance.

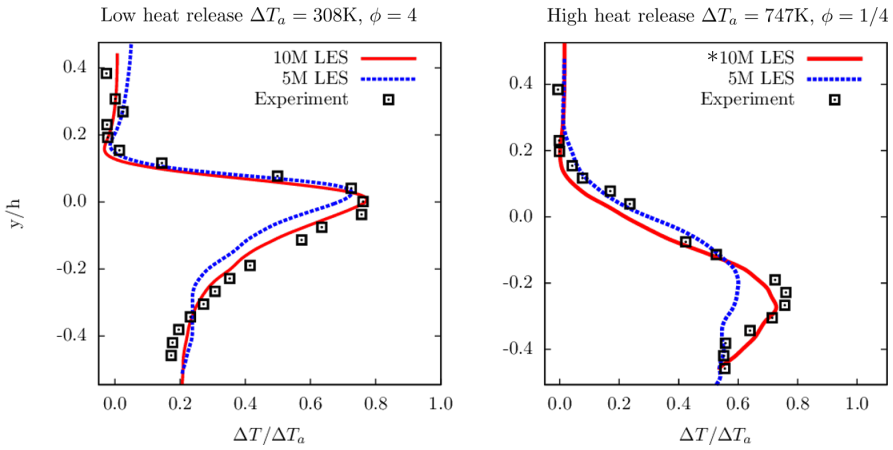

Figure 6.5: Comparison of normalized temperature rise profiles with experimental measurements. *Statistics are not temporally converged.

indicate. Note that in this simulation, all walls are assumed to be slip walls. This affects the temperature profiles due to the displacements effects associated with the boundary layer. More details on the flow-field in the low heat release case can be found in Sidharth et al. [104].

6.1.5 Subgrid-scale analysis

The subgrid-scale terms for an instantaneous flow-state are shown in Figure 6.6. An ensemble of flow realization at different time steps is considered. SGS statistics is evaluated from regions where the SGS kinetic energy estimated using the stretched-vortex model is greater than 10^{-6} times the mean value. This restricts the analysis to the turbulent mixing zone only. The primary result from the analysis points to the dominance of the SGS mass flux convection in the momentum equation. SGS pressure acceleration and SGS velocity dilatation do not appear to play an important role in this flow. Therefore, large-scale enstrophy dynamics is primarily driven by the SGS specific stress.

SGS mass flux ameliorates the density gradients in the reaction zone. This is also associated with diffusion of computable kinetic energy $(1/2)\bar{\rho}\bar{u}_i\bar{u}_i$. These dynamics are represented differently in Favre-filtered velocity based simulations, where SGS stress is

modeled using the Favre-filtered velocity with a closure model from incompressible literature. Let us consider the SGS effects in the momentum equations with a gradient diffusion model for the SGS mass flux and an eddy viscosity type model for Reynolds-filtered and Favre-filtered specific stresses. For the Reynolds-filtered momentum equation, we have

$$\overline{u}_i\mathcal{S}_\rho + \overline{\rho}\frac{\partial \mathcal{T}\left[u_i,u_j\right]}{\partial x_j} \approx -\bar{u}_i\partial_j(\nu_e\partial_j\bar{\rho}) - 2\bar{\rho}\partial_j(\nu_e\bar{S}_{ij}) \tag{6.14}$$

whereas in the Favre-filtered equation,

$$\partial_j\tau^{\mathrm{F}}_{ij} \approx (\widetilde{u_iu_j} - \tilde{u}_i\tilde{u}_j)\partial_j\bar{\rho} + \bar{\rho}\partial_j(\widetilde{u_iu_j} - \tilde{u}_i\tilde{u}_j) \tag{6.15}$$

$$= -2\nu_e\tilde{S}_{ij}\partial_j\bar{\rho} - 2\bar{\rho}\partial_j(\nu_e\tilde{S}_{ij}) \tag{6.16}$$

where S_{ij} is the trace-free strain rate tensor. Therefore, the difference in the modeled equations originates in the difference in the structural representation of turbulent mass diffusion. As is shown in Figures 6.6 and 6.7, the SGS mass convection term is by and large more important than the SGS specific stress term, and therefore structural modeling of this term requires more analysis and understanding in order to improve SGS modeling accuracy. Similar to momentum, SGS mass flux affects the species mass equations. While the SGS terms in the Favre-filtered equation contains terms of type $\partial_j\bar{\rho}\partial_j\tilde{Y}_s$, the corresponding Reynolds-filtered modeled term is of the type $\bar{Y}_s\partial_j\partial_j\bar{\rho}$. The pdfs show that this term is extremely important for mixing scalars. This is however, not the case for transport of product species mass.

In summary, the supersonic reacting mixing layer is dominated by specific stress and vorticity production by SGS baroclinic torque and SGS velocity dilatation is negligible. SGS mass flux is however important, and the accuracy of modeling its effect on the large scale momentum depends on the choice of the resolved-scale velocity and the model employed. However, the more important question concerns the closure in the species mass equations. Solving for Favre-filtered or Reynolds-filtered scalar is expected to make a difference in the time-averaged flow statistics. Although there is no combustion modeling in the present work, the choice of the resolved-scale scalar will bear important implications in the combustion modeling framework.

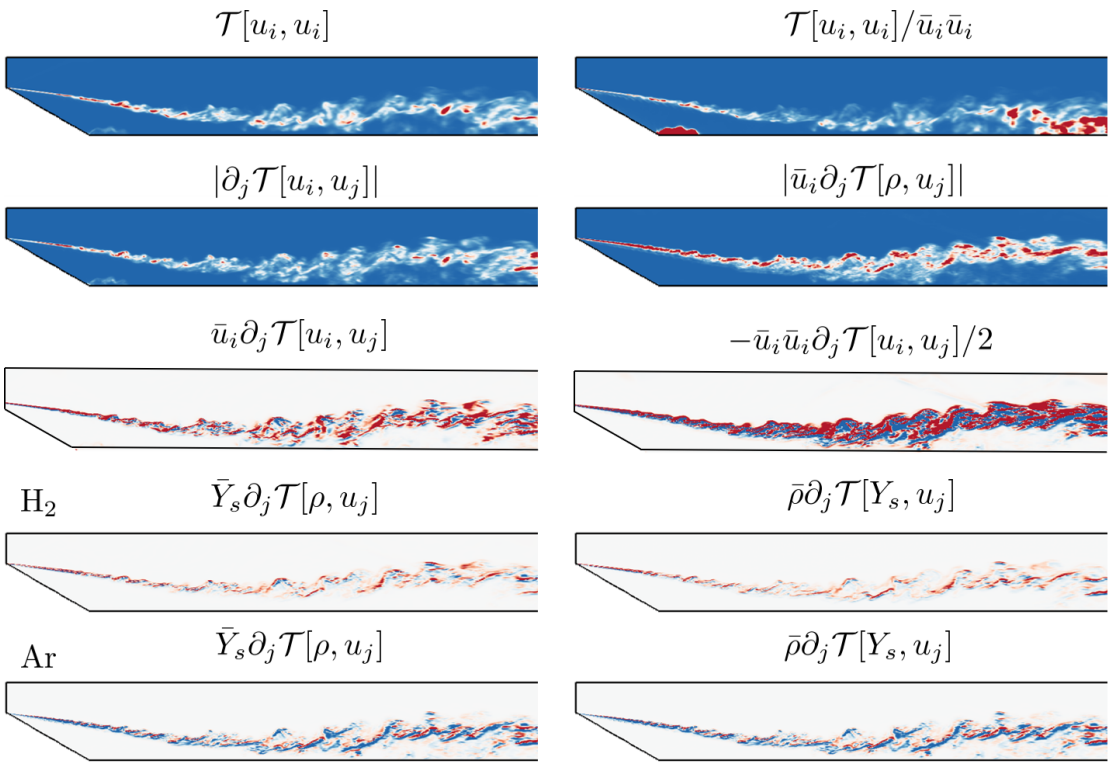

Figure 6.6: Modeled SGS fields from an instantaneous flow-field snapshot

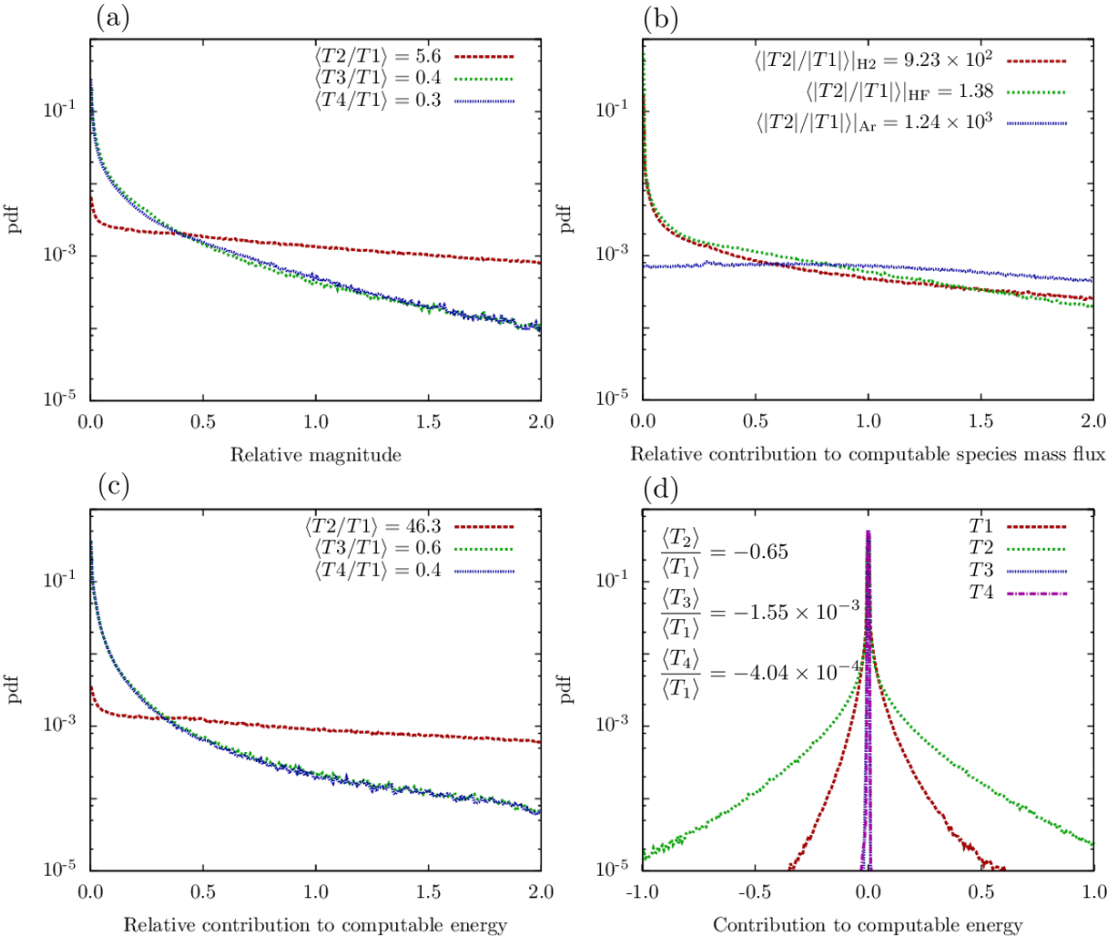

Figure 6.7: Pdfs associated with the modeled SGS terms

6.2 Reacting shock-bubble interaction

Shock-bubble interaction [88] involves impulsive acceleration of a spherical density inhomogeneity by a planar shock wave. The shock wave compresses the bubble, and the vorticity deposited by baroclinic torque results in development of a primary vortex ring followed by formation of secondary and near-turbulent flow structures at late time depending on the strength of the interaction. Acoustic impedance (product of density and sound speed) mismatch between the bubble and the ambient gas leads to non-linear acoustic effects during shock transmission. If the bubble acoustic impedance is higher than the ambient, the shock refraction pattern is convergent and leads to focusing of the transmitted shock onto the downstream pole. Shock focusing is associated with increase in pressure and temperature and can ignite a combustible gas mixture inside the bubble.

Shock-bubble interaction in reactive gases has been studied earlier mostly in the context of shock-flame interaction [115, 75]. Vorticity deposition by the shock results in enhanced mixing and combustion, followed by complex chemi-acoustic interactions. These interactions sustain turbulent reaction zones which can cause deflagration to detonation transition (DDT) in their vicinity[82]. Recently, experiments on reacting shock bubble interaction have been conducted by Haehn *et al.* [49] in the Wisconsin Shock-Tube Laboratory. The experiments demonstrated shock-initiated combustion of a H_2,O_2,Xe gas mixture inside a heavy spherical bubble surrounded by lighter N_2 gas. Shock-focusing due to the bubble creates a hot spot, thus igniting the mixture. A range of incident shock strengths were considered in the experiment and it was found that two different regimes exist. For low shock strengths $M \lesssim 2$, ignition is weak and the reaction proceeds slowly. For high shock strengths $M \gtrsim 2.5$, combustion is rapid, volumetric and can initiate even before the completion of shock-focusing.

Extensive two-dimensional computational studies by Diegelmann *et al* [25, 26] confirm the two regimes reported in the experiments. The computations find that ignition with weak shocks $2.0 \leq M \leq 2.3$ induces a subsonic deflagration wave, while strong shocks $M > 2.3$ lead to a supersonic detonation wave. For intermediate shock strength $M = 2.19$, the simulation exhibits DDT. The authors find that for a constant shock strength, increase in ambient pressure can change the reaction wave from deflagration

to detonation. The influence of the chemical reactions on the flow-field depends on the regime. They note that the dynamics of the detonated bubble differs significantly from an inert interaction, while the effect on the flow-field from deflagration combustion is weak.

Diegelmann *et al* [27] have also carried out a three-dimensional simulation of reacting shock bubble interaction (RSBI). The detonation case with $M = 2.83$ incident shock was considered. Azimuthal flow structures such as fine vortex filaments and Widnall-type instabilities [123] were observed on the axisymmetric vortex rings. The simulations slightly underpredicted the transverse bubble diameter post-detonation in comparison to the experiment. This was attributed to its sensitivity to the uncertainty in the location of ignition spot.

In this section, we present results from large eddy simulations (LES) of RSBI in the detonation regime [48]. LES enables low-resolution but stable computations of the shock-bubble interaction. The subgrid-scale (SGS) models account for the effect of unresolved small scales and are active during the initial interfacial roll-up and later in the primary vortex ring, the upstream secondary vortex ring[87] and the downstream supersonic vortex ring [124] regions. The flow field involves strong density variations due to shocks, combustion and turbulent mixing of inhomogeneous gases. Therefore, variable-density subgrid-scale terms require modeling. We solve Reynolds-filtered LES equations to compute filtered velocity, as opposed to Favre-filtered LES equations which compute the density-weighted filtered velocity. A new set of LES equations derived in Sidharth *et al.* [104] are used. Unlike the conventional Reynolds-filtered framework, the SGS terms in these equations do not involve time derivatives or third/fourth order correlations. Also, the effect of SGS mass flux, SGS dilatation and SGS pressure-gradient acceleration can be explicitly represented.

The objective of this work is two-fold: 1) to test the new LES equations on a complex yet canonical problem that involves compressible variable-density turbulence and 2) to understand the role of ignition spot location on intermediate time RSBI dynamics. We will see that within the detonation regime, for the same bubble gas mixture composition and the incident shock Mach number, depending on the bubble temperature, the detonation wave can originate either at the upstream pole or at the refracted-shock/bubble-interface point during shock-focusing. This can lead to significantly different flow and

mixing dynamics.

6.2.1 Subgrid-scale models

We specify the SGS models employed for closure. SGS specific stress and SGS fluxes of density, species mass fractions, internal energy are modeled with the Vreman eddy viscosity model [122]. The Vreman model has been demonstrated to perform well on transitional and turbulent shear layers. This is important for modeling of the small-scales present in SBI on the interface of the bubble after the shock transit. The eddy viscosity in Vreman model is computed as

$$\nu_e = 2.5 C_S^2 \Delta_c \sqrt{\frac{\mathbf{II}(G(u_i,u_j))}{\mathbf{I}(G(u_i,u_j))}} \quad \text{where} \quad G(a,b) = \frac{\Delta_c^2}{12}\frac{\partial \bar{a}}{\partial x_k}\frac{\partial \bar{b}}{\partial x_k} \tag{6.17}$$

Here $G(a,b)$ for two physical quantities a and b represents the gradient model [67] closure for $\mathcal{T}[a,b] = \overline{ab} - \bar{a}\bar{b}$. C_S is the Smagorinsky coefficient. $\mathbf{I}(A_{ij})$ and $\mathbf{II}(A_{ij})$ are the first and second invariants of any tensor A_{ij}. The SGS Prandtl number and SGS Schmidt number are taken to be 0.9 and 1.0 respectively. For SGS pressure-gradient acceleration and SGS dilatation correlations, we use the gradient model closure.

$$\mathcal{T}[\rho, \partial_i p/\rho] = \partial_i \bar{p}\mathcal{T}[\rho, 1/\rho] - \bar{\rho}\mathcal{T}[\partial_i p, 1/\rho] \overset{\text{m}}{=} \partial_i \bar{p}\; G(\rho, 1/\rho) - \bar{\rho}\; G(\partial_i p, 1/\rho) \tag{6.18}$$

$$\mathcal{T}[u_i, \partial_j u_j] \overset{\text{m}}{=} G[u_i, \partial_j u_j], \quad \mathcal{T}[p, \partial_j u_j] \overset{\text{m}}{=} G[p, \partial_j u_j] \tag{6.19}$$

We do not model the SGS mass fraction dilatation term, $\mathcal{T}[c_s, \partial_j u_j]$. In this work, we do not consider the SGS turbulent chemical source term $\bar{\Omega} - \Omega(\bar{E}_{\text{int}}, \bar{\rho}_s)$ and assume laminar finite rate chemistry. In the detonation regime of RSBI, combustion takes place inside the bubble before turbulent structures develop. Therefore, the SGS turbulent chemical source term is expected to be negligible during the detonation phase. For mass diffusion, we use an approximation by using a constant diffusion coefficient $\sigma_{\rho_s} = \partial_j(\bar{\rho} D \partial_j Y_s)$. Y_s is the mass fraction of species s and D is the diffusion coefficient obtained using constant Lewis number of 1.0. Ideally, a species diffusion coefficient matrix $D_{s1,s2}$ must be used as it is more accurate but the effect of accurate mass diffusion models on RSBI is not addressed in this work.

The chemical source term for species densities, $\dot{\omega}_s$ is evaluated as

$$\dot{\omega}_s = M_s \sum_{r=1}^{N_r} (\nu_{sr}^b - \nu_{sr}^f) \Gamma_s \Big(k_r^f \prod_{s'=1}^{N_s} [X_{s'}]^{\nu_{s'r}^f} - k_r^b \prod_{s'=1}^{N_s} [X_{s'}]^{\nu_{s'r}^b} \Big) \tag{6.20}$$

$[X_s]$ is the molar concentration of species s, M_s is its molecular weight. ν_{sr}^f, ν_{sr}^b is the molar stoichiometric coefficients of the forward/backward reaction for species s and reaction r. k_r^f, k_r^b are the reaction rates of reaction r. Γ_r is the third body efficiency of reaction r. The reaction rates are computed in the Arrhenius form with the reaction rate $k^f = AT^\eta \exp(-E_a/RT)$ where E_a is the activation energy, A is the pre-exponential factor, and η is the temperature exponent. All parameters are reaction specific. k^b is computed from the equilibrium constant of the reaction.

The reaction system in the simulation is hydrogen combustion. We are interested in the fast ignition regime that occurs above the 'crossover' temperature ($\sim$950K at 1 atm). In this regime, ignition occurs via chain branching explosion initiated by formation of HO_2 and H radicals. We model detailed chemical kinetics using Hong *et al* mechanism [54] with 8 species and 20 reactions. The 20 reactions may be grouped into four broad categories: hydrogen-oxygen shuffle reactions, hydroperoxyl reactions, radical-radical recombination reactions, and hydrogen-peroxide reactions. The mechanism provides improved rate constants for OH and HO_2 product reactions at high temperatures and has been shown to perform reliably at $T > 3000$K. The third body efficiency of Xe is set to be the same as that of Ar. We do not include the high pressure limit (Troe fall-off parameters) as the case considered in this work does not involves local pressures high enough to cause significant departures from the low-pressure limit parameters of the mechanism. In detonation, the induction time-scales are comparable or shorter than vibrational relaxation time scales for the shock leading the detonation. Therefore, vibrational relaxation effects can be important for accurate computation of thermochemical state and wave propagation velocities. However, for simplicity, we do not model vibrational relaxation of the species in the current work.

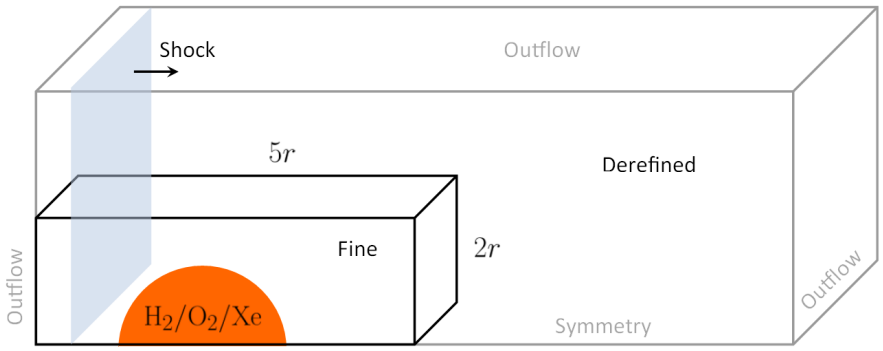

Figure 6.8: Computational setup for the shock-bubble interaction simulations

6.2.2 Computational setup

The computational setup based on the experiment [49] is shown in figure 6.8. A shock at Mach number of 2.83 is incident on a shock bubble with radius $r = 0.02$m in a frame of reference moving with 200m/s. Only a quarter of the bubble is simulated. The refined region of the domain is $5r \times 2r \times 2r$ with $r/\Delta = 80$. As seen from the figure, there is no derefined region upstream of the bubble. While this works well with upstream traveling shock waves, it is not effective for weak acoustic waves. However, since the numerical dissipation at the interface in the current simulations is high, this does not have a considerable effect on the interface development. The bubble gas mixture has a molar composition of H_2:O_2:Xe=1:2:3.75. The ambient gas is N_2. The density of the bubble is 3.28 kg/m^3. The Atwood number for the bubble corresponds to 0.5. The pre-shocked pressure p_0 and temperature T_0 are 1 atm and 295K respectively. The hydrodynamic time-scale based on shock-traversal time is 40 μ s. We also simulate a case where the pres-shocked p_0, T_0 are higher by a factor of 1.25. It will be seen in the next subsection that this changes the location of the ignition spot from downstream hemisphere to upstream pole, leading to a different kind of dynamics.

6.2.3 2D high resolution simulations

We carry out high resolution two-dimensional simulations as a preliminary exercise to understand the flow characteristics, time scales and sequence of events in the inert and reacting cases. An intermediate time snapshot of the flow-field is shown in figure 6.9.

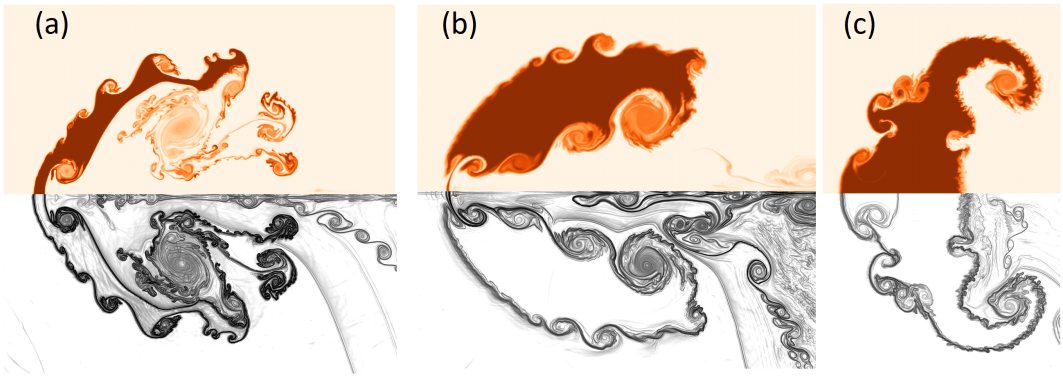

Figure 6.9: High resolution 2D simulations: Mass fraction of Xe (top) and log|$\nabla\rho$— (bottom) at inermediate time t=240 µs for (a) inert, (b) reacting case (p_0 = 1 atm) and (c) reacting case (p_0 = 1.25 atm)

Case (a) is the inert case, while cases (b) and (c) correspond to the reacting cases. The difference between cases (b) and (c) is that ambient pressure and temperature is higher. In case (b), detonation occurs at the refracted shock/interface point during shock transit. This results in detonation right when the incident shock hits the bubble. It is important to note that it is the increase in initial bubble temperature at this composition and shock Mach number that shifts the ignition spot. This was independently confirmed by keeping the ambient pressure at p_0 and increasing the bubble temperature.

Detailed evolution of the interaction including the detonation wave is visualized in [25, 26]. Dynamics in case (c) here resembles the $M = 2.9$ condition considered in [26]. It is seen that the interface development in case (c) is Richtmyer-Meshkov/Rayleigh-Taylor type while primary interface instability in case (b) is Kelvin-Helmholtz type. In general, the primary difference between inert and reacting cases is the reduced mixing between bubble and ambient fluid in the reacting cases. Unlike the inert case which has two main vortices, case (b) has multiple vortices on the lower interface.

The case (b) flow-field is explicitly filtered to estimate the importance of variable-density SGS terms in the Reynolds-filtered momentum equation. Using an exponential filter with filter $\Delta_c = 5\Delta$, we compute the magnitude of the individual SGS terms in $\mathcal{S}_{\rho u_i}$ and plot them in figure 6.10. It is seen that variable-density SGS terms (ii-iv) are active and non-negligible. Although this is a two-dimensional flow-field, it is expected

that the terms will actively contribute in 3D LES where the models are active in an *a posteriori* sense.

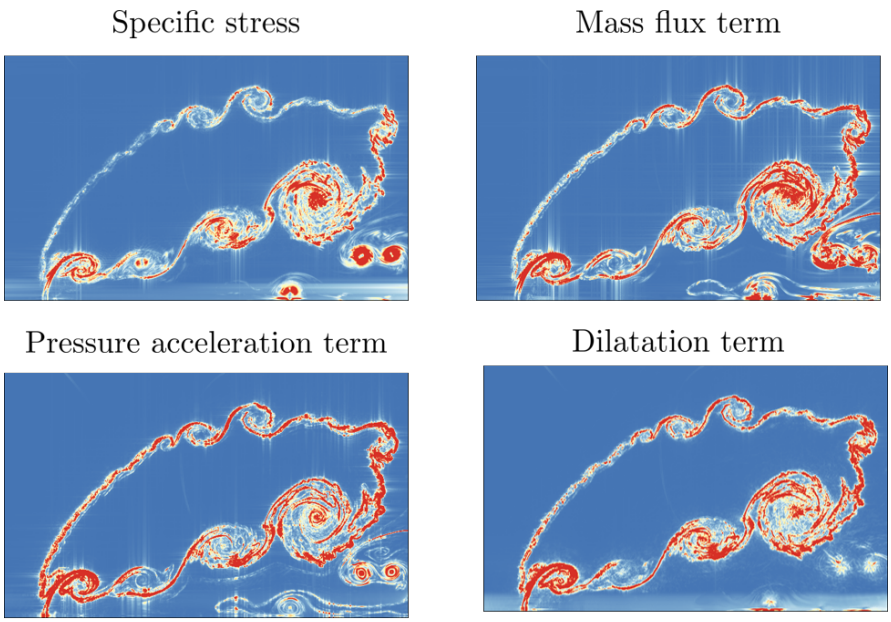

Figure 6.10: *A priori* estimate of magnitude of SGS terms in the Reynolds-filtered momentum equation for case (b): (i) SGS specific stress term, (ii) SGS mass flux convection, (iii) SGS pressure-gradient acceleration term, and (iv) SGS velocity dilatation term. An exponential filter with $\Delta_c = 5\Delta$ is used. All quantities are plotted on the same scale.

6.2.4 Large eddy simulation results

The results from large eddy simulations from the inert (case a) and reacting (cases b and c) interactions are presented in this section. Case (c) is simulated to study the dynamics with higher bubble temperature. However, to keep the Atwood number of the interaction fixed, the initial temperature of both the bubble and the ambient is increased to 372K.

Similar to the two-dimensional results, the spatio-temporal evolution of the reacting cases exhibit differences from the inert case. This is reflected not only in the bubble

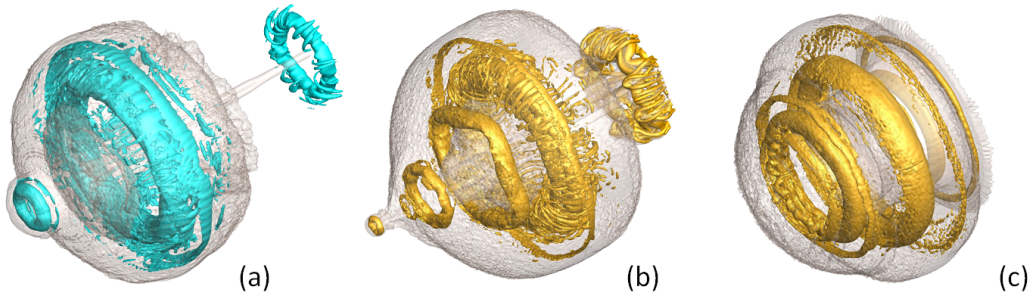

Figure 6.11: Large eddy simulation results of (a) inert, (b) reacting case T_0 and (c) reacting case $1.25T_0$: isosurfaces of Q criterion (different values for the three cases) and $Y_{\mathrm{Xe}} = 10^{-3}$ at $t^* = 5$

size due to volumetric expansion, but also the vortex ring system development at the intermediate stage. Figure 6.11 visualizes the vortex structures in the flow-field at $t =$ 200 µs or $t^* = 5$. The inert case has a stronger shear layer at the interface and shows the three main vortex ring systems: primary (middle), secondary (front) and the supersonic ring (rear). The primary vortex ring and its interaction with the interfacial vortex sheet results in small-scale vortex filaments. These kind of three-dimensional structures affect the ring evolution and cannot be captured by two-dimensional simulations. The reacting case (b), in contrast contains multiple vortex ring systems, albeit weaker in intensity. The primary vortex ring and the downstream rings have significant small-scale filaments. The secondary rings in the front display presence of azimuthal deformations, some of which are a consequence of symmetry boundary conditions and non-isotropic nature of the numerics. The hot bubble reacting case (c) has a different morphology from (a) and (b). The most striking difference is the absence of streamwise projectile structures in the front and the back of the bubble. The rear supersonic ring is extremely weak and does not show up in the figure. There are three large diameter rings with nearly no azimuthal small-scale filaments. Some weak three-dimensionality on the interfacial shear layer and Widnall-type instability on rings is observed.

In both reacting cases, with $M = 2.83$ incident shock, combustion takes place before vortex ring development. This is seen in the figure 6.12. The origin of detonation wave can be seen to shift from downstream hemisphere (case b) to upstream pole (case c) with

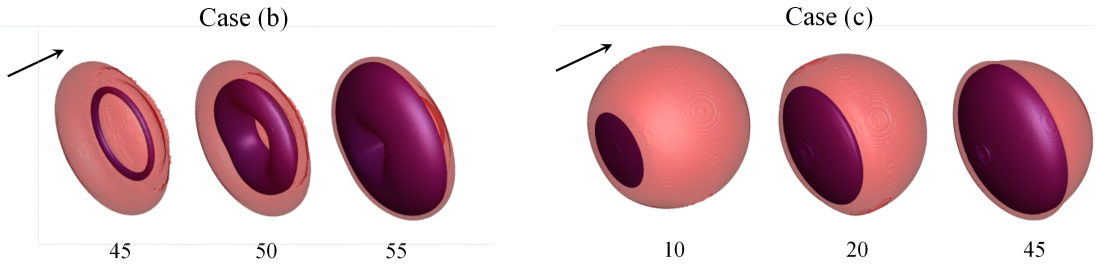

Figure 6.12: Visualization of the detonation waves inside the compressed bubble (translucent) using T isosurface values in reacting cases (b) and (c). The numbers indicate the time in µs.

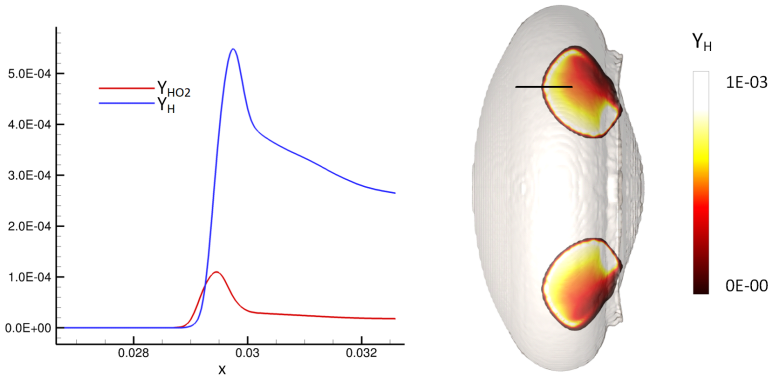

Figure 6.13: Mass fraction profiles of H and HO2 across the detonation wave in case (b) at t=50 µs.

higher initial bubble temperature. We also visualize the profiles of hydroperoxyl and hydrogen radicals across the detonation wave (figure 6.13). Qualitatively, the trends of radical profiles are similar to those observed in a Chapman-Jouguet detonation in stoichiometric H_2/Air [96] except the peak in mass fraction profile of H is much higher than that of HO2.

The evolution of the transverse bubble width (TW) is compared with the experiment in figure 6.14. Case (b) corresponds to the experimental conditions. Although the expansion rate in the post-detonation phase is captured correctly, the peak TW values are underpredicted similar to the high resolution 3D simulations in [27]. This can be attributed to the experimental uncertainty in the ignition spot on account of thermal/compositional fluctuations in the bubble. It is also interesting to observe that expansion rate in case (c) is much slower and the peak TW is reached at much later time. Therefore, the large scatter in the experimental data around $t^* = 6$ may potentially be explained by different ignition locations in different runs.

We also comment on the chemiluminescence images observed in the experiment. The signals from the experiment indicate presence of two bright spots inside the bubble, the explanation for which is not clear. From current simulations, we observe, in both reacting cases, two local OH maxima (figure 6.15). It is possible that the bright spots in OH chemiluminescence correspond to those local maxima. Since the exposure times in the experiment are long and the OH maxima are found to exist in the simulations for some time post-combustion, the hypothesis is consistent.

The activity of SGS terms in the simulation, particularly the variable-density SGS terms is of interest. In the initial phases of the interaction, the SGS terms are active only in the shear layer deposited by the shock and at the bubble poles where there are sharp gradients in the flow quantities. Later as three-dimensional instabilities and small-scale structures develop on the vortex ring systems and the center line jet (cases a and b), the SGS terms become active. To determine the size of the modeled variable-density SGS terms in comparison to the constant density SGS term in the Reynolds-filtered momentum equation, we plot the regularized ratio of the SGS vector projection on $\bar{u}_i$. This scalar metric is relevant as it represents the contribution of the SGS terms to resolved-scale kinetic energy. Figure 6.17 reveals that the modeled variable-density SGS terms are large and surpass the contribution of the SGS specific stress terms in

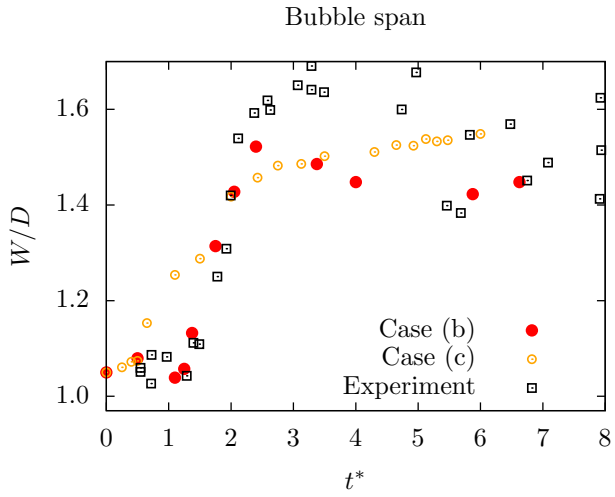

Figure 6.14: Comparison of the time evolution of the radial extent of the bubble with experiment.

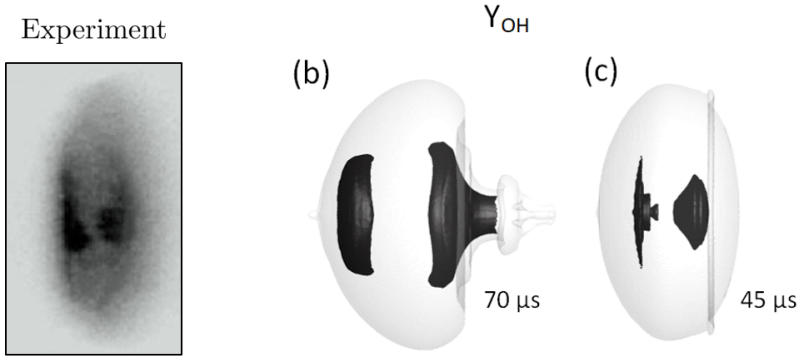

Figure 6.15: Presence of two OH peaks at different poles of the bubble: (b) and (c) denote the two different simulation cases.

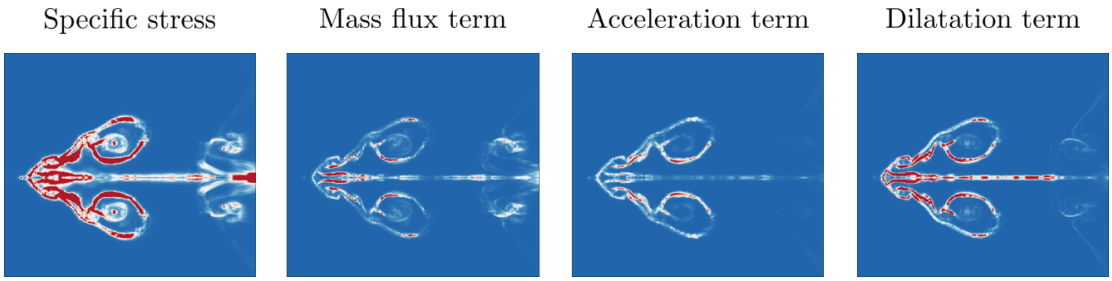

Figure 6.16: A slice visualization of modeled variable density SGS terms at $t = 240$ µs, plotted on the same colormap.

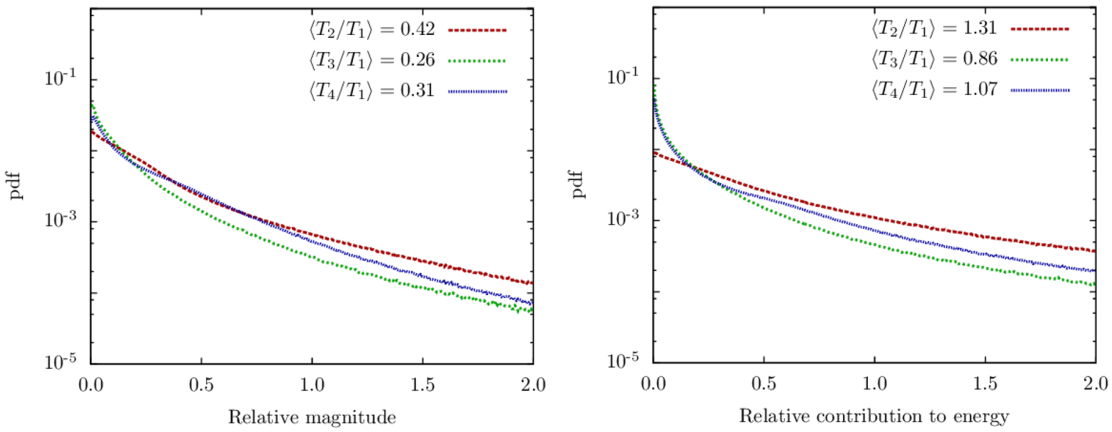

Figure 6.17: Pdfs associated with relative size of modeled variable-density SGS terms in intermediate stage of the interaction.

certain regions in the domain. This has implications for modeling of variable-density SGS effects in LES of high speed combustion.

The section presents results from Reynolds-filtered large eddy simulations of reacting shock-bubble interaction. A strong interaction with $M = 2.83$ incident shock is considered. The flow dynamics is complex involving baroclinic vorticity deposition, detonation, volumetric expansion, chemi-acoustic interactions and quasi-turbulent mixing. This work demonstrates that the new set of Reynolds-filtered velocity equations can simulate complex variable-density flow-dynamics. The equations takes into account the dilatational and inertial effects at subgrid-scales. In particular, the effect of SGS mass flux, SGS pressure-gradient acceleration, and SGS velocity-dilatation is explicitly modeled. This is important from the point of view of resolved-scale vorticity transport as the curl of SGS pressure-gradient acceleration is the SGS baroclinic torque.

The results from the simulation compare well with the experiment in terms of the time evolution of the transverse bubble width. In our study, we find that the ignition point of detonation can move from the downstream hemisphere to the upstream pole as the initial temperature of the bubble gas is increased. This changes the interaction dynamics significantly, resulting in a different kind of vortex ring system and transverse width evolution. Therefore, thermal fluctuation content in the bubble is an important parameter for uncertainty quantification of the RSBI analysis. In the future, high resolution simulations with accurate mass diffusion and vibrational relaxation models will help make predictive quantification of the flow and the thermo-chemical state in different stages of the interaction.

6.3 Conclusions

In this chapter, we carried out large-eddy simulations of compressible reacting flows to apply and test the Reynolds-filtered governing equations for numerical computation. Two flow cases are simulated: (a) a reattaching shear layer, and (b) reacting shock-bubble interaction. The first case involves non-premixed H_2-F_2 combustion and the second, premixed H_2-O_2 combustion. The SGS fields are modeled as follows: the SGS specific stress and SGS scalar fluxes are modeled from incompressible flow literature, while SGS pressure acceleration and SGS dilatation terms are closed with gradient

models. In the shear layer case, SGS mass flux is found to be dynamically active. The term affects the transport of large-scale momentum and species mass significantly. The role of SGS mass flux and its closure requires further understanding in the context of mixing and turbulence statistics. In the reacting shock bubble interaction, the flow becomes multi-scale and near-turbulent only in its late stages. All modeled variable-density SGS terms in the momentum equation are found to be equally as important as the SGS specific stress. Although the equations are successfully applied to a transitional flow, the relative contribution of the SGS terms and numerical dissipation in the presence of a non-turbulent sharp scalar interface requires a careful analysis to avoid aphysical interface evolution.

Chapter 7

Summary and conclusions

The thesis provides a framework to analyze the effects of small-scale spatial density variations on the dynamics of large-scale velocity fields in multi-scale and fully turbulent flows.

The effect of density variations in locally homogeneous turbulence is demonstrated by considering the variable-density Karman-Howarth-Monin equation which describes the evolution of the second order velocity structure function. The dissipation of specific energy includes terms involving dilatation and spatial gradient of density in addition to the flux in scale space.

The role of subgrid-scale density fluctuations on resolved-scale velocity is analyzed using both density-weighted and non-density-weighted forms of the filtered governing equations. First, we discuss the conventional Favre-filtered framework and then follow with the derivation of a novel Reynolds-filtered form of the equations. The Reynolds-filtered velocity dynamics are emphasized because the curl of the filtered velocity is the filtered vorticity, as opposed to the curl of Favre-filtered velocity, which is a density convolved vorticity variable. SGS baroclinic torque appears in the transport equation of filtered vorticity, but is absent in the Favre-filtered case.

The conventional Reynolds-filtered momentum equation contains the time derivative of the SGS mass flux. This unsteady SGS term makes the equation cumbersome from a modeling perspective. Therefore, the new Reynolds-filtered equations for mass, momentum, and energy are derived by decoupling the transport of SGS mass flux and

SGS kinetic energy. The new Reynolds-filtered equations involve only double correlations of the flow variables and do not contain any time derivative of SGS term. The terms involving SGS density and dilatation fields appear explicitly, independent of the SGS specific stress.

Next, we build a qualitative understanding of variable-density effects in physical space using the vorticity field associated with Lundgren's stretched-vortex model for turbulent fine structures [73]. A initial distribution of variable density regions in the vortex plane is found to produce more small-scale enstrophy than the near-incompressible case. The 3D energy spectrum computed from the model vorticity field shows that the baroclinic vorticity production results in higher energy in the -5/3 subrange. For subgrid modeling using the stretched-vortex model [79], this would imply an increase in the $k^{-5/3}$ spectrum pre-factor but not its slope. Since the pre-factor in the SGS model is computed by structure-function matching with the filtered velocity field [119], the SGS specific stress model does not require any modification in the presence of subgrid density variations. Consistency of the prefactor with the supergrid velocity field automatically takes care of the increased energy content. This consistency is however contingent on the solution variable being the Reynolds-filtered velocity. In the case of Favre-filtered velocity, the structure function matching procedure as presented in Voelkl et al. [119] does not directly hold.

We quantify the variable-density SGS terms in the filtered governing equations using fields from direct numerical simulations. An exponential filter in the inertial-viscous region of the energy spectrum is applied to obtain the filtered and the subgrid-scale quantities. Direct numerical simulations of low Reynolds number turbulent mixing are carried out, in which baroclinic torque plays an important role in the vorticity dynamics. Two flow cases are considered: turbulent mixing of isotropically distributed variable-temperature fluids and turbulent mixing of a reshocked heavy gas layer. In the first case, the baroclinic torque primarily arises from pressure fluctuations of turbulent eddies, while in the second case, it is associated with the pressure jump across the traversing normal shock. Later, as the flow evolves, vorticity is also generated by acoustic waves interacting with density variations during the mixing process. In both cases, variable-density SGS terms in the momentum equation are found to be locally large and comparable to the SGS specific stress term. In compressible decaying turbulent flows

upto turbulent Mach number of 0.3 however, SGS variable-density terms are negligible. Therefore, SGS modeling in the presence of strong density variations associated with material/temperature variation in the fluid and additionally in the presence of chemical reactions, is different from the case where density fluctuations occur primarily due to compressibility of fluid motion.

To test the robustness and accuracy of the new Reynolds-filtered equation set in numerical computations, large eddy simulations of compressible reacting flows are carried out. Taylor series expansion based gradient model is used for SGS acceleration and SGS dilatation closures, while conventional closures for SGS specific stress and SGS scalar fluxes are employed from the literature. For the reacting shear layer in an expansion ramp configuration, SGS mass flux is found to be an important term affecting the momentum and the species mass equations. Separately, in reacting shock bubble interaction, when the interaction becomes chaotic and multi-scale at late stages, all variable-density SGS terms are found to be active and equally important as the SGS specific stress.

The research work leading to this thesis provides an effective modeling framework for physical representation of small-scale effects in high Reynolds number variable-density turbulent flows, commonly encountered in aerodynamics and propulsion for high speed flight. Future work will involve the use of Reynolds-filtered compressible Navier-Stokes equations to solve for the time-averaged turbulent flow-fields, and their extension to turbulent boundary layers with consistent wall-modeling techniques.

References

[1] V Adumitroaie, J. R. Ristorcelli, and D. B. Taulbee. Progress in Favre-Reynolds stress closures for compressible flows. *Physics of Fluids*, 11(9):2696–2719, 1999.

[2] Hussein Aluie. Compressible turbulence: the cascade and its locality. *Physical review letters*, 106(17):174502, 2011.

[3] J Bakosi and JR Ristorcelli. Extending the langevin model to variable-density pressure-gradient-driven turbulence. *Journal of Turbulence*, 12, 2011.

[4] BJ Balakumar, GC Orlicz, CD Tomkins, and KP Prestridge. Simultaneous particle-image velocimetry–planar laser-induced fluorescence measurements of richtmyer–meshkov instability growth in a gas curtain with and without reshock. *Physics of Fluids*, 20(12):124103, 2008.

[5] Arindam Banerjee, Robert A Gore, and Malcolm J Andrews. Development and validation of a turbulent-mix model for variable-density and compressible flows. *Physical Review E*, 82(4):046309, 2010.

[6] RW Bilger. Turbulent jet diffusion flames. *Progress in Energy and Combustion Science*, 1(2-3):87–109, 1976.

[7] B. J. Boersma and S. K. Lele. Large eddy simulation of compressible turbulent jets. *Center for Turbulence Research Annual Research Briefs*, pages 365–377, 1999.

[8] Aristides M Bonanos, Jeffrey M Bergthorson, and Paul E Dimotakis. Mixing measurements in a supersonic expansion-ramp combustor. *Flow, Turbulence and Combustion*, 80(4):489–506, 2008.

[9] KNC Bray, Paul A Libby, Goro Masuya, and JB Moss. Turbulence production in premixed turbulent flames. *Combustion Science and Technology*, 25, 1981.

[10] Howard Brenner. Bi-velocity hydrodynamics. *Physica A: Statistical Mechanics and its Applications*, 388(17):3391–3398, 2009.

[11] Martin Brouillette. The Richtmyer-Meshkov instability. *Annual Review of Fluid Mechanics*, 34(1):445–468, 2002.

[12] Garry L Brown and Anatol Roshko. On density effects and large structure in turbulent mixing layers. *Journal of Fluid Mechanics*, 64(4):775–816, 1974.

[13] Graham V Candler, Pramod K Subbareddy, and Joseph M Brock. Advances in computational fluid dynamics methods for hypersonic flows. *Journal of Spacecraft and Rockets*, 2015.

[14] Graham V Candler, Pramod K Subbareddy, and Ioannis Nompelis. Cfd methods for hypersonic flows and aerothermodynamics. *Hypersonic Nonequilibrium Flows: Fundamentals and Recent Advances*, pages 203–237, 2015.

[15] Nilanjan Chakraborty, Lipo Wang, Ilias Konstantinou, and Markus Klein. Vorticity statistics based on velocity and density-weighted velocity in premixed reactive turbulence. *Journal of Turbulence*, 18(9):825–853, 2017.

[16] P Chassaing. Some problems on single point modeling of turbulent, low-speed, variable density fluid motions. In *IUTAM Symposium on Variable Density Low-Speed Turbulent Flows*, pages 65–84. Springer, 1997.

[17] P. Chassaing, G. Harran, and L. Joly. Density fluctuation correlations in free turbulent binary mixing. *Journal of Fluid Mechanics*, 279:239–278, 11 1994. ISSN 1469-7645.

[18] Patrick Chassaing. The modeling of variable density turbulent flows. a review of first-order closure schemes. *Flow, turbulence and combustion*, 66(4):293–332, 2001.

[19] Patrick Chassaing, RA Antonia, Fabien Anselmet, L Joly, and S Sarkar. *Variable density fluid turbulence*. Springer Science & Business Media, 2013.

[20] Jeremy Chesnel, Julien Reveillon, Thibaut Menard, and Francois-Xavier Demoulin. Large eddy simulation of liquid jet atomization. *Atomization and Sprays*, 21(9), 2011.

[21] Stephen Childress. A vortex-tube model of eddies in the inertial range. *Geophysical & Astrophysical Fluid Dynamics*, 29(1-4):29–64, 1984.

[22] J Chomiak and JR Nisbet. Modeling variable density effects in turbulent flames: some basic considerations. *Combustion and flame*, 102(3):371–386, 1995.

[23] D Chung and DI Pullin. Large-eddy simulation and wall modelling of turbulent channel flow. *Journal of fluid mechanics*, 631:281–309, 2009.

[24] BD Collins and JW Jacobs. Plif flow visualization and measurements of the richtmyer–meshkov instability of an air/sf 6 interface. *Journal of Fluid Mechanics*, 464:113–136, 2002.

[25] Felix Diegelmann, Stefan Hickel, and Nikolaus A Adams. Shock mach number influence on reaction wave types and mixing in reactive shock–bubble interaction. *Combustion and Flame*, 174:85–99, 2016.

[26] Felix Diegelmann, Volker Tritschler, Stefan Hickel, and Nikolaus Adams. On the pressure dependence of ignition and mixing in two-dimensional reactive shock-bubble interaction. *Combustion and Flame*, 163:414–426, 2016.

[27] Felix Diegelmann, Stefan Hickel, and Nikolaus A Adams. Three-dimensional reacting shock–bubble interaction. *Combustion and Flame*, 181:300–314, 2017.

[28] Diego A Donzis, KR Sreenivasan, and PK Yeung. The batchelor spectrum for mixing of passive scalars in isotropic turbulence. *Flow, turbulence and combustion*, 85(3):549–566, 2010.

[29] Gregory L Eyink. Locality of turbulent cascades. *Physica D: Nonlinear Phenomena*, 207(1-2):91–116, 2005.

[30] Gregory L Eyink and Theodore D Drivas. Cascades and dissipative anomalies in compressible fluid turbulence. *Physical Review X*, 8(1):011022, 2018.

[31] Gregory Falkovich, Itzhak Fouxon, and Yaron Oz. New relations for correlation functions in navier–stokes turbulence. *Journal of Fluid Mechanics*, 644:465–472, 2010.

[32] A Favre. Statistical equations of turbulent gases. *Problems of hydrodynamics and continuum mechanics*, pages 231–266, 1969.

[33] Alexandre JA Favre. Formulation of the statistical equations of turbulent flows with variable density. In *Studies in Turbulence*, pages 324–341. Springer, 1992.

[34] Pedro José Martínez Ferrer, Guillaume Lehnasch, and Arnaud Mura. Compressibility and heat release effects in high-speed reactive mixing layers i.: Growth rates and turbulence characteristics. *Combustion and Flame*, 180:284–303, 2017.

[35] Jerome Fontane and Laurent Joly. The stability of the variable-density Kelvin-Helmholtz billow. *Journal of Fluid Mechanics*, 612:237–260, 2008.

[36] Jonathan B Freund, Sanjiva K Lele, and Parviz Moin. Compressibility effects in a turbulent annular mixing layer. part 1. turbulence and growth rate. *Journal of Fluid Mechanics*, 421:229–267, 2000.

[37] CE Frieler and PE Dimotakis. Mixing and reaction at low heat release in the non-homogeneous shear layer. *First National Fluid Dynamics Congress*, 1988.

[38] Sébastien Galtier and Supratik Banerjee. Exact relation for correlation functions in compressible isothermal turbulence. *Physical review letters*, 107(13):134501, 2011.

[39] M. Germano. Turbulence: the filtering approach. *Journal of Fluid Mechanics*, 238:325–336, 5 1992. ISSN 1469-7645. URL `http://journals.cambridge.org/article_S0022112092001733`.

[40] M. Germano. Averaging procedures for the large eddy simulation of variable density flows. *IUTAM Symposium on Variable Density Low-Speed Turbulent Flows*, pages 101–108, 1996.

[41] M Germano. A direct relation between the filtered subgrid stress and the second order structure function. *Physics of Fluids*, 19(3):038102, 2007.

[42] M. Germano, A. Abb, R. Arina, and L. Bonaventura. On the extension of the eddy viscosity model to compressible flows. *Physics of Fluids*, 26(4):041702, 2014.

[43] Daniel R Getsinger, Cory Hendrickson, and Ann R Karagozian. Shear layer instabilities in low-density transverse jets. *Experiments in fluids*, 53(3):783–801, 2012.

[44] AE Gill, JSA Green, and AJ Simmons. Energy partition in the large-scale ocean circulation and the production of mid-ocean eddies. In *Deep Sea Research and Oceanographic Abstracts*, volume 21, pages 499IN1509–508528. Elsevier, 1974.

[45] Th Gomez, H Politano, A Pouquet, and M Larchevêque. Spiral vortices in compressible turbulent flows. *Physics of Fluids*, 13(7):2065–2075, 2001.

[46] Sigal Gottlieb, Chi-Wang Shu, and Eitan Tadmor. Strong stability-preserving high-order time discretization methods. *SIAM review*, 43(1):89–112, 2001.

[47] Igor A Grigoriev, Stefan Wallin, Geert Brethouwer, and Arne V Johansson. Capturing turbulent density flux effects in variable density flow by an explicit algebraic model. *Physics of Fluids*, 27(4):045108, 2015.

[48] Sidharth GS and G Candler. Large eddy simulation of reacting shock bubble interaction. *TRR40 Summer Research Program Report*, (4), 2017.

[49] Nicholas Haehn, Devesh Ranjan, Chris Weber, Jason Oakley, David Rothamer, and Riccardo Bonazza. Reacting shock bubble interaction. *Combustion and Flame*, 159(3):1339–1350, 2012.

[50] Fujihiro Hamba. Effects of pressure fluctuations on turbulence growth in compressible homogeneous shear flow. *Physics of Fluids*, 11(6):1623–1635, 1999. URL `http://scitation.aip.org/content/aip/journal/pof2/11/6/10.1063/1.870023`.

[51] JC Hermanson and PE Dimotakis. Effects of heat release in a turbulent, reacting shear layer. *Journal of Fluid Mechanics*, 199:333–375, 1989.

[52] DJ Hill, C Pantano, and DI Pullin. Large-eddy simulation and multiscale modelling of a richtmyer–meshkov instability with reshock. *Journal of fluid mechanics*, 557:29–61, 2006.

[53] Reginald J Hill. Applicability of kolmogorov's and monin's equations of turbulence. *Journal of Fluid Mechanics*, 353:67–81, 1997.

[54] Zekai Hong, David F Davidson, and Ronald K Hanson. An improved h 2/o 2 mechanism based on recent shock tube/laser absorption measurements. *Combustion and Flame*, 158(4):633–644, 2011.

[55] Kiyosi Horiuti and Takeharu Fujisawa. The multi-mode stretched spiral vortex in homogeneous isotropic turbulence. *Journal of Fluid Mechanics*, 595:341–366, 2008.

[56] Laurent Joly, Jérôme Fontane, and Patrick Chassaing. The Rayleigh-Taylor instability of two-dimensional high-density vortices. *Journal of Fluid Mechanics*, 537: 415–431, 2005.

[57] Peter Kaps and Peter Rentrop. Generalized runge-kutta methods of order four with stepsize control for stiff ordinary differential equations. *Numerische Mathematik*, 33(1):55–68, 1979.

[58] Anand Kartha, Pramod K Subbareddy, Graham V Candler, and Paul Dimotakis. Large-eddy simulation of supersonic reacting mixing layers. In *44th AIAA Fluid Dynamics Conference*, number 3030, 2014.

[59] Anand Kartha, Pramod K Subbareddy, Graham V Candler, and Paul Dimotakis. Les of reacting mixing layers: Species concentration boundedness and inflow conditions. In *22nd AIAA Computational Fluid Dynamics Conference*, number 3207, 2015.

[60] M Klein, C Kasten, Y Gao, and N Chakraborty. A-priori direct numerical simulation assessment of sub-grid scale stress tensor closures for turbulent premixed combustion. *Computers & Fluids*, 122:1–11, 2015.

[61] Leslie SG Kovasznay. Turbulence in supersonic flow. *Journal of the Aeronautical Sciences*, 20(10), 1953.

[62] Johannes Kreuzinger, Rainer Friedrich, and Thomas B. Gatski. Compressibility effects in the solenoidal dissipation rate equation: A priori assessment and modeling. *International Journal of Heat and Fluid Flow*, 27(4):696 – 706, 2006.

[63] Maher Lagha, John Kim, JD Eldredge, and Xiaolin Zhong. A numerical study of compressible turbulent boundary layers. *Physics of fluids*, 23(1):015106, 2011.

[64] Chris CK Lai, John J Charonko, and Katherine Prestridge. A kármán–howarth–monin equation for variable-density turbulence. *Journal of Fluid Mechanics*, 843: 382–418, 2018.

[65] John C LaRue and Paul A Libby. Measurements in the turbulent boundary layer with slot injection of helium. *The Physics of Fluids*, 20(2):192–202, 1977.

[66] Sanjiva K Lele. Compressibility effects on turbulence. *Annual review of fluid mechanics*, 26(1):211–254, 1994.

[67] A Leonard. Energy cascade in large-eddy simulations of turbulent fluid flows. *Advances in geophysics*, 18:237–248, 1975.

[68] Paul A Libby and KNC Bray. Variable density effects in premixed turbulent flames. *AIAA J*, 15(8):1186–1193, 1977.

[69] Paul A Libby and KNC Bray. Countergradient diffusion in premixed turbulent flames. *AIAA Journal*, 19(2), 1981.

[70] RP Lindstedt and EM Vaos. Modeling of premixed turbulent flames with second moment methods. *Combustion and Flame*, 116(4):461–485, 1999.

[71] AN Lipatnikov and Jerzy Chomiak. Effects of premixed flames on turbulence and turbulent scalar transport. *Progress in Energy and Combustion Science*, 36(1): 1–102, 2010.

[72] Daniel Livescu and JR Ristorcelli. Buoyancy-driven variable-density turbulence. *Journal of Fluid Mechanics*, 591:43–71, 2007.

[73] TS Lundgren. Strained spiral vortex model for turbulent fine structure. *The Physics of Fluids*, 25(12):2193–2203, 1982.

[74] TS Lundgren. A small-scale turbulence model. *Physics of Fluids A: Fluid Dynamics*, 5(6):1472–1483, 1993.

[75] George H Markstein. *Nonsteady flame propagation: AGARDograph*, volume 75. Elsevier, 2014.

[76] G Matheou and D Chung. Direct numerical simulation of stratified turbulence. *Physics of Fluids*, 24(9):091106, 2012.

[77] Georgios Matheou, Aristides M Bonanos, Carlos Pantano, and Paul E Dimotakis. Large-eddy simulation of mixing in a recirculating shear flow. *Journal of Fluid Mechanics*, 646:375–414, 2010.

[78] MF Miller, CT Bowman, and MG Mungal. An experimental investigation of the effects of compressibility on a turbulent reacting mixing layer. *Journal of Fluid Mechanics*, 356:25–64, 1998.

[79] Ashish Misra and Dale I Pullin. A vortex-based subgrid stress model for large-eddy simulation. *Physics of Fluids*, 9(8):2443–2454, 1997.

[80] AS Monin. The theory of locally isotropic turbulence. In *Soviet Physics Doklady*, volume 4, page 271, 1959.

[81] Peter A Monkewitz, Dietrich W Bechert, Bernd Barsikow, and Bernhard Lehmann. Self-excited oscillations and mixing in a heated round jet. *Journal of Fluid Mechanics*, 213:611–639, 1990.

[82] Elaine S Oran and Vadim N Gamezo. Origins of the deflagration-to-detonation transition in gas-phase combustion. *Combustion and Flame*, 148(1):4–47, 2007.

[83] C Pantano and S Sarkar. A study of compressibility effects in the high-speed turbulent shear layer using direct simulation. *Journal of Fluid Mechanics*, 451: 329–371, 2002.

[84] Ashish Patel, Bendiks J Boersma, and Rene Pecnik. The influence of near-wall density and viscosity gradients on turbulence in channel flows. *Journal of Fluid Mechanics*, 809:793–820, 2016.

[85] RT Pierrehumbert and KL Swanson. Baroclinic instability. *Annual review of fluid mechanics*, 27(1):419–467, 1995.

[86] Katherine Prestridge, Gregory Orlicz, Sridhar Balasubramanian, and BJ Balakumar. Experiments of the richtmyer–meshkov instability. *Phil. Trans. R. Soc. A*, 371(2003):20120165, 2013.

[87] Devesh Ranjan, Mark Anderson, Jason Oakley, and Riccardo Bonazza. Experimental investigation of a strongly shocked gas bubble. *Physical review letters*, 94 (18):184507, 2005.

[88] Devesh Ranjan, Jason Oakley, and Riccardo Bonazza. Shock-bubble interactions. *Annual Review of Fluid Mechanics*, 43:117–140, 2011.

[89] Jean Reinaud, Laurent Joly, and Patrick Chassaing. The baroclinic secondary instability of the two-dimensional shear layer. *Physics of Fluids*, 12(10):2489–2505, 2000.

[90] J Raymond Ristorcelli and Gregory A Blaisdell. Consistent initial conditions for the dns of compressible turbulence. *Physics of Fluids*, 9(1):4–6, 1997.

[91] JR Ristorcelli. A representation for the turbulent mass flux contribution to reynolds-stress and two-equation closures for compressible turbulence. *ICASE Report*, (93-88), 1993.

[92] Vincent Robin, Arnaud Mura, and Michel Champion. Direct and indirect thermal expansion effects in turbulent premixed flames. *Journal of Fluid Mechanics*, 689: 149–182, 2011.

[93] Robert Rubinstein and Gordon Erlebacher. Transport coefficients in weakly compressible turbulence. *Physics of Fluids*, 9(10):3037–3057, 1997. URL `http://scitation.aip.org/content/aip/journal/pof2/9/10/10.1063/1.869413`.

[94] Vladimir A Sabelnikov and Andrei N Lipatnikov. Recent advances in understanding of thermal expansion effects in premixed turbulent flames. *Annual Review of Fluid Mechanics*, 49:91–117, 2017.

[95] Ravi Samtaney, Dale I Pullin, and Branko Kosović. Direct numerical simulation of decaying compressible turbulence and shocklet statistics. *Physics of Fluids*, 13 (5):1415–1430, 2001.

[96] Antonio L Sánchez and Forman A Williams. Recent advances in understanding of flammability characteristics of hydrogen. *Progress in energy and combustion science*, 41:1–55, 2014.

[97] Donald Leon Sandoval. *The dynamics of variable-density turbulence*. PhD thesis, 1995.

[98] S Sarkar. The pressure–dilatation correlation in compressible flows. *Physics of Fluids A: Fluid Dynamics*, 4(12):2674–2682, 1992.

[99] Jörg Schumacher, Janet D Scheel, Dmitry Krasnov, Diego A Donzis, Victor Yakhot, and Katepalli R Sreenivasan. Small-scale universality in fluid turbulence. *Proceedings of the National Academy of Sciences*, 111(30):10961–10965, 2014.

[100] John D. Schwarzkopf, Daniel Livescu, Robert A. Gore, Rick M. Rauenzahn, and J. Raymond Ristorcelli. Application of a second-moment closure model to mixing processes involving multicomponent miscible fluids. *Journal of Turbulence*, 12: N49, 2011.

[101] Sylvain Serra, Vincent Robin, Arnaud Mura, and Michel Champion. Density variations effects in turbulent diffusion flames: modeling of unresolved fluxes. *Combustion Science and Technology*, 186(10-11):1370–1391, 2014.

[102] Tsan-Hsing Shih, John L. Lumley, and J. Janicka. Second-order modelling of a variable-density mixing layer. *Journal of Fluid Mechanics*, 180:93–116, 7 1987. ISSN 1469-7645.

[103] GS Sidharth, G. V. Candler, and P. E. Dimotakis. Baroclinic torque and implications for subgrid-scale modeling. *7th AIAA Theoretical Fluid Mechanics Conference*, (3214), 2014.

[104] GS Sidharth, Anand Kartha, and Graham V Candler. Filtered velocity based les of mixing in high speed recirculating shear flow. *46$^{\text{th}}$ AIAA Fluid Dynamics Conference*, (3184), 2016.

[105] Krishnendu Sinha and Graham V Candler. Turbulent dissipation-rate equation for compressible flows. *AIAA Journal*, 41(6):1017–1021, 2003.

[106] Eric F Spina, Alexander J Smits, and Stephen K Robinson. The physics of supersonic turbulent boundary layers. *Annual Review of Fluid Mechanics*, 26(1): 287–319, 1994.

[107] KR Sreenivasan, S Raghu, and D Kyle. Absolute instability in variable density round jets. *Experiments in Fluids*, 7(5):309–317, 1989.

[108] Gilbert Strang. On the construction and comparison of difference schemes. *SIAM Journal on Numerical Analysis*, 5(3):506–517, 1968.

[109] Pramod K Subbareddy and Graham V Candler. A fully discrete, kinetic energy consistent finite-volume scheme for compressible flows. *Journal of Computational Physics*, 228(5):1347–1364, 2009.

[110] Pramod K Subbareddy, Matthew D Bartkowicz, and Graham V Candler. Direct numerical simulation of high-speed transition due to an isolated roughness element. *Journal of Fluid Mechanics*, 748:848–878, 2014.

[111] Pramod K Subbareddy, Graham V Candler, and Pietro Ferrero. Scalar conservation in large eddy simulations of reacting flows. In *7th AIAA Theoretical Fluid Mechanics Conference*, number 3203, 2014.

[112] Pramod K Subbareddy, Anand Kartha, and Graham V Candler. Scalar conservation and boundedness in simulations of compressible flow. *Journal of Computational Physics*, 348:827–846, 2017.

[113] Xiao-Bo Sun and Xi-Yun Lu. A large eddy simulation approach of compressible turbulent flow without density weighting. *Physics of Fluids*, 18(11):118101, 2006.

[114] D Taulbee and J VanOsdol. Modeling turbulent compressible flows: the mass fluctuating velocity and squared density. *AIAA paper*, (524), 1991.

[115] Geraint Thomas, Richard Bambrey, and Caren Brown. Experimental observations of flame acceleration and transition to detonation following shock-flame interaction. *Combustion Theory and Modelling*, 5(4):573–594, 2001.

[116] Andrew Trettel and Johan Larsson. Mean velocity scaling for compressible wall turbulence with heat transfer. *Physics of Fluids*, 28(2):026102, 2016.

[117] VK Tritschler, BJ Olson, SK Lele, Stefan Hickel, XY Hu, and Nikolaus Andreas Adams. On the richtmyer–meshkov instability evolving from a deterministic multimode planar interface. *Journal of Fluid Mechanics*, 755:429–462, 2014.

[118] Edward R Van Driest. Turbulent boundary layer in compressible fluids. *Journal of the Aeronautical Sciences*, 18(3), 1951.

[119] Tobias Voelkl, DI Pullin, and Daniel C Chan. A physical-space version of the stretched-vortex subgrid-stress model for large-eddy simulation. *Physics of Fluids*, 12(7):1810–1825, 2000.

[120] Albertus Willem Vreman. *Direct and large-eddy simulation of the compressible turbulent mixing layer*. University of Twente, 1995.

[121] Albertus Willem Vreman, ND Sandham, and KH Luo. Compressible mixing layer growth rate and turbulence characteristics. *Journal of Fluid Mechanics*, 320:235–258, 1996.

[122] AW Vreman. An eddy-viscosity subgrid-scale model for turbulent shear flow: Algebraic theory and applications. *Physics of fluids*, 16(10):3670–3681, 2004.

[123] Sheila E Widnall, Donald B Bliss, and Chon-Yin Tsai. The instability of short waves on a vortex ring. *Journal of Fluid Mechanics*, 66(1):35–47, 1974.

[124] KA Winkler, Jay W Chalmers, Stephen W Hodson, Paul R Woodward, and Norman J Zabusky. A numerical laboratory. *Physics Today*, 40(10):28–37, 1987.

[125] Helen C Yee, Neil D Sandham, and M Jahed Djomehri. Low-dissipative high-order shock-capturing methods using characteristic-based filters. *Journal of computational physics*, 150(1):199–238, 1999.

[126] A. Yoshizawa, Y. Matsuo, and Y. Mizobuchi. A construction of the Reynolds-averaged turbulence transport equations in a variable-density flow, based on the concept of mass-weighted fluctuations. *Physics of Fluids*, 25(7):075105, 2013.

[127] Akira Yoshizawa. Statistical theory for compressible turbulent shear flows, with the application to subgrid modeling. *Physics of Fluids*, 29(7):2152–2164, 1986.

[128] David L Youngs. Three-dimensional numerical simulation of turbulent mixing by rayleigh–taylor instability. *Physics of Fluids A: Fluid Dynamics*, 3(5):1312–1320, 1991.

[129] Otto Zeman. Dilatation dissipation: The concept and application in modeling compressible mixing layers. *Physics of Fluids A*, 2(2):178–188, 1990.

[130] Otto Zeman. On the decay of compressible isotropic turbulence. *Physics of Fluids A*, 3(5):951–955, 1991.

[131] Xiangxiong Zhang and Chi-Wang Shu. On maximum-principle-satisfying high order schemes for scalar conservation laws. *Journal of Computational Physics*, 229(9):3091–3120, 2010.

[132] Ye Zhou. A scaling analysis of turbulent flows driven by rayleigh–taylor and richtmyer–meshkov instabilities. *Physics of Fluids*, 13(2):538–543, 2001.